Van der Waals heterostructures based on graphene and 2D ferroelectric CuInP$_2$S$_6$

PhD Thesis

Anubhab Dey

School of Physics and Astronomy

University of Nottingham

14th August 2023

Abstract

Two-dimensional van der Waals (vdW) ferroelectrics are of great technological interest for high-density electronics, such as non-volatile memories and field-effect transistors, due to their intrinsic ferroelectric polarisation. Their integration with graphene offers opportunities to create ferroelectric/graphene hybrid systems for novel applications, such as ferroelectric field effect transistors. Also in these systems, graphene can provide a sensitive probe of the ferroelectric polarisation, which is difficult to measure in thin ferroelectrics. Within the family of vdW ferroelectrics, $CuInP_2S_6$ (CIPS) has attracted widespread attention due to its relatively high Curie temperature (T_c = 315 K), out-of-plane ferroelectricity, ionic conductivity and large optical band gap at room temperature (E_g = 2.7 eV). This thesis focuses on the electrical and optical properties of CIPS in bulk and thin layers. In particular, it explores CIPS/graphene heterostructures and the unique phenomena that emerge from the charge transfer at the CIPS/graphene interface.

A series of planar and vertical devices based on CIPS/graphene heterostructures, including field effect transistors (FETs) and tunnel junctions (TJs), are investigated to study the charge transfer across the CIPS/graphene interface. Resistive switching and memristive effects are observed in the transport characteristics of the devices. These are attributed to ferroelectric polarisation and charge trapping in the CIPS layer. In the FET, electrostatic gating is used to control the charge transfer at the CIPS/graphene interface. The gate-induced time-dependent charge transfer is slow (τ > 100 s) and depends on the sweep rate and range of applied gate voltage. The hysteresis and memristive

effects are also sensitive to temperature and light illumination. A significant increase in hysteresis at temperatures $T > 200$ K suggests charge transfer from/to deep localised states in the CIPS layer. Also, light illumination leads to photo-ionisation of these states and a light activated slow redistribution of charges.

Finally, this thesis reports on the quantum Hall effect in graphene encapsulated by CIPS. Electrostatic gating of the graphene channel enables the Fermi energy to be tuned so that electrons in the localized states of CIPS are in equilibrium with the current-carrying, delocalized states of graphene. Due to the presence of strongly bound states in this hybrid system, a quantum Hall plateau is achieved at room temperature in relatively modest magnetic fields. This phenomenon offers the prospect for the controlled manipulation of the quantum Hall effect at room temperature.

Publications

- *Room temperature quantum Hall effect in a gated ferroelectric-graphene heterostructure*. **Anubhab Dey**, Nathan Cottam, Oleg Makarovskiy, Wenjing Yan, Vaidotas Mišeikis, Camilla Coletti, James Kerfoot, Vladimir Korolkov, Laurence Eaves, Jasper F. Linnartz, Arwin Kool, Steffen Wiedmann, Amalia Patanè (manuscript accepted in *Communication Physics* 2023)

- *Memristive effects due to charge transfer in graphene gated through ferroelectric $CuInP_2S_6$*. **Anubhab Dey**, Wenjing Yan, Nilanthy Balakrishnan, Shihong Xie, Zakhar R Kudrynskyi, Oleg Makarovskiy, Faguang Yan, Kaiyou Wang and Amalia Patanè, *2D Materials*. 9 (2022) 035003.

- *Ferroelectric semiconductor junctions based on graphene/In_2Se_3/graphene van der Waals heterostructures*. Shihong Xie, **Anubhab Dey**, Wenjing Yan, Zakhar R Kudrynskyi, Nilanthy Balakrishnan, Oleg Makarovsky, Zakhar D Kovalyuk, Eli G Castanon, Oleg Kolosov, Kaiyou Wang and Amalia Patanè, *2D Materials*. 8 (2021) 045020.

Conference presentations

- CMQM 2022, 20th-22nd June 2022, University of Bath, Bath, UK: Oral presentation. *Memristive effects in graphene induced by two dimensional ferroelectric $CuInP_2S_6$*.

- Graphene Week 2021 (virtual event), 20th-24th September 2021: Online poster presentation. *Electrically and optically controlled memristive effects in two-dimensional ferroelectric CuInP$_2$S$_6$.*

- EP2DS24-MSS20 2021 (virtual event) 31st October-5th November 2021: Online poster presentation. *Electrically and optically controlled memristive effects in two-dimensional ferroelectric CuInP$_2$S$_6$.*

Acknowledgements

Many people have contributed to the completion of this thesis and I owe each of them a great debt of gratitude. First and foremost, I would like to thank my supervisor Prof. Amalia Patanè, for her continuous support and encouragement throughout the course of my PhD. I am grateful for the time and effort she has invested in developing my research skills and guiding me throughout my research.

I am eternally grateful to my co-supervisor, Dr. Oleg Makarovskiy, for his expertise and assistance with the research and technical aspects of the experiments throughout my PhD. The 'Semiconductor Physics' module he taught has also benefitted me greatly.

I would also like to thank Dr. Wenjing Yan for her insights and support which were essential for the successful execution of the works completed herein.

My sincere thanks go to Prof. Laurence Eaves for his useful insights and fruitful discussions on various aspects of my work and life.
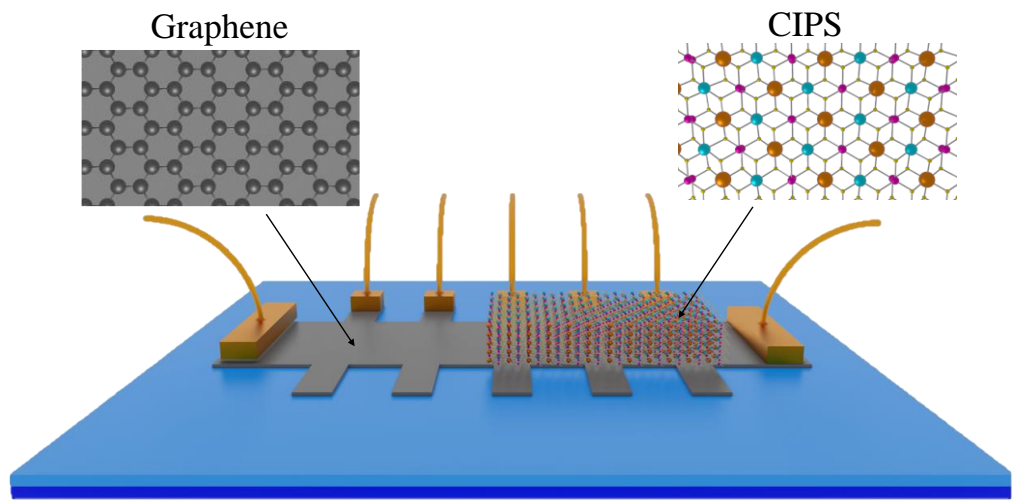
Physical Constants

Quantity	Symbol	Value	Unit
Boltzmann constant	k_B	1.38065×10^{-23}	JK^{-1}
Electron charge	e	1.60218×10^{-19}	C
Electron mass in vacuum	m_e	9.10938×10^{-31}	Kg
Permittivity in vacuum	ε_0	8.85419×10^{-12}	Fm^{-1}
Planck constant	h	6.62607×10^{-34}	Js
Reduced Planck constant	$\hbar$	1.05457×10^{-34}	Js
Speed of light in vacuum	c	2.99792×10^{8}	ms^{-1}

Graphene

CIPS

Schematics of CIPS/graphene Hall bar device

50μm
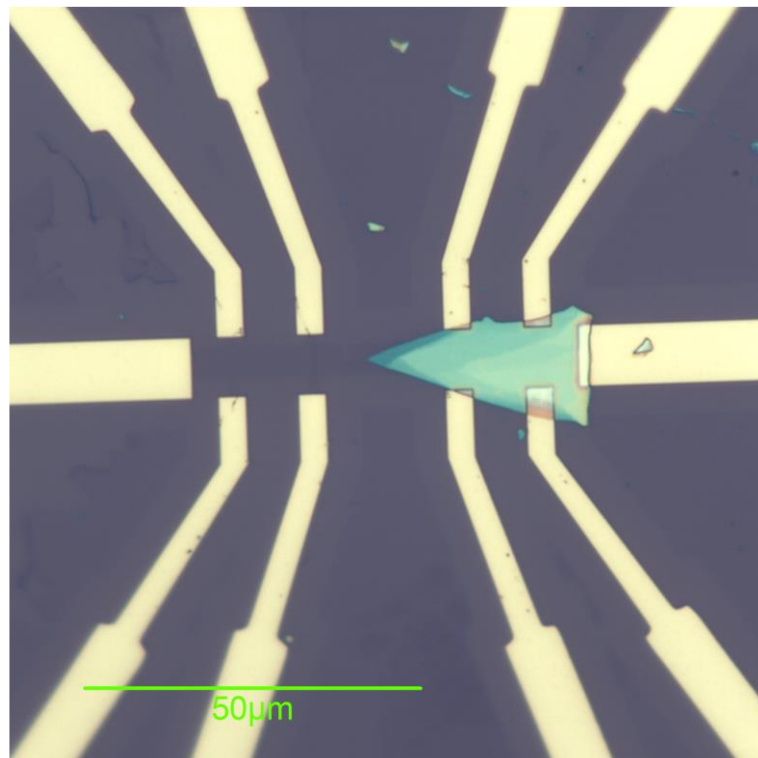
Optical image of a CIPS/graphene Hall bar device

List of Contents

Chapter 1

Introduction

Since the successful isolation of graphene in 2004 [1], scientific efforts have been focussed on a wide range of two-dimensional (2D) layered materials. Although graphene displays many extraordinary properties making it a unique platform for exploring low dimensional physics, it has many shortcomings like the lack of an electronic band gap [2]. 2D layered materials have the advantage over graphene of having extended bandgap tunability through composition, thickness and strain control. These exist in bulk form as stacks of strongly bonded layers with weak van der Waals (vdW) interlayer interactions, allowing exfoliation of bulk crystals into atomically thin layers. These atomically thin 2D vdW materials exhibit a wide range of unique electrical, optical, mechanical and thermal properties, which do not exist in their bulk counterparts [3]. Since the isolation of graphene, the library of 2D vdW materials has expanded considerably and now includes the wide-gap insulator hexagonal boron nitride (hBN), metal chalcogenides (*e.g.* InSe, GaSe), transition metal dichalcogenides (*e.g.* MoS_2, WSe_2) and metal oxides (*e.g.* TiO_2, MnO_2), to name a few. Among these, 2D vdW ferroelectric materials have drawn growing interest in recent years because of their intrinsic ferroelectric polarisation and potential applications in modern electronics. These materials have a non-centrosymmetric structure with a stable and switchable electric polarisation that can be reversed by an external electric field. Unlike conventional ferroelectrics consisting of complex perovskite oxide, such as $BaTiO_3$, $PbTiO_3$, and $BiFeO_3$, which suffer from imperfect charge screening, chemical defects and depolarising field in ultrathin films [4-6], the 2D vdW ferroelectric materials offer a feasible way of

exploring ferroelectricity at the atomic scale, facilitating further miniaturisation of electronic devices beyond the Moore's law. Because of their uniform atomic thickness, these materials offer the opportunity of high density data storage and non-volatile memory applications. Over the years, 2D ferroelectricity has been reported in $CuInP_2S_6$ [7], α-In_2Se_3 [8, 9], WTe_2 [10], SnTe [11], 1T-$MoTe_2$ [12] *etc*. However, although there have been many theoretical predictions, it is still difficult to measure weak in-plane or out-of-plane polarisation, particularly in thin layers. Also, various 2D vdW ferroelectric materials have been incorporated into hybrid ferroelectric memories [13-15], logic devices, such as ferroelectric field effect transistors (FeFETs) [16-18], ferroelectric tunnel junctions (FTJs) [19-21], and the switchable diode [22].

Within the family of 2D vdW ferroelectrics, $CuInP_2S_6$ (CIPS) is of particular interest due to its relatively high Curie temperature (T_c = 315 K), out-of-plane ferroelectricity [7, 23-26], ionic conductivity [27, 28] and large optical band gap at room temperature (E_g = 2.7 eV) [29]. In recent years, CIPS has been used in combination with other 2D materials to realize FeFETs [16, 30, 31], negative capacitance transistors [32, 33], photodetectors [34], FTJs [21, 35], memristors [36] and devices for energy applications [37, 38]. Despite the numerous reports on CIPS based device applications, there has been no extensive study of heterostructures consisting of CIPS and graphene. In particular, the electrostatic potential at the CIPS/graphene interface can be modified by switching the ferroelectric polarisation in CIPS. One of the interesting aspect is to understand the complex interplay between the charge transfer at the CIPS/graphene interface and the ferroelectric polarisation. This thesis presents a comprehensive study of the hysteretic and memristive effects in CIPS/graphene

heterostructure devices using electrical gating, high magnetic fields and light illumination. The studies presented in this thesis reveal different origins for the memristive behaviour in the transport characteristics. The thesis also describes how localised charge carriers in CIPS in proximity to graphene can contribute to the observation of a quantum Hall effect at room temperature. The understanding of these mechanisms is essential for the development of CIPS-based devices and their use in new device applications, such as non-volatile memories, quantum metrology, and low power electronics.

1.1 Thesis overview

The thesis is structured as follows:

Chapter 1 is an overview of the contents presented in the subsequent chapters.

Chapter 2 describes 2D vdW materials, describing well-known materials, such as graphene and hBN. This is followed by a brief description about 2D ferroelectrics, an emerging field of research within the family of 2D materials. Finally, this chapter discusses the crystal structure and ferroelectricity in CIPS, the primary 2D vdW ferroelectric material studied in this thesis. As a comparison, another widely studied ferroelectric material, α-In_2Se_3, is also described later in this chapter.

Chapter 3 details the methods and experimental techniques involved in the fabrication of hybrid field effect transistors (FETs) where a single layer of graphene is capped by a CIPS flake. A site-specific transfer technique of graphene microsheets to arbitrary substrates is also described in this chapter.

Chapter 4 describes the different characterisation techniques used in the project. This includes details of the optical techniques, surface analysis, electrical and magneto-transport measurements used throughout the project.

Chapter 5 reports on the optical studies of CIPS using photoluminescence and Raman spectroscopy. This includes the effect of temperature and layer thickness on the optical properties.

Chapter 6 discusses the memristive effects induced by a CIPS layer on the electrical properties of graphene. Here, we consider two types of devices based on the CIPS/graphene heterostructure. The first device is a planar hybrid FET where a single layer of graphene is capped by a CIPS flake. The second device is based on a vertical heterostructure where a thin CIPS layer is sandwiched between two few layer graphene electrodes. The charge transfer across the CIPS/graphene interface is studied by electrical transport measurements, which are sensitive to electrostatic gating, temperature and light illumination.

Chapter 7 investigates the quantum Hall effect (QHE) in CIPS/graphene heterostructures. It describes how the dynamic exchange of localised charge carriers at the CIPS/graphene interface enables the observation of the QHE at room temperature. This phenomenon is studied over a range of applied magnetic fields and temperatures.

Chapter 8 concludes the thesis, providing an overview of the key findings in this project followed by remarks on the future prospects for work beyond this thesis.

Chapter 2

Two-dimensional Van der Waals crystals

This chapter is a general introduction to van der Waals (vdW) crystals and heterostructures. In particular, it presents a description of two well-known two dimensional (2D) materials: graphene and hBN. Later sections in this chapter focus on a new category of 2D materials based on ferroelectrics. Of particular interest is $CuInP_2S_6$ (CIPS) whose properties are primarily featured in this thesis. Other 2D ferroelectric materials, such as α-In_2Se_3, are also discussed briefly for a comparison with CIPS.

2.1   2D vdW materials

The electronic properties of a crystal are affected by its dimensionality. The density of states (DoS) describes the number of states that are available to charge carriers per unit energy, $D(E)$, and is essential for determining the carrier concentrations and energy distribution of carriers within a material. With increasing number of confined dimensions, the density of states become increasingly more quantised. For example, for a bulk (3D) system the DoS is continuous; however, for a quantum dot (0D), the DOS consists of δ-like functions due to 0D discrete states (Figure 2.1). In particular, for a 2D semiconductor with a band gap energy, E_g, the electrons and holes are confined in a plane and the conduction and valence bands are described by 2D energy-wave vector dispersions. For a parabolic energy dispersion, the resulting $D(E)$ consists of step-like functions. These low-dimensional systems and the

phenomena resulting from the quantised energy states play a key role in the advancement of modern day electronic devices [39].
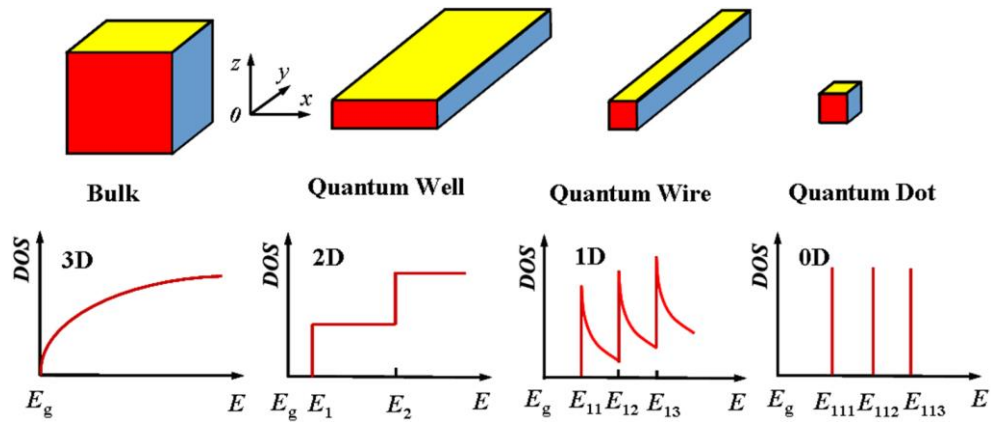
Figure 2.1. Diagram showing the density of states for systems with different dimensionality. Figure adapted from Ref. [40].

2.1.1 Graphene

As the first member of the family of 2D vdW materials, graphene has attracted enormous attention owing to its remarkable properties first reported experimentally in 2004 [41]. Single layer graphene (SLG) is an allotrope of carbon consisting of a single layer of covalently bonded carbon atoms arranged in a hexagonal (honeycomb) lattice with carbon-carbon spacing of 0.142 nm (Figure 2.2). Each carbon atom forms strong localised in plane σ-bonds with three nearest atoms by sp^2 hybridisation (a combination of s, p_x and p_y orbitals); the remaining non-hybridised electronic orbital (p_z) of each carbon atom forms a delocalised π-bond oriented out of plane of the graphene sheet. This orbital hybridises to form two half-filled bands of free moving electrons, π and π^*, which are responsible for graphene's notable electronic properties. These π bonds provide a weak van der Waals interaction between adjacent graphene

layers in bilayer and multilayer graphene sheets. Graphene sheets stack to form graphite with an interlayer spacing of 0.335 nm.
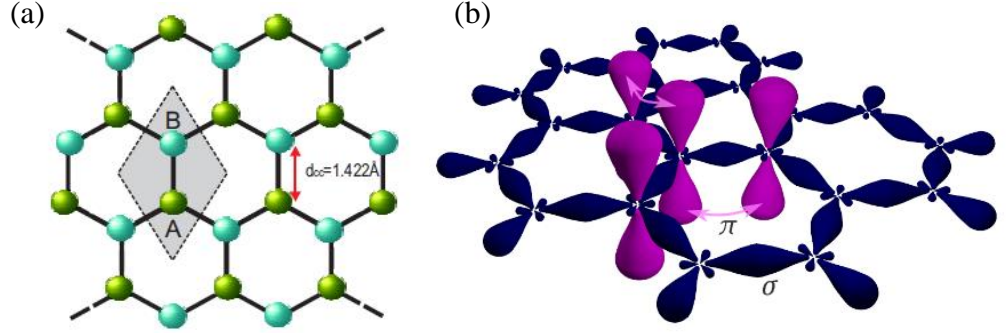
Figure 2.2. (a) Schematics showing the carbon honeycomb lattice with A and B interlinked sub-lattices and interatomic spacing $d_{cc} = 0.142$ nm. (b) Illustration showing in-plane σ-bonds and out-of-plane π-bonds in graphene. Figures adapted from Ref. [42].

Figure 2.3 shows the crystal structure and the first Brillouin zone of graphene. The unit vectors in real space for graphene are:

$$\vec{a_1} = \left(\frac{\sqrt{3}a}{2}, \frac{a}{2}\right), \vec{a_2} = \left(\frac{\sqrt{3}a}{2}, \frac{-a}{2}\right). \quad (2.1)$$

where $a = 0.142$ nm. The corresponding units vectors of the reciprocal lattice are:

$$\vec{b_1} = \left(\frac{2\pi}{\sqrt{3}a}, \frac{2\pi}{a}\right), \vec{b_2} = \left(\frac{2\pi}{\sqrt{3}a}, \frac{-2\pi}{a}\right). \quad (2.2)$$

The corners of the Brillouin zone (K and K') where the conduction and valence band meet, are called Dirac points and are given by:

$$\vec{K} = \left(\frac{2\pi}{3a}, \frac{2\pi}{3\sqrt{3}a}\right), \vec{K'} = \left(\frac{2\pi}{3a}, \frac{-2\pi}{3\sqrt{3}a}\right). \quad (2.3)$$
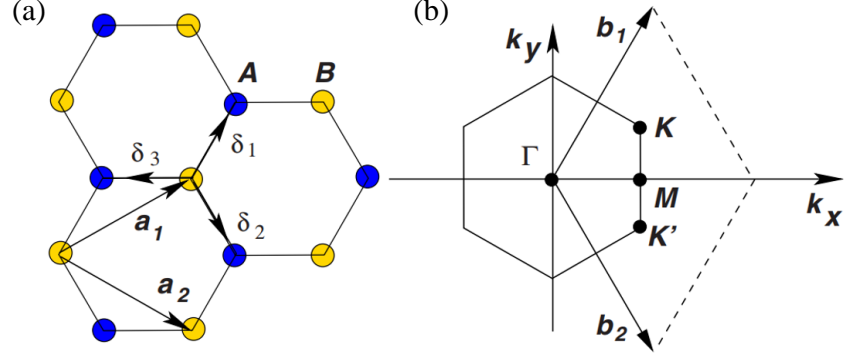
Figure 2.3. (a) Crystal structure of graphene with 2 unit cell atoms A (blue) and B (yellow). δ_1, δ_2, δ_3 are the vectors of the nearest neighbour sites. (b) Brillouin zone of graphene showing the points of symmetry Γ, K and M. Figure adapted from Ref. [43].

The conduction and valence bands meet at six vertices of the hexagonal Brillouin zone and form linearly dispersing Dirac cones. This peculiar band structure makes graphene a zero band-gap semiconductor and gives rise to interesting properties, such as ambipolar electric field effect [44], charge carrier tunability [45], and high carrier mobility [46].

The charge carriers in graphene mimic relativistic particles, namely massless Dirac fermions, as described by the Dirac equation [43]. The charge carriers follow a linear energy dispersion relation close to the Fermi level. This is given by:

$$E(p) = \pm v_F |p| . \tag{2.4}$$

Here, p is the electron momentum relative to the Dirac point and v_F is the Fermi velocity, $v_F \sim 10^6$ m/s. The energy states in the conduction band are considered positive while the energy states in the valence band are negative. Based on the 2D nature of graphene and its linear energy dispersion, the DOS of graphene can be expressed as:

$$D(E) = \frac{2E}{\pi v_F^2 \hbar^2} , \qquad (2.5)$$

and the carrier density in graphene at $T = 0$ K can be expressed as,

$$n(E_F) = \frac{E_F^2}{\pi v_F^2 \hbar^2} . \qquad (2.6)$$

For graphene on a SiO$_2$/Si substrate, the carrier density can be tuned by electrostatic gating as:

$$dn = \frac{\varepsilon_0 \varepsilon}{de} dV_G , \qquad (2.7)$$

where ε_0 and ε are the permittivity in free space and relative permittivity of the SiO$_2$ layer, respectively, d is the thickness of the oxide layer and V_G is the applied gate voltage on the Si substrate. Depending on V_G, the Fermi level moves up or down through the Dirac point according to

$$E_F = \pm \hbar v_F k_F = \pm \hbar v_F \sqrt{\pi n} . \qquad (2.8)$$

As the density of charge carriers changes with V_G, the resistance also changes with a maximum value at a particular gate voltage at which the Fermi level aligns with the Dirac point.
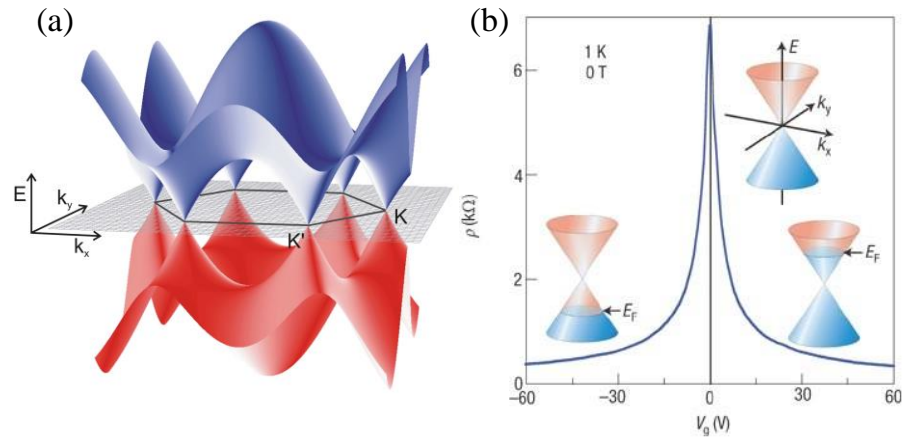
Figure 2.4. (a) Energy dispersion in the graphene honeycomb lattice. (b) Resistivity of graphene as a function of gate voltage and corresponding position of the Fermi energy. Figure adapted from Ref. [43].

The properties of graphene can vary tremendously depending on the growth technique and substrate used. Mechanical exfoliation from bulk graphite yields flakes with the highest mobility ($\mu > 200{,}000$ cm^2/Vs at room temperature [47]), as the produced SLG is not exposed to chemical processing or complex transfer processes. However, the graphene flake size is relatively small ($< 10 \times 10$ µm^2 [1]) and requires custom made electrical contacts to suit each flake, which is a time consuming process. Thermal decomposition of silicon carbide (SiC) produces wafer-scale SLG with homogeneous monolayer domains of size $> 50 \times 50$ µm^2 [48]. This type of graphene is typically heavily n-type ($n > 10^{12}$ cm^{-2}) with relatively low carrier mobility ($\mu \sim 10^3$ cm^2/Vs [49]) at room temperature. Commercially available CVD grown SLG is typically p-type and has a lower mobility ($\mu \sim 10^3$-10^4 cm^2/Vs [50, 51]) than exfoliated graphene. Graphene growth using molecular beam epitaxy (MBE) represents a relatively new route to large scale graphene production. Since the graphene can be grown directly on a dielectric material in an ultra-clean MBE environment, it does not require any transfer processes, thus producing pure graphene samples [52]. Other new methods include liquid phase exfoliation (LPE) involving exfoliation of graphite using sonication in solvents [53].

2.1.2 Hexagonal boron nitride

Hexagonal boron nitride (hBN) is another important material in numerous vdW heterostructures due to its inherent characteristics, which are complementary to both graphene and other 2D materials. hBN is a dielectric with mechanical robustness, low density of dangling bonds, and high thermal conductivity [54]. hBN is regularly used to encapsulate vdW materials, such as

graphene [55], InSe [56], MoS$_2$ [57], In$_2$Se$_3$ [58], as a means of either improving the electronic properties of the encapsulated material or protecting it from the environment.

2D-hBN nanosheets consists of a hexagonal layered structure with boron and nitrogen atoms bounded by strong covalent bonds within each layer (Figure 2.5a). These layers are held together by weak vdW forces. The unit cell parameters of hBN are $a = b = 2.502$ Å, $c = 6.617$ Å, $\alpha = \beta = 90^o$, $\gamma = 120^o$ with an interlayer spacing of ~ 3.3 Å [59]. The band structure of hBN exhibits an indirect to direct band gap crossover in the monolayer limit [60] (Figure 2.5b). The large band gap ~ 5.97 eV of bulk hBN [61] makes this material optically transparent to the wavelengths required to probe many vdW materials. hBN is also used as a gate dielectric in graphene based electronics as it lowers electron-hole charge fluctuations compared to SiO$_2$, leading to improved device performance.
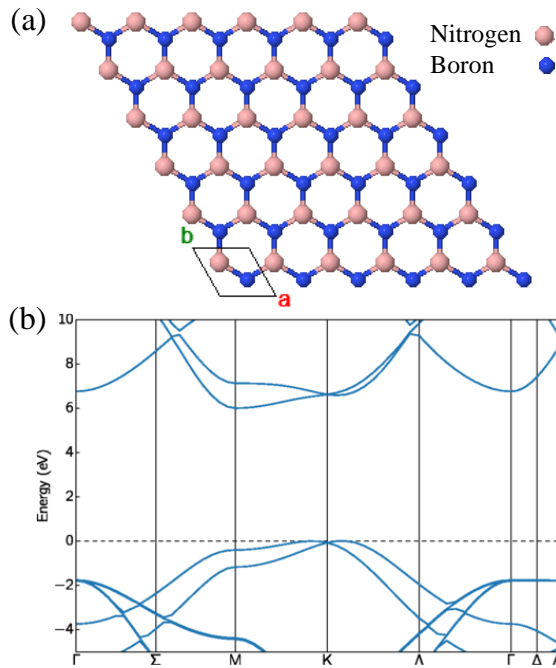
Figure 2.5. (a) Crystal structure of monolayer hBN. (b) Band structure of hBN showing the points of symmetry Γ, Σ, M, K and Λ in the Brillouin zone. Figure adapted from Ref. [62].

2.2   2D ferroelectrics

Ferroelectrics are materials with stable and switchable spontaneous polarisation (**P**) that can be reversed by an external electric field, **E**, yielding a hysteresis loop in the dependence of **P** on **E** (as shown in Figure 2.6) [63]. The electric field required to reverse the polarisation is called coercive field, E_c, and the temperature below which these materials demonstrate ferroelectricity is called the Curie temperature, T_c. Ferroelectricity has come a long way since its discovery in bulk crystals of Rochelle salt in 1920 [64]. Since then, together with theoretical development, plenty of studies have been conducted on traditional ferroelectric compounds, such as $PbTiO_3$, $BaTiO_3$, $BiFeO_3$, $PbZrO_3$ *etc*. However, these conventional ferroelectrics suffer from imperfect charge screening, chemical defects, and depolarising field in ultrathin layers [4, 65, 66].

In recent years many theoretical works have predicted 2D vdW materials with intrinsic ferroelectricity at the atomic scale, such as $CuInP_2S_6$ [7, 23], In_2Se_3 [8, 9], SnTe [11] and WTe_2 [10]. However, experimental observations of ferroelectricity in 2D materials are rare since it is still difficult to measure weak in-plane or out-of-plane polarisation in thin layers. These 2D ferroelectric materials have been used in different devices, such as ferroelectric field effect transistors (Fe-FETs), ferroelectric tunnel junctions (FTJs), and ferroelectric switchable diodes [67]. The outstanding behaviours of these 2D ferroelectric materials have opened up possibility of combining them with other semiconductors for computing-in-memory architectures with efficient data reading/writing.

Some of the experimentally confirmed 2D vdW ferroelectric materials are summarized below in Table 2.1.

Material	E_c (V/nm)	T_c (K)	Bandgap (eV)	References
$CuInP_2S_6$	5×10^{-3}	315 (5L)	2.7	[7, 29]
$CuCrP_2S_6$	-	32 (bulk)	1.4 (1L)	[68]
SnTe	-	270 (1L), 98 (bulk)	1.6 (1L), 0.3 (bulk)	[11]
SnSe	14×10^{-3}	>380 (1L)	2.1 (1L), 0.9 (bulk)	[69]
SnS	1.07×10^{-3}	>300 (1L)	1.6 (1L), 1.2 (bulk)	[69]
GeTe	0.2	570 (1L)	0.6 (bulk)	[70]
α-In_2Se_3	0.02	700 (4L)	2.8 (1L), 1.4 (bulk)	[8, 71]
$MoTe_2$	-	330 (1L)	-	[12]
WTe_2	0.05	350 (2-3L)	-	[10, 72]

Table 2.1. Different 2D vdW ferroelectrics. E_c, T_c and L represent the coercive electric field, the Curie temperature and the number of layers, respectively. The table is reproduced from Ref.[73].

Here, this section introduces the ferroelectric copper indium thiophosphate ($CuInP_2S_6$ or CIPS). This belongs to the transition metal thiophosphate (TMTP) family. CIPS is the primary vdW material studied in this project. As a comparison, another vdW ferroelectric material belonging to the III-VI group, α-In_2Se_3, is described later.
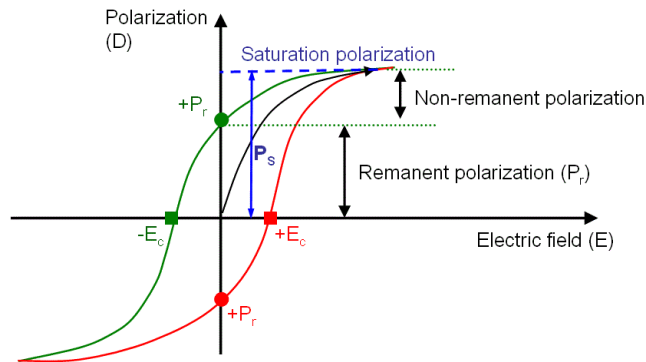
Figure 2.6. Typical polarisation versus electric field curve for a ferroelectric material. Figure adapted from Ref. [63].

13

2.2.1 CuInP$_2$S$_6$

CIPS has attracted widespread attention in recent years due to its vdW layered structure and ferroelectricity at room temperature. This section focuses on two aspects: the crystal structure and the out-of-plane ferroelectricity of CIPS.

CIPS belongs to the family of transition metal thiophosphates, a broad class of vdW crystals where metal cations are embedded in the lattice framework of thiophosphate ($P_2S_6^{4-}$) anions. It is a layered vdW material with monoclinic symmetry (space group *Cc* at *T* = 296 K) consisting of ABC close packed stacking of sulphur atoms [24]. In the sulphur framework, the metal cations (Cu^{1+} and In^{3+}) and P-P pairs fill the octahedral voids (Figure 2.7). Amongst them, the Cu, In and P-P pairs form a triangular pattern in the same layer. The bulk crystals of CIPS consists of vertically stacked and weakly interacting vdW layers. Since the positions of Cu and P-P pairs are exchanged from one layer to another, a complete unit cell is composed of two adjacent layers.
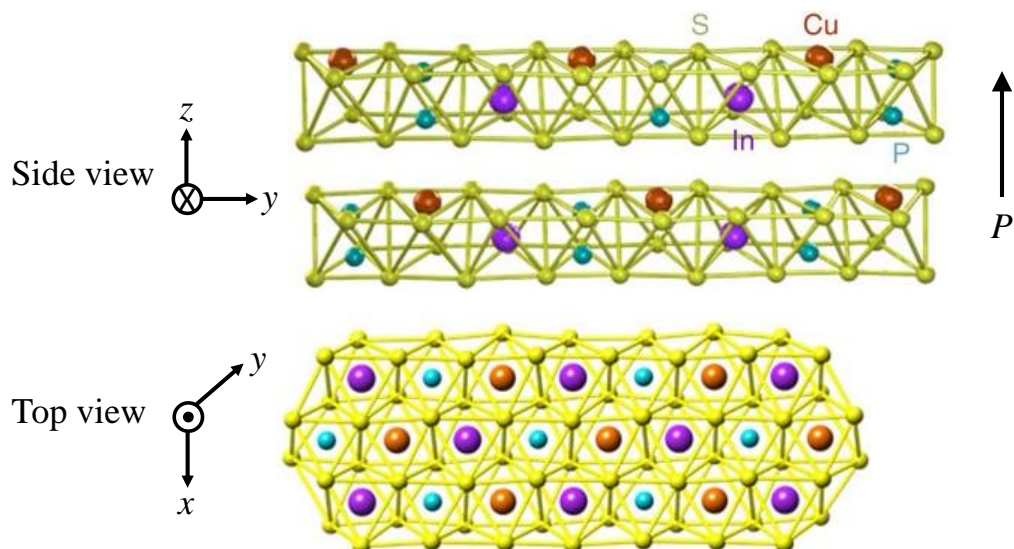
Figure 2.7. Side and top view of CuInP$_2$S$_6$ crystal structure with vdW gap between the layers. The polarisation direction is indicated by the arrow. Figure adapted from Ref. [74].

The out-of-plane ferroelectricity and ionic conductivity of CIPS originates from the spatial instability of the Cu^{1+} cations. The Cu^{1+} cation can occupy three crystallographic sites in the sulphur octahedral cage: Cu1, Cu2 and Cu3 [75] (Figure 2.8). Cu1 is the quasi-trigonal position shifted from the centre of the octahedra, Cu2 is the octahedral centre, and Cu3 is situated in the vdW gap. In addition to these sites, a twofold axis doubles each position. The $Cu1^u$ position is displaced upwards from the centre of the S_6 octahedron and the $Cu1^d$ position is displaced downwards from it.
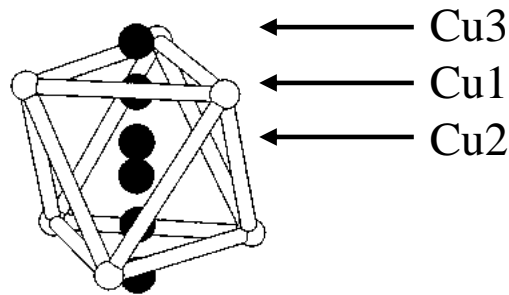
Figure 2.8. Sulphur octahedral cage showing different copper sites: the off-centre Cu1, the almost centre Cu2, and the Cu3 in the interlayer space.

At low temperature ($T = 153$ K), the $Cu1^u$ position is fully filled [75] (Figure 2.9). As the temperature increases, the occupancy of the $Cu1^u$ position decreases and the $Cu1^d$ position is filled in the meantime. Above $T_c = 315$ K, the $Cu1^u$ and $Cu1^d$ positions become equivalent (Cu1) and the crystal structure becomes centrosymmetric (space group *C2/c*) with the appearance of a twofold axis through the octahedral centre. At $T = 353$ K, the Cu1 occupancy decreases and the Cu2 and Cu3 sites begin to fill, as more energy becomes available for hopping motion. At higher temperatures, Cu1-Cu3 hopping is observed, resulting in the copper ions being able to penetrate into the vdW gaps. Thus,

above T_c, the motion of the copper ion increases not only inside the layers but also in the interlayer gaps.
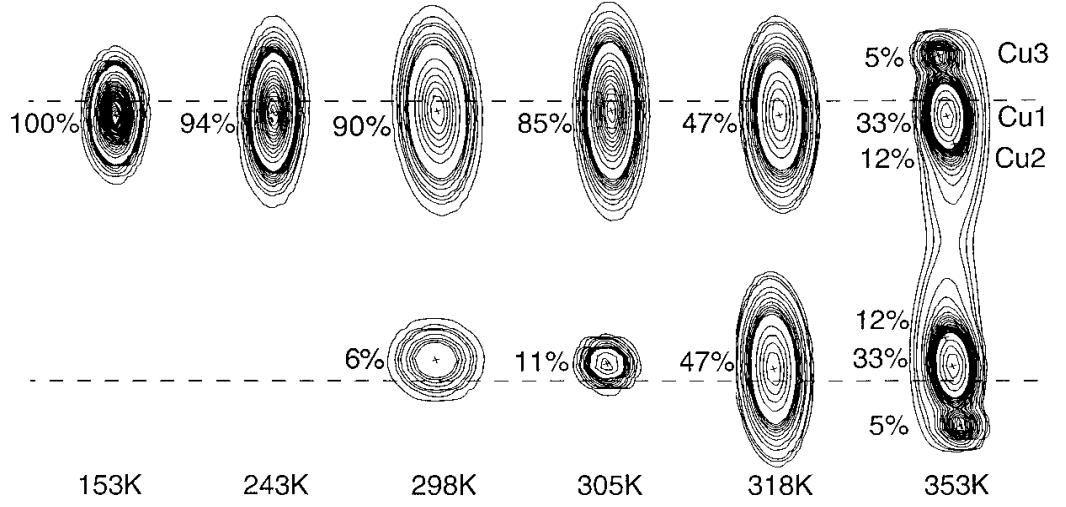
Figure 2.9. Thermal evolution of the different copper site occupancies and the corresponding probability density contours in $CuInP_2S_6$ measured using elastic X-ray data. The crosses mark the refined positions, and the dashed lines indicate the upper and lower sulphur planes of a single layer. Figure adapted from Ref. [75].

The spontaneous ferroelectric polarisation (**P**) originates from the off-centre ordering of the Cu^{1+} cations. To balance this structural distortion, In^{3+} cation in the adjacent S_6 octahedron displaces in the opposite direction to Cu^{1+}, resulting in a collinear ferroelectric lattice. The polarisation of CIPS has been found to be in the range of $2.55 - 4$ $\mu C/cm^2$ using various methods, such as the Born effective charge method and the Berry-phase approach [7, 75-77]. The discrepancy in the accurate determination is due to the Cu3 site being partially filled, producing a large dipole moment and considerable ionic conduction. The coercive field of CIPS was reported to be $E_c \sim 5 \times 10^6$ V/m in bulk CIPS by polarisation switching studies [76] and $\sim 14 \times 10^7$ V/m in thin layers by capacitance-voltage measurements [35].

16

The base-centred monoclinic lattice parameters of both the ferroelectric ($T < 315$ K) and paraelectric phase ($T > 315$ K) of CIPS are: $a = 6.09559$ Å, $b = 10.56450$ Å, $c = 13.6230$ Å, $\alpha = \gamma = 90°$, $\beta = 107.1011°$ [75]. The Brillouin zone of CIPS is shown in Figure 2.10.
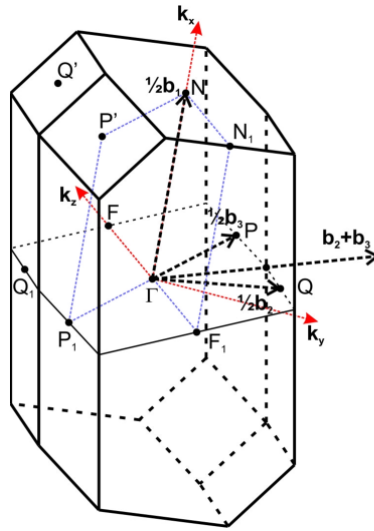
Figure 2.10. Brillouin zone for both paraelectric and ferroelectric phases of the monoclinic $CuInP_2S_6$ crystal. Figure adapted from Ref. [78].

The electronic energy structure of CIPS calculated using density functional theory shows that ferroelectric CIPS is a direct band gap material ($\Gamma \rightarrow \Gamma$ transition) whereas the paraelectric CIPS exhibits an indirect band gap [78, 79], as shown in Figure 2.11. In para-electric CIPS the valence band maximum (VBM) is located at the L point, while the conduction band minimum (CBM) is at the Γ point. The calculated partial density of states demonstrate that the top of the valence band of CIPS crystal is created by electrons belonging to Cu and S atoms, while the bottom of the conduction band is formed by mixed orbitals of In and P_2S_6 complexes.
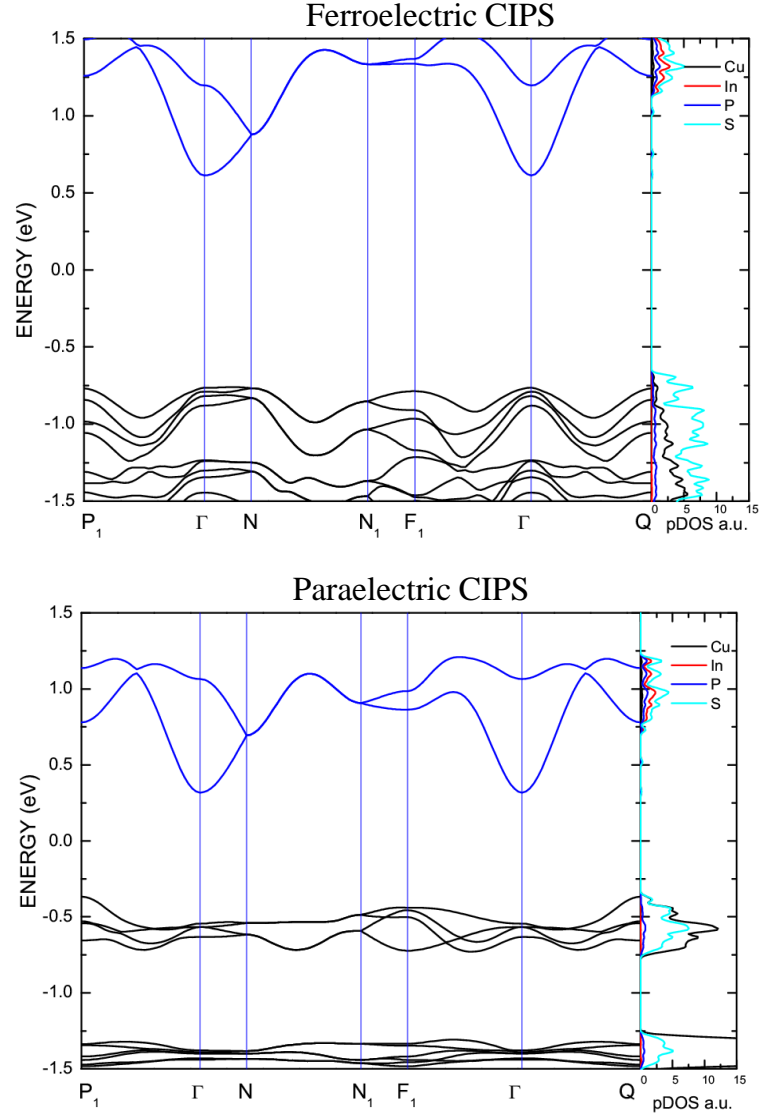
Figure 2.11. *Ab initio* band structure and density of states of $CuInP_2S_6$. Figure adapted from Ref. [78].

2.2.2 In$_2$Se$_3$

In$_2$Se$_3$ is one of the most important III-VI semiconductors that has been extensively studied in recent years. In$_2$Se$_3$ can exist in five different polytypes (α, β, γ, δ, κ [80]) due to different stacking order of the layers and polymorphs. The α phase is considered to be the most stable structure at room temperature. A single layer of α-In$_2$Se$_3$ consists of alternating Se and In atomic layers connected via covalent bonds to form a Se-In-Se-In-Se quintuple layer (QL).

18

These QLs are bound to each other through weak vdW forces [71]. By shifting the central Se atom layer, using an energy efficient kinetic pathway, out-of-plane and in-plane polarisation can be reversed simultaneously in a coupled motion (Figure 2.12). The lateral shift of the Se atoms alters the interlayer spacing with neighbouring In atoms in both out-of-plane and in-plane directions [71].
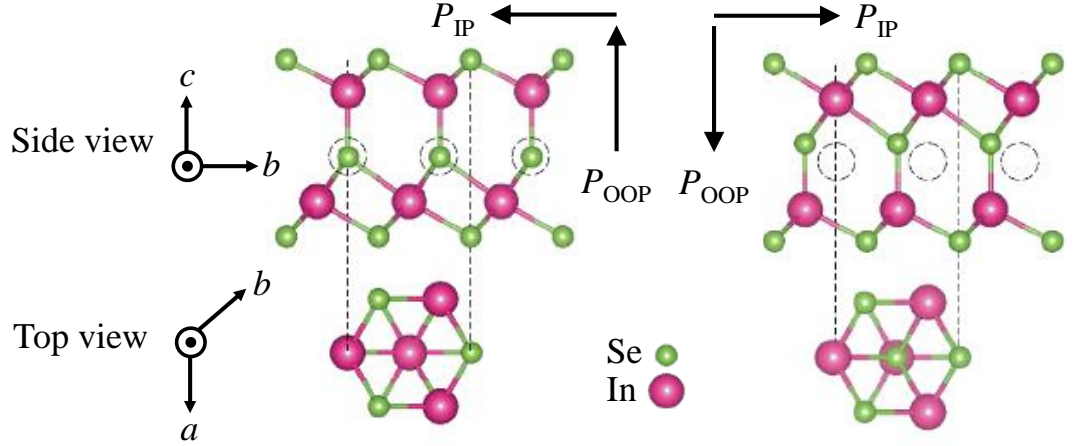
Figure 2.12. Side and top views of two oppositely polarized α-In$_2$Se$_3$ quintuple layers. Figure is adapted from Ref [81].

The unit cell parameters of bulk α-In$_2$Se$_3$ are: $a = b = 3.98$ Å, $c = 18.9$ Å, $\alpha = \beta = 90°$, $\gamma = 120°$. Due to robust quantum confinement, the band gap varies from 1.45 eV to 2.8 eV with the thickness decreasing from 95 nm to 3 nm [82]. First principle calculations show that the band gap of bulk α-In$_2$Se$_3$ is indirect. Figure 2.13 shows the electronic band structure and Brillouin zone for one QL of α-In$_2$Se$_3$. The valence-band maximum (VBM) occurs along the Γ-L direction (about one third of the Γ-L distance from Γ), while the conduction-band minimum (CBM) is located at Γ, with an indirect band gap of 1.34 eV [83]. The low coercive field ($\sim 10^7$ V/m) and room temperature ($T_c > 500$ K) in-plane and out-of-plane ferroelectricity makes α-In$_2$Se$_3$ a promising material for ferroelectric field effect transistors [84] and ferroelectric tunnel junctions [85].
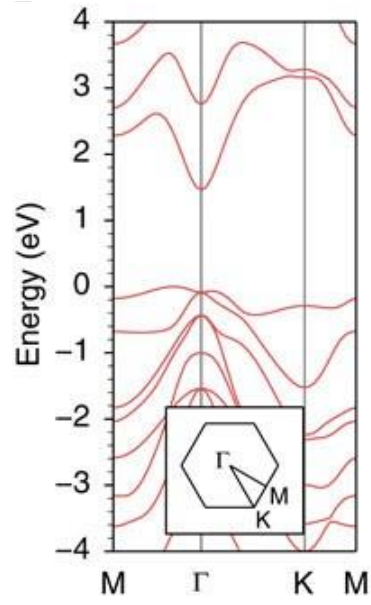
Figure 2.13. Electronic band structure of one quintuple layer of ferroelectric α-In$_2$Se$_3$. Inset shows the first Brillouin zone. Figure adapted from Ref. [71].

Chapter 3

Sample fabrication techniques

This chapter describes the techniques used to fabricate the different types of CIPS/graphene heterostructures used in this project. The graphene described here is in the form of individual graphene microsheets suspended in a membrane, which can be transferred to a desired location. Also, flakes of CIPS are obtained by mechanical exfoliation and transferred on top of graphene or on specific substrates for electrical and optical studies. High quality pristine CVD graphene FETs were provided by collaborators, Dr. Camilla Coletti and Dr. Vaidotas Mišeikis, in the NEST laboratories at the Istituto Italiano di Tecnologia, Italy.

3.1   Mechanical exfoliation

Exfoliation techniques discussed here are largely used for mechanical exfoliation and isolation of $CuInP_2S_6$ (CIPS) flakes. Mechanical exfoliation was originally developed by Andre Geim and Konstantin Novoselov for the isolation of monolayer graphene in 2004 and has been successfully applied to other two-dimensional vdW materials [1]. Despite low yield and relatively small size of the single-layer flakes produced by this technique, it is widely used due to its accessibility and excellent material quality of the produced sample. The techniques discussed here routinely produced uniform thin CIPS flakes (down to $t \sim 12$ nm) with a minimum area of ~ 100 μm^2. This area is needed for device fabrication, photoluminescence and Raman experiments.

For exfoliation, we first prepare a polydimethylsiloxane (PDMS) stamp on clean glass slides. These glass slides are cleaned by standard cleaning

techniques using acetone and isopropyl alcohol (IPA). We use pre-packaged DGL/17-X4 polymer films available from Gel-pack. This is a silicone-based film with a thickness of ~ 0.43 mm and has sufficient retention strength for exfoliation of thin layers. These are then cut into 10 mm squares and then, using a tweezer, placed on the glass slide. Putting one corner down first and slightly bending the rest of the stamp to let it slowly roll onto the glass slide avoids the formation of bubbles. The protective cover sheet is then removed for the transfer of flakes.

The CIPS crystal, as shown in Figure 3.1a, was purchased from HQ graphene. Flakes of various thickness were exfoliated from the bulk crystal under ambient conditions. This method relies on the difference between in-plane covalent and out-of-plane weaker van der Waals bonds, which facilitate the cleavage at the interface between two adjacent planes. We use a low residue, commercially available adhesive tape from Nitto. The tape is cut into small pieces larger than the size of the PDMS stamp. The bulk crystal is then placed between two pieces of tape and pressure is applied to ensure good contact between the tape and surface of the crystal. The two pieces are then pulled apart, resulting into flakes scattered on the tape (Figure 3.1b). This process is repeated several times. More peels ensure larger surface coverage and overall thinner flakes of small sizes. The resultant flakes have a broad range of thickness ranging from $t \sim 12$ nm to several hundred microns. The lateral dimension of the flake varies extensively depending on the thickness, with the thinner flakes being smaller in size. The prepared tape is then put on top of the PDMS stamp and pressure is applied gently with a cotton bud to ensure good contact between the tape and PDMS (Figure 3.1c). Too much pressure can lead to formation of

22

wrinkles and cracks in the material. After transferring the flakes onto the PDMS stamp, the tape is peeled off. A faster peel usually results in more material being transferred. Figure 3.1d shows the CIPS flakes transferred from the tape onto the PDMS stamp. These flakes are then analysed under the microscope. Figure 3.1e shows a typical optical image of exfoliated CIPS flakes of varying thickness scattered on PDMS. Individual flakes can be selected for different experiments and transferred to 300 nm thick SiO_2/Si substrates.
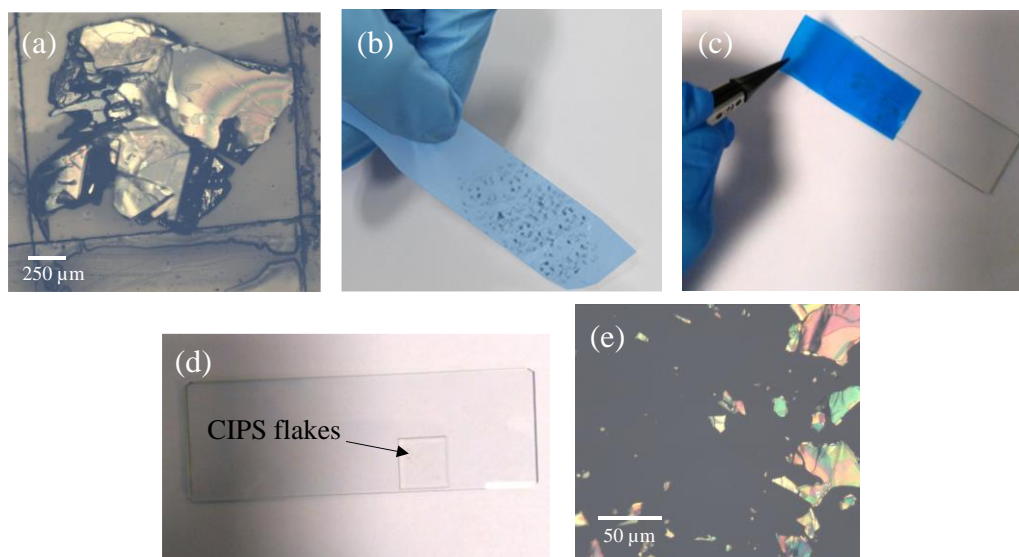
Figure 3.1. (a) Optical image of bulk CIPS crystal. (b) CIPS flakes scattered on a Nitto tape. (c) The tape with flakes is pressed on top of a PDMS stamp. (d) PDMS stamp showing the location of CIPS flakes. (d) Optical image of the PDMS stamp under a microscope using a 20x objective.

3.2 Deterministic dry-transfer technique

A deterministic all-dry transfer set-up based on a technique similar to that described by Castellanos-Gomez *et al*. [86] was used to control the position and alignment of the exfoliated vdW nanosheets. Typically, mechanically exfoliated flakes on PDMS film adhered to a glass microscope slide are examined under an optical microscope to locate the desired nanoflake. Once

suitable flakes are identified, they can then be stamped onto a desired substrate. The glass slide with the desirable flake is clamped to the stamping arm of the stamping system. Figure 3.2 shows a schematic of the system used to transfer exfoliated flakes. The system includes a stamping arm, which is manually operated by a micrometer stage capable of *xyz* translation with dual-goniometers for precise angular rotation. There is a motorised stage capable of making 360° rotation and *xy* translation controlled by a computer. A microscope display up to 50x objective is aligned perpendicular to the stage. This ensures the flake and the substrate are suitably aligned up until the point of contact by varying the focal point of the microscope. It is usual for some drift to occur of the order of a few µm in the *xy* plane as the stamping arm is lowered. The motorised stage and the stamping arm can be adjusted for misalignments. By incrementally trimming the edges of the PDMS stamp with a scalpel and checking the distance of the desired flake from the edge using the microscope, it is possible to create polymer squares of ~ 1 mm^2 around the desired flake. This allows for the transfer of flakes to a substrate without the risks of damaging flakes after consecutive transfers. The other benefit is that the PDMS stamp may trap debris or air pockets when adhering to glass slide. The target substrate is attached to the copper plate using a double-sided adhesive tape. The interfaces of the material to be deposited and the target substrate are brought onto contact by lowering the stamping arm. The point of contact can be detected by the change in the optical contrast from the PDMS stamp touching the substrate. The viscoelastic property of PDMS allows us to vary the adhesion between the PDMS stamp and the substrate using the micromanipulator in the *z* direction. The adhesive strength varies with the

peeling rate, causing a kinetic switching between adhesion and release of flakes as they are deposited on the substrate [87].
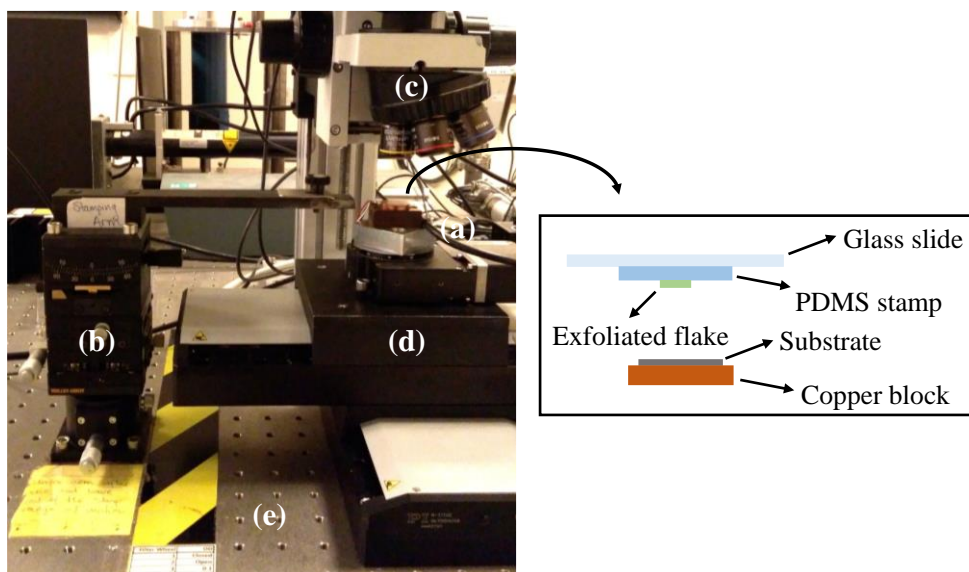
Figure 3.2. All-dry deterministic transfer set-up of exfoliated flakes onto arbitrary substrates. The different components of the setup are: (a) Sample section. (b) Transfer arm holding the glass slide. (c) Microscope with 5x, 10x, 20x and 50x magnification. (d) Substrate controller stage. (e) Optical bench.

3.3 Needle assisted transfer of graphene microsheets

A site-specific transfer technique of individual graphene microsheets to arbitrary substrates was developed according to the method described by Bie *et al*.[88]. In this method, several graphene microsheets with a lateral dimension of 10 μm × 40 μm are fabricated by electron beam lithography (EBL) using commercially available CVD graphene on 300 nm thick SiO_2 on Si. Following the EBL processing, the resultant PMMA-graphene stack on SiO_2/Si is etched in a solution consisting of Buffered Oxide Etch (BOE) and Hydrofluoric acid (HF) at a ratio of 5:2. After a few minutes, PMMA/graphene film floats on the top of the etching solution surface, which is sieved using a plastic boat and transferred into DI water. The film is washed several times with DI water, following which

a copper grid is used to remove it carefully. Figure 3.3 shows the process of making a PMMA/graphene membrane suspended on a copper grid. After drying in an inert atmosphere overnight, the PMMA/graphene film is used for the transfer of individual graphene microsheets onto a target substrate deterministically.
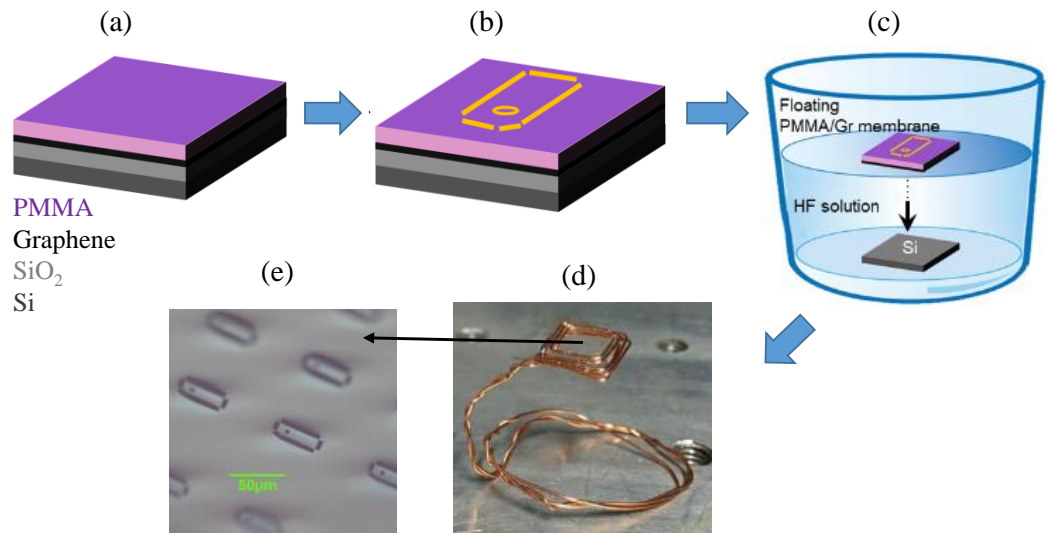
Figure 3.3. Schematics of preparation of graphene microsheets. (a) PMMA spin coated on graphene/SiO_2/Si. (b) Patterning PMMA/graphene using EBL and plasma etching. (c) Etching SiO_2 in HF solution. (d) Scooping the PMMA/ graphene using a copper grid. (e) Optical image showing the PMMA/graphene microsheets spread across the membrane.

The copper grid containing the PMMA/graphene microsheets is attached to the copper block in the transfer set-up. A glass fiber with a tip diameter of ~500 nm is attached with the transfer arm of the set-up. Using three-axis (x,y,z) micromanipulators, one corner of a microsheet is touched gently with the needle tip. The microsheet is torn apart from the base membrane and adhered to the needle for transfer onto a target substrate. After a successful transfer, the substrate containing PMMA/graphene microsheet is heated on a hot plate at $T =$ 180 ºC for 30 minutes and dissolved in acetone for 30 mins to remove the PMMA. Figure 3.4 shows a successful transfer of graphene microsheet on top

of a CIPS flake. If the graphene microsheet is in an unwanted location, the above mentioned process can be repeated after placing the sample in hot acetone ($T = 60\ °C$) for 30 minutes which will remove the graphene.
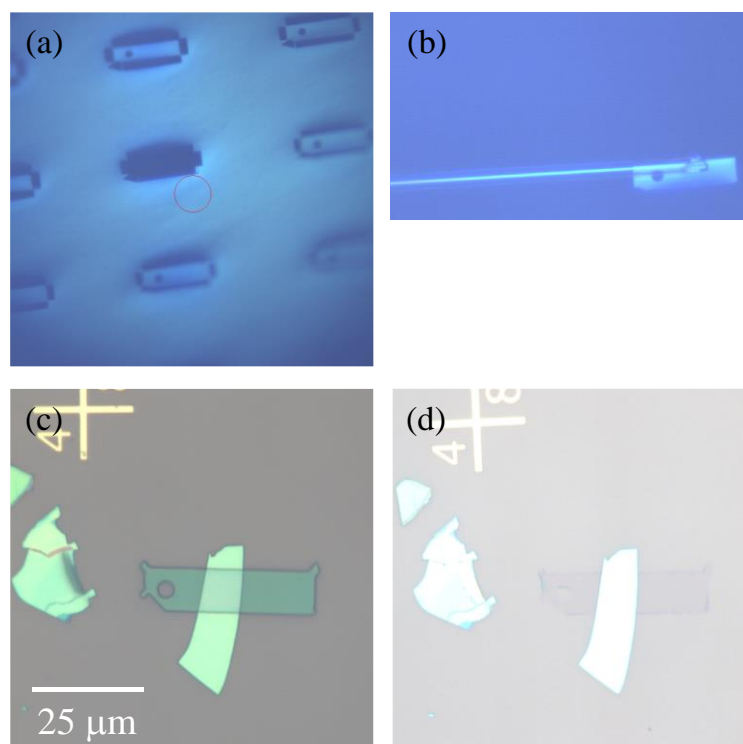
Figure 3.4. (a) Optical image of PMMA/graphene membrane with a graphene microsheet detached using a glass needle. (b) PMMA/Graphene microsheet attached to the glass needle. (c) PMMA/graphene transferred on top of a CIPS flake. (d) Graphene microsheet on top of CIPS after washing away PMMA.

3.4 Patterning of single layer graphene

Figure 3.5 shows a device based on CIPS/graphene heterostructure. Here, a graphene stripe is first transferred to 300 nm thick SiO_2 on Si substrate using the needle technique. The CIPS/graphene heterostructure was processed by electron beam lithography (EBL) using nanobeam nB5EBL tool in the Nanoscale and Microscale Research Centre (nmRC) at the University of Nottingham.

Prior to EBL processing, the graphene microsheet is spin-coated with polymethyl methacrylate (PMMA) (8% in anisole) at 4000 rpm for 30s and baked on a preheated hot plate at $T = 180\ ^\circ$C for 10 mins and left to cool down to room temperature followed by a further spin-coat of PMMA (2% in anisole) under the same conditions. The resulting stack of thickness ~ 500 nm is used as a high-resolution positive electron-beam resist. The sample is then patterned by EBL. Selective removal of the exposed regions of the resist is done by immersing it in a solution of isopropyl alcohol (IPA) and deionised water (DI) water at a ratio of 7:3, leaving the unexposed PMMA as a mask to pattern graphene by plasma etching (Figure 3.5b). We use reactive ion etching (RIE) using Corial 200IL RIE/ICP plasma etcher that mixes bombardment by ions and chemical etching with alternating electric fields with a range of gas chemistries.
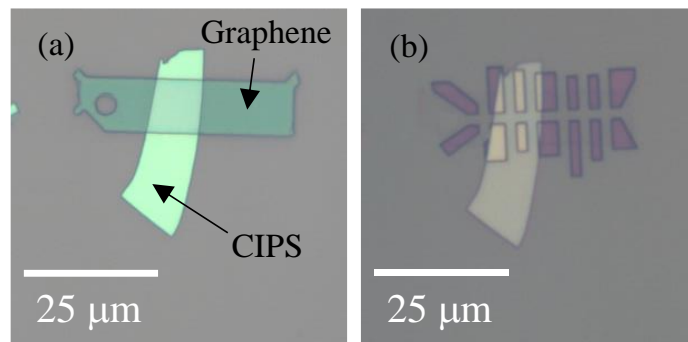
Figure 3.5. (a) Optical image of a graphene microsheet transferred on top of a CIPS flake (t ~ 50 nm). (b) EBL patterned graphene microsheet before etching.

To deposit titanium/gold (Ti/Au) at the graphene edges to form contact pads, a dual layer of PMMA (A8 and A2) is spin coated followed by another EBL exposure and development procedure, as described above. The optical image of the device after EBL exposure is shown in Figure 3.6a. The metal deposition is carried out by loading the masked graphene/substrate into an Edwards Auto 305 thermal evaporator. At a typical deposition rate of 0.30 - 0.45

nm/s, a Ti/Au (10/100 nm) bilayer is deposited and left for several minutes to cool down to room temperature. To remove the excess metal and unexposed PMMA, the substrates are immersed in acetone at $T = 60\ °C$ for ~ 1-3 hours and rinsed with IPA and gently dried by a pressurised nitrogen gas stream. Figure 3.6b shows the CIPS/graphene heterostructure device with gold contacts. Finally, graphene is cleaned by thermal annealing in argon: hydrogen (Ar:H_2 = 95:5) atmosphere at $T = 300\ °C$ for 3 hours.
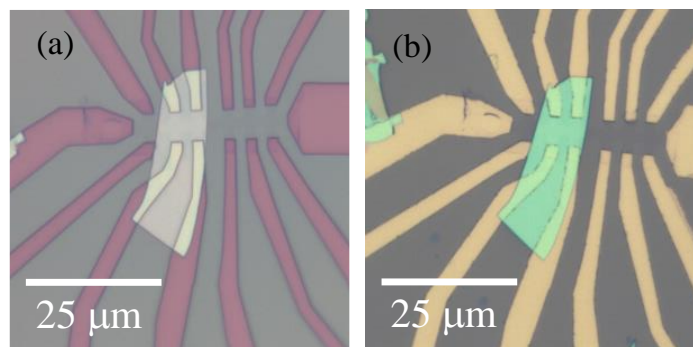
Figure 3.6. (a) EBL pattern for metal contacts on graphene. (b) Finished CIPS/graphene multi-terminal FET after Ti/Au deposition.

3.5   Mounting and bonding devices

Non-magnetic headers produced in-house are used for mounting samples. These have either 12 or 8 pins and can have a copper plate (as shown in Figure 3.7a) to help improve electrical contact with the back gate of the Si/SiO$_2$ substrate. The device is mounted onto the header and held in place using silver conductive paste (DuPont conductor paste 4929N). The silver paste, once dry, also acts as a conductive bridge between the back gate and one of the pins on the header (Figure 3.7b). The contact pads on the device are bonded to a pin on the header using a 50 µm diameter gold wire using silver paste. After bonding,

the sample is left to dry overnight in a controlled atmosphere, namely in a nitrogen chamber or in a pumped vacuum cryostat.
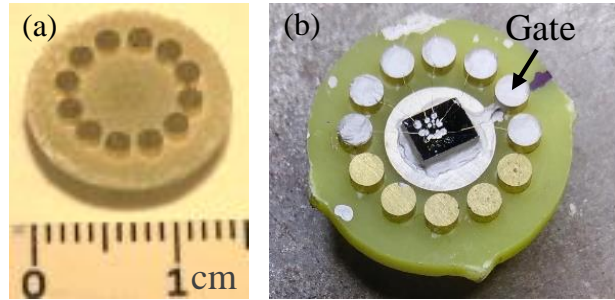
Figure 3.7. (a) Optical image of a 12-pin non-magnetic header. (b) CIPS/graphene heterostructure device mounted on a copper plated header using silver paste.

3.6 Summary

Using mechanical exfoliation and dry transfer, it is possible to create vdW heterostructures and devices from individually exfoliated flakes of CIPS on 300 nm thick SiO_2/Si substrates. The processing of graphene samples using EBL avoids the exposure to harsh chemicals used in traditional lithography techniques, which can cause unwanted doping and damage the layers. The quality of the samples can be assessed through the observation of physical phenomena dependent on the sample and interface quality which will be discussed in the following chapters.

Chapter 4

Experimental techniques

This chapter describes the various techniques employed in the characterisation of samples. These techniques are classified here into three broad categories: optical studies (photoluminescence and Raman), surface characterisation (atomic force microscopy, piezoresponse force microscopy, Kelvin probe force microscopy) and electrical measurements.

4.1   Optical studies

2D layered materials have extraordinary optoelectronic properties owing to their distinct electronic band structures and quantum confinement of charge carriers. Several spectroscopy techniques, particularly micro-photoluminescence (μPL) and micro-Raman (μRaman) are extensively used in this project to study the fundamental light-matter interaction in 2D materials.

4.1.1 Photoluminescence

Photoluminescence (PL) is the radiative emission of photons by a material after light excitation. In a PL experiment, the semiconductor material is excited using a laser with energy (E_{ex}) higher than the band gap energy (E_g) of the material, *i.e.* $E_{ex} = h\nu > E_g$, leading to photon absorption and generation of electron-hole pairs. An electron excited onto a state in the conduction band (CB) relaxes and eventually recombines with a hole in the valence band (VB) by emitting a photon of energy (E_{ph}) smaller than E_{ex} via different recombination processes including phonon emission processes.

In ideal semiconductors with no energy level inside the forbidden gap, electrons and holes recombine, respectively from the extrema of the CB and VB. This process is called band-to-band transition and the energy of the emitted photon is equal to the band gap energy of the material (Figure 4.1). When Coulomb interaction between electron and holes cannot be neglected, one should consider additional optical transitions due to the formation of excitons. For a free exciton, the energy of the emitted photon is smaller than E_g by an amount corresponding to the exciton binding energy E_b. The presence of defects or impurities in the crystal can lead to energy levels within the forbidden gap, which can contribute to various recombination processes involving excitons bound to ionised or neutral donors, band-acceptor and donor-acceptor recombination [89].
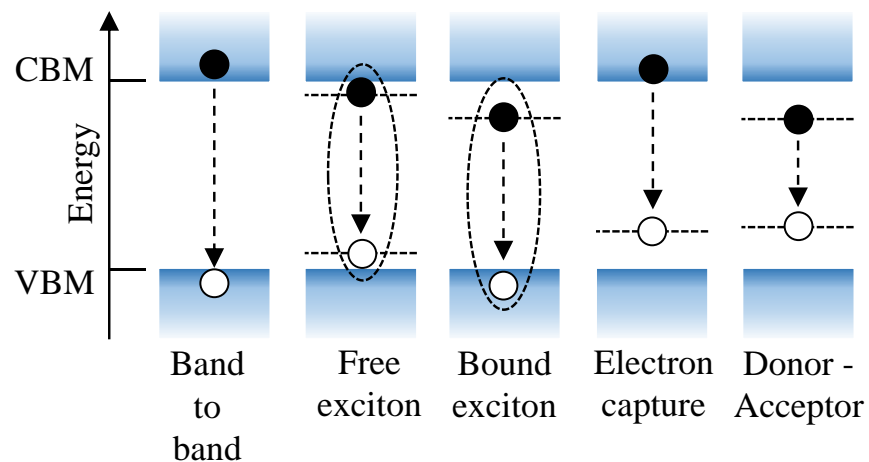
Figure 4.1. Schematics showing various carrier recombination processes in photoluminescence reproduced from Ref [90].

PL experiments can be used to gather useful information about the band gap energy and states in the forbidden gap due to impurities and defects [90]. For example, the PL linewidth and peak energy can reveal information about impurity type (acceptor or donor) and concentration, as well as thickness and composition of low-dimensional materials. Experiments can be conducted at

different temperatures and with temporal resolution (time-resolved PL) and used to extract useful information about radiative lifetimes and density of states [90].

The PL experiments in this project are conducted using a Horiba Jobin Yvon micro-PL system equipped with two laser sources: a 633 nm He-Ne laser and a 532 nm frequency doubled Nd:YVO$_4$ laser. Laser light is passed through an adjustable pinhole aperture and then through a beam splitter (Figure 4.2a). The laser is then focused onto the sample through an adjustable objective. A laser spot of diameter ~1 μm can be achieved allowing for the accurate measurement of distinct areas on a flake or heterostructure. Light from the sample is returned through the objective and is reflected from the beam splitter into a second pinhole aperture before passing through a filter to remove unwanted light from the sample. The light is then monochromated by the grating before finally reaching the detector. The second aperture blocks unwanted light from sources other than the sample area excited by the focused laser beam. Two types of detector are available in this system. A Charge-Coupled Device (CCD) detector and an indium gallium arsenide (InGaAs) array detector are used depending on the spectral range of interest: The CCD detector covers the range 350 to 800 nm and the InGaAs detector covers the range 800 to 1600 nm. A series of filters are used to reduce the power of the laser. Typically 1% of full power ($P = 15$ mW) is used for PL experiments to achieve a good signal without overheating and damaging the flakes. The grating of the detector can be set to either 150 or 1200 g/mm (grooves per mm) in order to control the spectral resolution. For PL experiments, broad emission peaks are generally observed so the 150 g/mm grating is favourable. The sample to be measured is placed upon a motorized *xy* stage allowing for sub-micron scale adjustments of the laser spot

position. For low-temperature µPL studies, the samples are held in vacuum and mounted inside a cold finger optical cryostat with a sapphire window of 1 cm diameter (Figure 4.2b). The samples are mounted on a copper plate by silver paint. The temperature within the cryostat is controlled by a continuous helium flux via a transfer tube from a He dewar with an external pressure regulator and is continuously monitored. By balancing the level of He flux against the output of the internal cryostat heaters (controlled by a Lakeshore LS331S temperature control unit), temperatures between $T = 8$ K and 300 K can be reached.
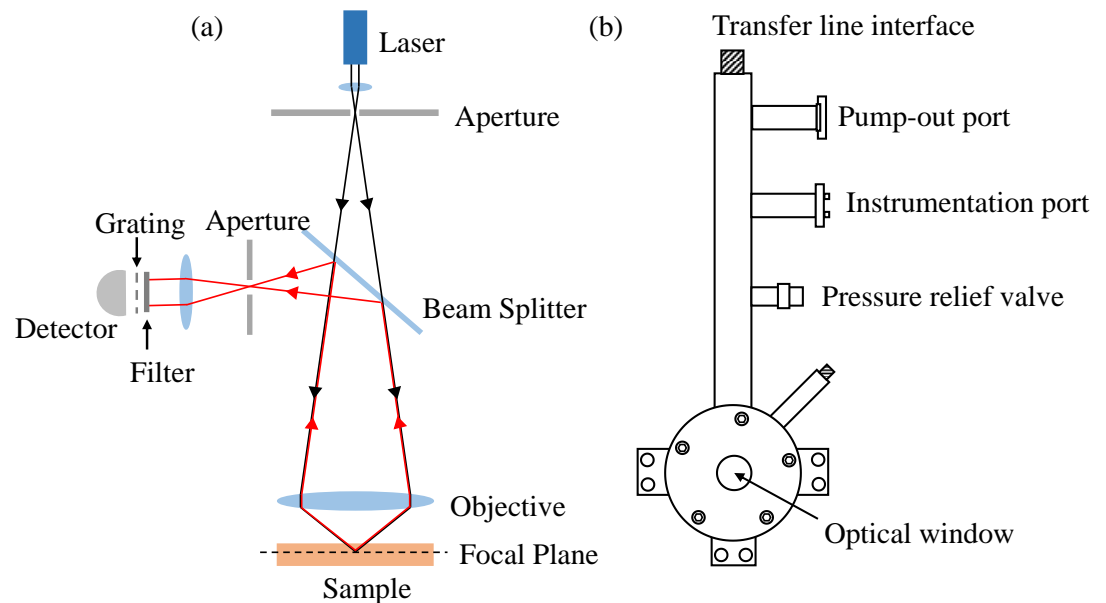
Figure 4.2. (a) Schematics of the confocal microscope system used for photoluminescence studies. (b) Schematics of a cold finger optical cryostat used for low-temperature photoluminescence studies.

4.1.2 Raman spectroscopy

Raman spectroscopy is based on the inelastic scattering of light by lattice vibrations (phonons). Figure 4.3 shows a representation of the Raman scattering process. In a first-order Raman process, a photon of energy $h\nu_i$ and wave vector k_i is scattered by one phonon of energy $E_q = \hbar\omega_q$ and wave vector q, which is

either excited or absorbed. Since energy and momentum are conserved, the energy of the scattered phonon can be described as $\hbar\omega_s = \hbar\omega_i \pm \hbar\omega_q$ and momentum as $\hbar k_s = \hbar k_i \pm \hbar k_q$. The positive and negative signs correspond to the phonon absorption (anti-Stokes component) and phonon excitation (Stokes component). Typically, the Stokes component is only detected as the probability of anti-Stokes processes is smaller. Raman spectroscopy can measure directly the phonon energies. The intensity of the Raman signal is generally expressed as a function of the wavenumber difference between the incident and scattered photon. Raman spectroscopy has been widely used to study the vibrational mode intensities and effect of strain applied to a crystal and has become a standard characterization technique for TMDCs, graphene and other layered materials [91]. The Raman spectra can be affected by any strain applied to the crystal, which can be identified by shifts in the Raman modes and/or variations in peak intensity [92]. In vdW heterostructures fabricated by dry transfer techniques, many interfacial defects or impurities can be present, resulting in strained layers. The ability to assess the strain makes it very useful for determining the sample quality.
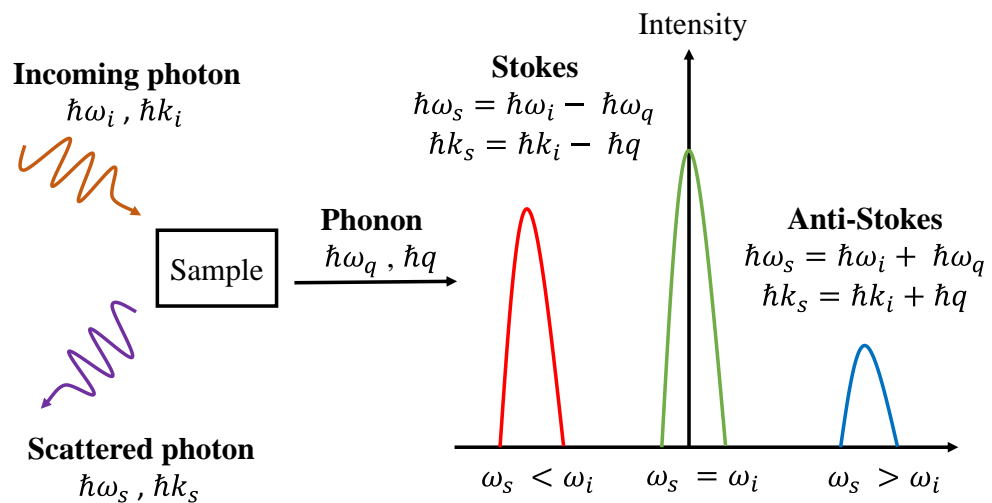
Figure 4.3. Representation of the Raman scattering process showing Stokes and anti-Stokes components.

The Raman spectroscopy experiments in this project are conducted within the same confocal microscope setup used for PL. Since in Raman spectra narrow peaks are observed over a small spectral range, the grating of the detector is set to 1200 g/mm (grooves per mm).

4.2   Surface characterisation

Various scanning probe techniques are used to resolve structures at the sub-nanometer level and are thus of particular interest for studying the surface of two dimensional materials. They offer the possibility to correlate morphology and structure with various significant electronic properties. These techniques typically involve an atomically sharp tip positioned close to a surface attached to a piezo-electric actuator which can execute motions with precision and accuracy at the atomic scale. Unlike optical and electrical transport techniques which average over the bulk of the material, these surface probe techniques help to understand the behaviour localised to the surface. Various surface techniques like atomic force microscopy (AFM), piezoresponse force microscopy (PFM) and Kelvin probe force microscopy (KPFM) have been used in this project to determine thickness of flakes, size of ferroelectric domains, presence of defects at the interface level, *etc.*

4.2.1 Atomic force microscopy

AFM measurements are conducted on two different setups, a NX20 AFM from Park systems and a MFP-3D AFM from Asylum Research in non-contact mode.

The Park NX20 system is equipped with a NuNano SPARK 350 AFM tip with a cantilever resonance frequency of ~ 350 kHz and force constant of ~ 42 N/m. The tip of radius ~ 18 nm upon a cantilever is brought close enough to interact with the sample in [93]. Upon the back of the cantilever, a mirror is positioned from which a laser beam is deflected into a photodetector. The cantilever-tip system oscillates at its resonant frequency via a piezo-electric component in close proximity to the surface of the sample. The cantilever behaves like an oscillating spring with an inherent force constant and resonant frequency. The tip is brought within an operating distance from the sample, which is typically in the range 10 – 0.1 nm for tip-sample interaction. At such distances, the atomic forces of the sample are sufficient to deflect the tip/cantilever and alter the resonant frequency of the system due to the attractive van der Waals force acting between the atoms of the tip apex and the sample surface. The amplitude of the tip/cantilever oscillation is more sensitive to the tip-sample distance. To probe the topography of the sample, the xy range is incrementally scanned in line segments. As variations in sample topography changes the tip-sample distance and the interaction forces, the amplitude change detects the sample topography. The oscillation amplitude measured at the operating frequency is used as feedback signal. The feedback controls movements of the z scanner during the imaging process to compensate for the deviations in the amplitude from the predefined setpoint. By maintaining a constant amplitude and distance, the z scanner reconstructs the sample topography (Figure 4.4). Typically the non-contact mode prevents the damage of the tip apex which can lower the spatial resolution and accuracy of roughness measurements.

The Asylum Research MFP-3D system is used with SCOUT 70 silicon AFM probe with a cantilever resonance frequency of ~ 70 kHz, spring constant of ~ 2 N/m and tip radius of ~ 5 nm.
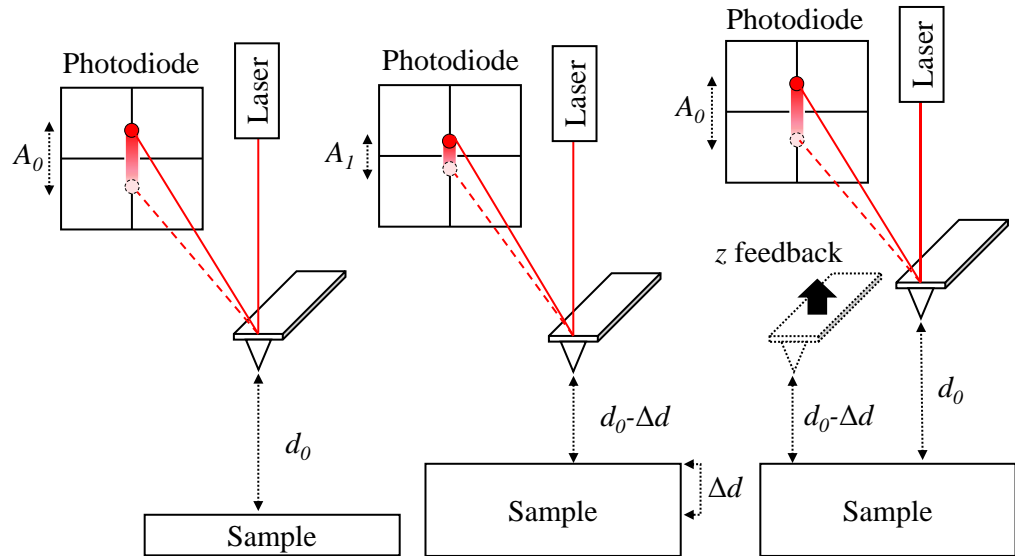
Figure 4.4. Tip-sample distance dependence of the oscillation amplitude and the *z* feedback in non-contact mode in AFM.
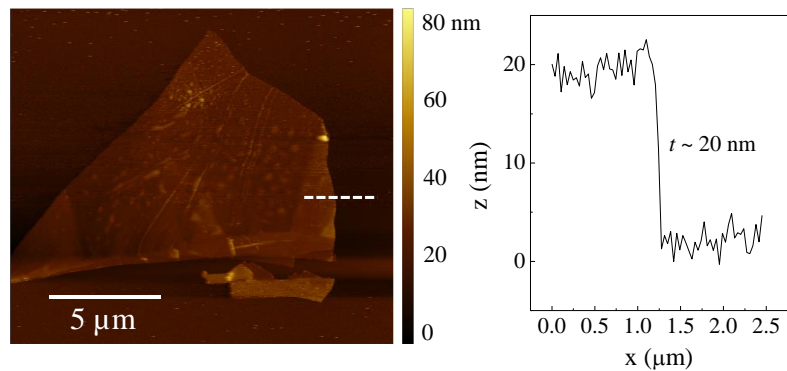
Figure 4.5. AFM image of a CIPS flake exfoliated on SiO_2/Si substrate. Inset: z-profile along the white dashed line shown in the AFM image.

4.2.2 Piezoresponse force microscopy

Piezoresponse force microscopy (PFM) is an extension of AFM which probes the electromechanical properties on the nanometer scale in addition to topography [94]. The PFM measurements are conducted using a Park NX20

setup under ambient conditions. This is achieved by bringing a conductive AFM tip in contact with the surface of a ferroelectric material and applying a pre-set AC voltage between the sample surface and the AFM tip (Figure 4.6). This results in an external electric field within the sample. The orientation of the polarisation in the sample if parallel to the applied electric field produces an in-phase PFM signal; whereas if the polarisation is oriented anti-parallel to the electric field, it produces an out-of-phase PFM signal. Thus the phase contrast between the two oppositely oriented vertical domains in the sample is 180°. The phase contrast between the applied AC bias and the piezo-electric response of the sample directly relates to the polarisation orientation in the sample. The amplitude on the other hand resolves the position of the domain walls where the response from the two oppositely oriented domains cancels out. For samples containing out-of-plane and in-plane polarisations, the vector PFM with vertical and lateral channels provide more complete information. The out-of-plane polarisation is estimated by tracking the vertical cantilever deflection and the in-plane polarisation can be determined from the lateral torsion of the cantilever. Using both these channels, a complete electromechanical response analysis is achieved. Besides domain imaging, PFM can be also used for switching ferroelectric domains by measuring the local PFM response and sweeping an additional DC bias between the tip and the sample surface. The polarity of the local ferroelectric domain below the tip aligns according to the sign and magnitude of the applied voltage. This gives a phase hysteresis loop revealing the particular voltage required to reverse the polarisation of the domains. One can perform an array of PFM signal vs. voltage spectroscopy measurements at

various locations for analysing the local switching behaviour of the ferroelectric domains.
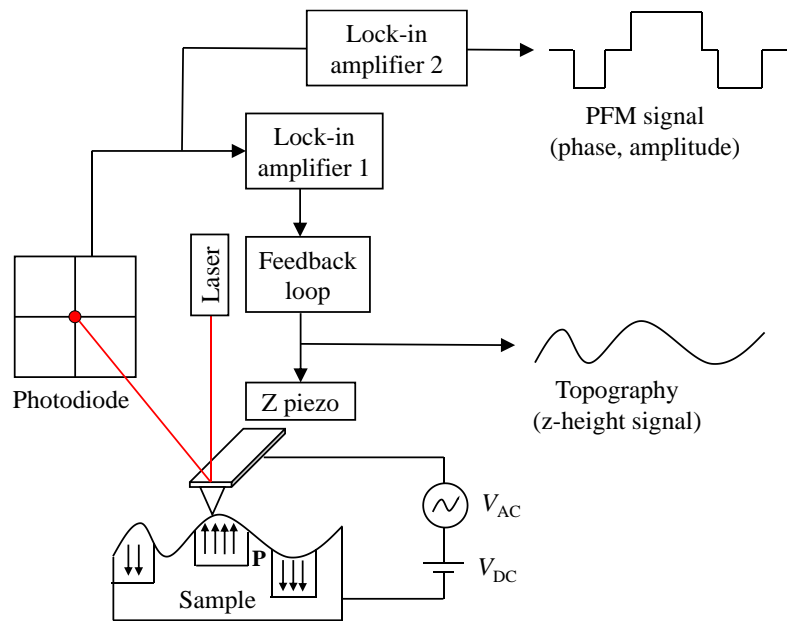
Figure 4.6. Schematic diagram showing the experimental set-up used for PFM imaging in contact mode.
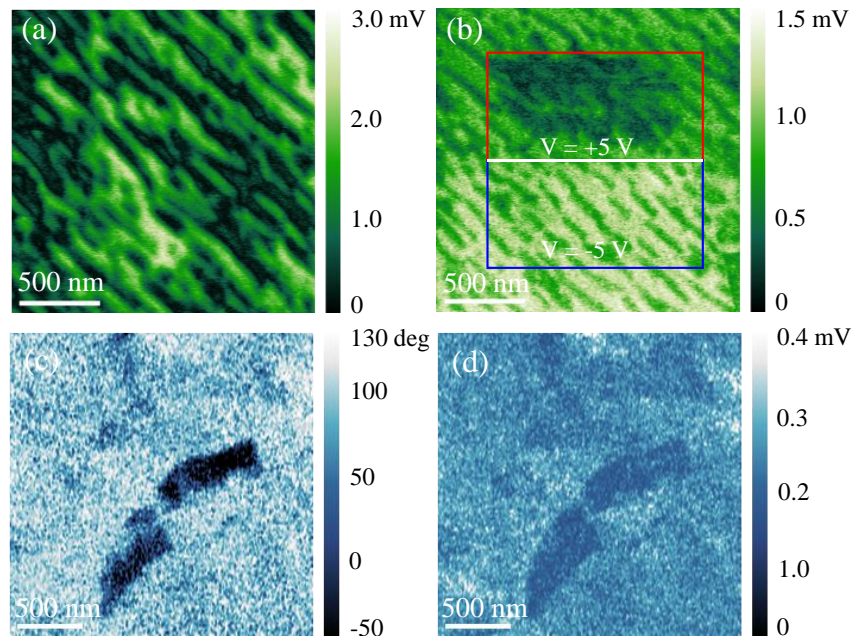
Figure 4.7. (a) PFM amplitude image of a CIPS flake ($t \sim 14$ nm) on Si-substrate (native oxide) before and (b) after biasing two regions at $V = \pm 5$ V. (c) PFM phase and (d) amplitude measurements of a α-In$_2$Se$_3$ flake ($t \sim 28$ nm) on Si-substrate (native oxide). PFM measured using a NuNano Spark 350 cantilever with $f_{AC} = 17$ kHz.

4.2.3 Kelvin probe force microscopy

Kelvin probe force microscopy (KPFM) is an electrostatic force microscopy technique to study the electronic surface properties of various conductive and semiconductive samples [95]. KPFM provides information regarding the local surface potential distribution, and if calibrated, the work function of the sample. The cantilever is mechanically excited while an AC voltage is applied to the tip and sample. Meanwhile a second lock-in-amplifier compensates the potential difference between the sample and the cantilever by applying an additional DC bias. Thus, the feedback signal is used to create a surface potential map.

The working of KPFM is based on the Fermi level alignment of the sample and the conductive AFM tip (Figure 4.8). Once an electrical contact is established, the Fermi level alignment leads to an offset in the vacuum levels, which introduces the contact potential difference V_{CPD}. This contact potential difference is compensated at each point of the scan by applying a DC bias that equals V_{CPD}.
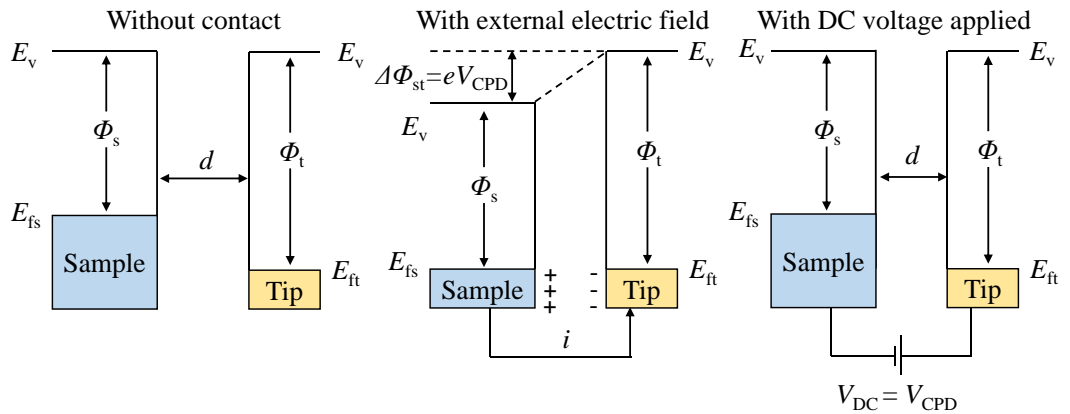
Figure 4.8. Energy level diagrams for the sample and tip in KPFM. KPFM applies V_{DC} to compensate for V_{CPD}. Φ_s and Φ_t are the work functions of the sample and tip, respectively. E_{fs} and E_{ft} are the Fermi levels of the sample and tip, respectively.

In amplitude modulated KPFM (AM-KPFM), the cantilever is mechanically excited to oscillate at its resonance frequency. The changes in amplitude for this oscillation controlled by the z scanner due to the attractive van der Waals forces between the tip and the sample gives the topography of the sample. At the same time a low frequency AC voltage is applied to the tip via a second lock-in amplifier. The AC voltage leads to a modulated electrostatic interaction force between the tip and sample. There is also an additional DC bias applied between the tip and the sample. The static DC term in the electrostatic interaction force is difficult to detect with sufficient signal-to-noise ratio. The second lock-in amplifier is used to decouple the AC term from the topography signal to detect the electrostatic tip-sample interaction force (Figure 4.9).
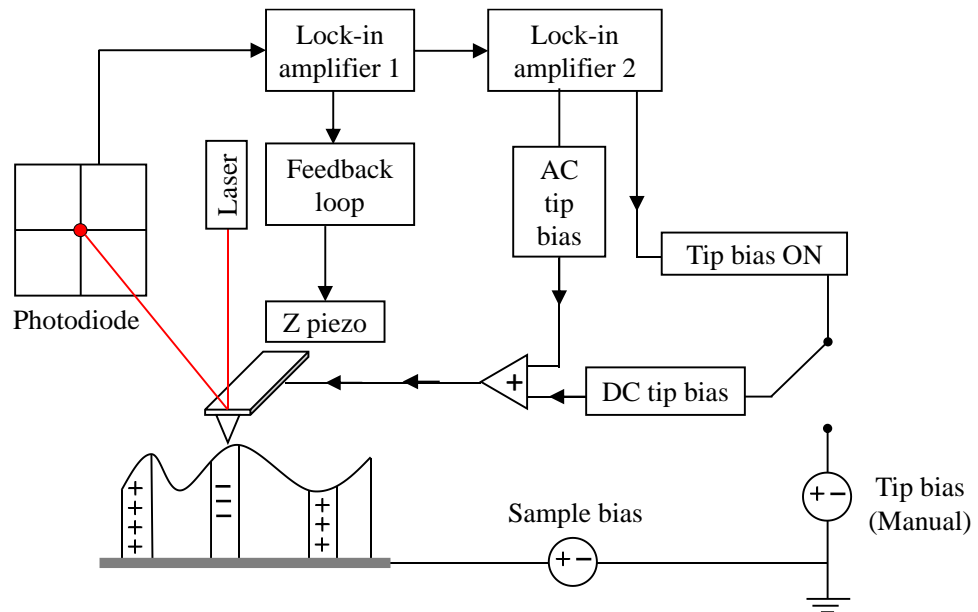
Figure 4.9. Schematic diagram showing the experimental set-up used for KPFM imaging.

AM-KPFM is measured using Park system NX20 setup under ambient conditions using Multi75E cantilever. Figure 4.10 shows typical AM-FPFM images of CIPS and α-In$_2$Se$_3$ on graphene.
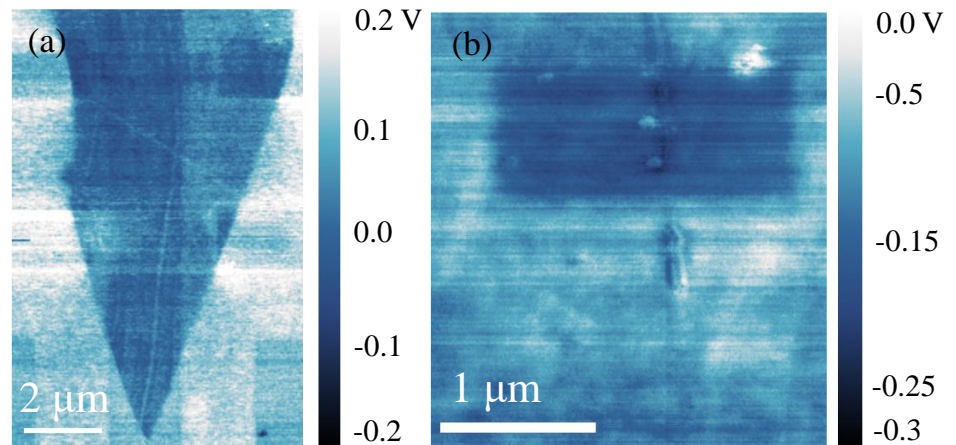
Figure 4.10. (a) AM-KPFM image of a CIPS flake on a SLG Hall bar. (b) AM-KPFM image of a α-In$_2$Se$_3$ flake exfoliated on CVD graphene. The dark area corresponds to the poling region with $V = + 10$ V. AM-KPFM is measured using a Multi75E cantilever with $V_{AC} = 4$ V and $f_{AC} = 17$ kHz.

4.3.   Transport measurements

Transport measurements are conducted on planar and vertical devices (Figure 4.11.) typically carried out after mounting the device in a homemade vacuum cryostat connected to a Pfeiffer turbo-molecular vacuum pump at 10^{-6} mbar pressure. The device is mounted by carefully positioning the pins on the header into a 12-pin socket of the cryostat. The device is electrically connected through the cryostat into a breakout box with BNC connectors corresponding to the 12-pins on the cryostat socket (Figure 4.12).

The planar devices discussed in this project are typically hybrid field effect transistors (FETs) consisting of a conducting channel (*e.g.* graphene) with source and drain contacts on either sides of the channel (Figure 4.11a). Some of these hybrid FETs consist of two sections: pristine graphene and CIPS/graphene. These are in a series resistance configuration with the same electrical current, *I* flowing through both of them. Thus by monitoring the voltage drop, *V* across different pairs of terminals along the graphene channel, we can study the

conductive properties of different materials simultaneously. The resistance can be measured by sweeping the gate voltage V_G, which leads to an electric field across the dielectric material (typically SiO_2). The vertical devices presented in this project are tunnel junctions (Figure 4.11b) with a thin layer of CIPS sandwiched between two electrodes made of few layer graphene (FLG).
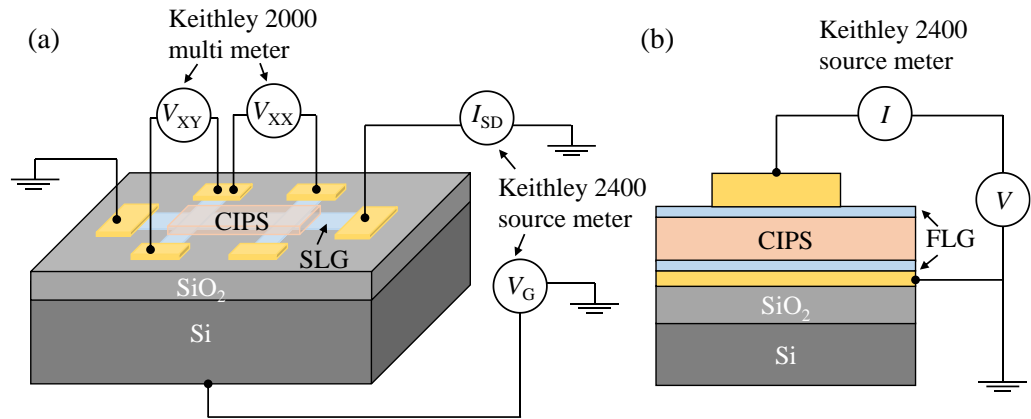
Figure 4.11. (a) 3D schematic of a four-terminal measurement of a graphene Hall bar device capped with a CIPS flake. (b) Schematic showing the cross-section of a CIPS-based tunnel device.

In a two terminal configuration, current voltage (*I-V*) measurements are performed using a Keithley 2400 direct current (DC) source meter using a ground plug to complete the circuit through the device and back to the source meter. The Keithley 2400 can be used to apply a voltage and measure the current simultaneously. It is also possible to ramp the applied voltage between user-defined setpoints to measure current as a function of the applied voltage.

For gate voltage measurements, a second Keithley 2400 source meter sweeps the voltage applied to the gate electrode typically in steps of 0.1 V. Sweeping the gate voltage too quickly can cause a build up of reactive current through the gate, thus damaging the device. The gate leakage current, I_G

(typically $I_G < 10$ nA) is monitored constantly and gives an indication of the stability of the gate.

Excessive leakage can lead to electrical breakdown as conductive pathways are formed between the gate electrode and the conducting channel of the device.

In a four-terminal configuration, a Keithley 2400 source meter is used to apply a constant current (typically ~ 1 µA) in the conducting channel and the resistance is measured by a Keithley 2000 multi meter to read the voltage drop between the contacts on the conducting channel. This eliminates the contact resistance associated with two-terminal measurements. In this configuration another Keithley 2400 source meter sweeps the back gate voltage.
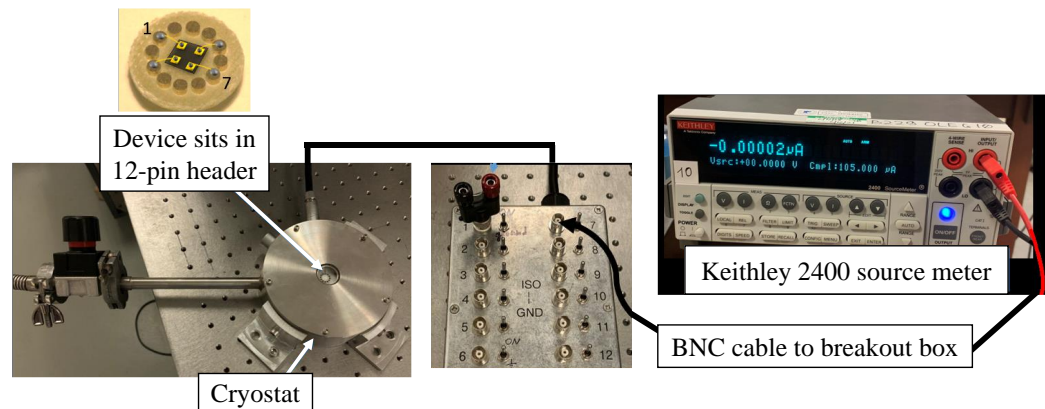
Figure 4.12. Schematic diagram with optical images of key components that are used for electrical measurements of the devices presented in this thesis.

A 405 nm collimated laser diode module from ThorLabs is used for transport measurements under light. It has an elliptical beam profile (3.8 mm × 1.8 mm) with power P ~ 4.5 mW, as measured using a ThorLabs optical power meter. It is placed at a suitable height for the laser to shine the optical window in the cryostat. A series of neutral density filters from ThorLabs with optical density OD1 to OD5 is used to vary the laser power on the sample.

To study the conductive properties of the devices at low temperatures, specialised equipment is used. A homemade bench-top cryostat with a 100 Ω platinum resistor (Pt100) is used to vary the temperature (Figure 4.13a). A Lakeshore 331, 340 or 350 temperature controller is used to provide PID controlled temperature stabilisation with heating power in the range between 2.5 mW and 25 mW. The cryostat is compatible with a home-made copper 'cold-finger' nitrogen bucket, which can be filled with liquid nitrogen to cool the system. Using this configuration, one can reach temperature down to ~ 100 K and heating up to ~ 500 K.

For magneto-transport studies, a Hall bar geometry is used. It consists of a graphene Hall bar with one section of the graphene capped by a CIPS flake. A current I_{SD} is applied across the graphene channel and the longitudinal voltage drop V_{XX} is measured along the direction of the current. The transverse or Hall voltage V_{XY} is measured in the presence of an externally applied magnetic field. The four-terminal, method as described before, is used to measure the Hall voltage. This is achieved by introducing a second Keithley 2000 multi meter so that both V_{XX} and V_{XY} can be measured simultaneously. A 'High T Mag' Cryogenics cryo-free closed cycle helium system is used to measure at high magnetic fields at temperature down to $T = 4$ K (Figure 4.13b). The sample is mounted into a probe, lowered into a liquid helium cooled cryostat and placed perpendicular to magnetic field at the centre of the magnet. This system produces a persistent magnetic field $B \leq 16$ T via a superconducting magnetic coil. The superconducting magnet is maintained at $T \approx 3$ K and is decoupled from the sample space. The maximum temperature that can be achieved in the sample space is $T \approx 400$ K. The magnetic field can be swept in the range from $B = -16$

T to $B = +16$ T at an average rate of ~ 0.283 T/min or held at a persistent field within that range.
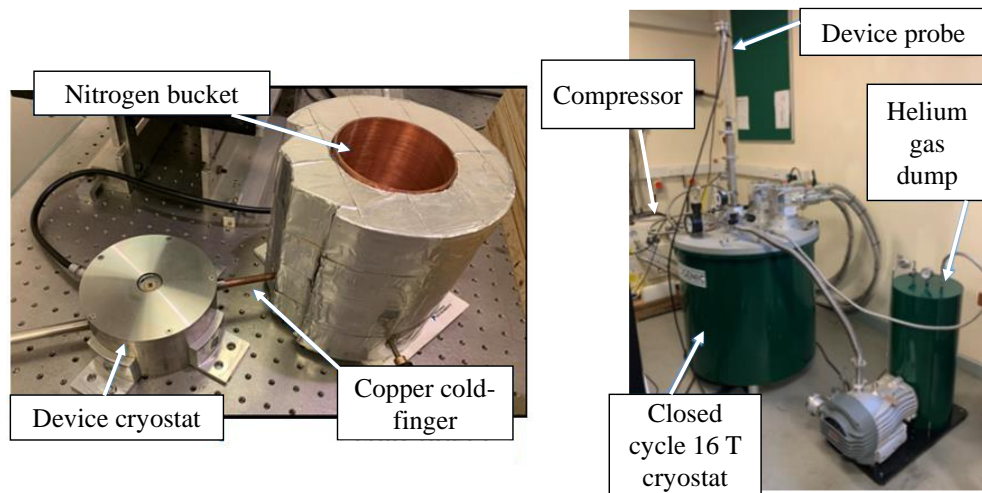
Figure 4.13. (a) Bench-top cryostat system for transport measurements in the temperature range of 100 K-500 K. (b) High-T Mag system for performing measurements at low temperatures and high magnetic fields.

Chapter 5

Optical studies of 2d van der Waals ferroelectric CIPS

This chapter reports on the optical and vibrational properties of bulk and thin layers of CIPS. Raman spectra at room temperature show well-defined peaks corresponding to different vibrational modes of CIPS. Photoluminescence (PL) experiments show broad emission bands due to defect states within the bandgap. The PL spectra are weakly affected by temperature and thickness of the CIPS flakes. These findings reveal the temperature behaviour of the CIPS optical response and are important for a full understanding of the CIPS-based devices presented in Chapters 6 and 7.

The studies in this chapter were conducted by myself. The work presented in this chapter was published in *2D Mater*. **9**, 035003 (2022).

5.1   Introduction

In recent years, CIPS crystals have been studied extensively due to their stable room temperature out-of-plane ferroelectricity and high Curie temperature ($T_c \sim 315$ K) in the bulk phase [24, 26]. The low phase transition temperature provides the possibility of modulating the optical properties of CIPS for device applications via temperature control [96]. Temperature dependent Raman spectroscopy has been used to study the phase transition from the ferroelectric to the paraelectric phase at $T_c \sim 315$ K [26]. It has been suggested that the coupling between the P_2S_6 deformation modes and Cu^I vibrations facilitates the motion of the Cu-ions, inducing ionic conductivity in CIPS. The effect of temperature and structural ordering on the optical absorption edge of CIPS crystals has also been studied. At high temperatures ($T > T_c$), the Cu-ions tend to

move into the interlayer van der Waals space. This leads to a paraelectric phase and an absorption band edge with a broad Urbach tail [29]. More recently, reports on temperature dependent photoluminescence, ultrafast nonlinear absorption and carrier relaxation in CIPS have provided further insights into the ferroelectric-paraelectric phase transition and the role of defects [97]. Here, we study the optical properties of CIPS in the bulk phase and thin flakes. CIPS flakes of different thickness were exfoliated from a bulk crystal and stamped onto 300 nm thick SiO_2/Si substrates under ambient conditions. These were then analysed using Raman and photoluminescence spectroscopy at different temperatures and optical excitation powers.

5.2   Raman spectroscopy

Figure 5.1 shows the Raman spectra at $T = 300$ K for bulk CIPS at different laser powers $P = 2\mu W$, $20\mu W$, $200\mu W$. The Raman peaks are observed at 103 cm^{-1}, 115 cm^{-1}, 317 cm^{-1}, 162 cm^{-1}, 214 cm^{-1}, 238 cm^{-1}, 266 cm^{-1}, 374 cm^{-1} and 450 cm^{-1}. These resemble closely those reported in the literature [16, 26, 98]. The cation (Cu and In) vibrational modes are usually found at low frequency (< 50 cm^{-1}) with the low and high frequency modes corresponding to vibrations of the Cu and In, respectively. The anion ($P_2S_6^{4-}$) vibrations corresponds to peaks at 103 cm^{-1} and 115 cm^{-1}. The peaks at 162 cm^{-1} and 214-266 cm^{-1} correspond to the deformations of the S-P-P and S-P-S bonds within the octahedra of CIPS, respectively. The peak present at 317 cm^{-1} is attributed to the distortions within the S_6 cage occupied by the Cu^{1+} ions. This is also closely related to the 266 cm^{-1} deformation mode. The peak at 374 cm^{-1} is attributed to P-P stretching; and the P-S stretching mode is centred at 450 cm^{-1}. Similar

Raman spectra were obtained from different regions of the crystal, suggesting a homogenous chemical composition of the CIPS crystal. Changing the laser power does not change the position of the Raman modes, as shown in Figure 5.1. It has been reported in the literature that when the temperature approaches $T_c =$ 315 K, the intensity of the P-P (~370 cm^{-1}), S-P-P (~160 cm^{-1}) and anion (~100 cm^{-1}) modes decreases and the distinct peaks corresponding to S-P-S vibration modes merge together [98].
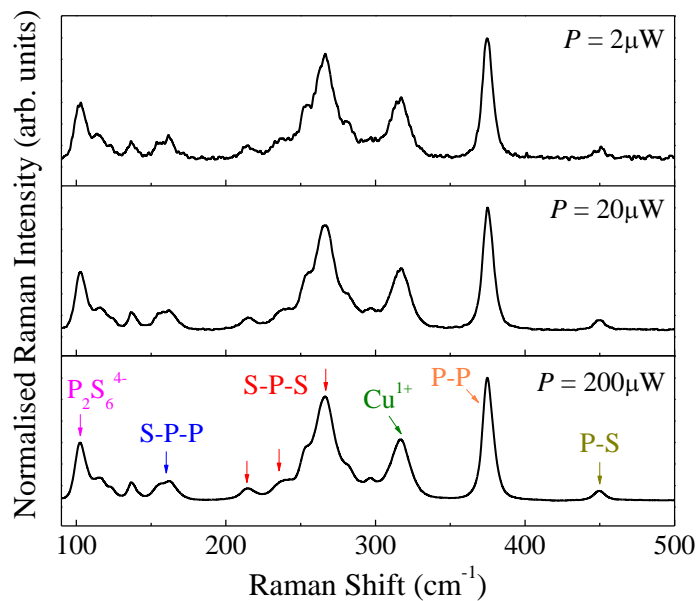
Figure 5.1. Normalized Raman spectra of bulk CuInP$_2$S$_6$ at laser powers $P =$ 200, 20 and 2 μW ($\lambda = 532$nm) using a 100x objective at $T = 300$ K. The spectra are normalized to the intensity of the 374 cm^{-1} Raman peak (P-P stretching mode).

For the exfoliated CIPS flakes, the thickness of the flakes is in the range $t = 14$ nm to 80 nm, as measured by atomic force microscopy (AFM). The Raman spectra of the flakes were measured with laser power $P = 200$ μW and objective 100x (Figure 5.2a). For the thinnest flakes, we have removed the background signal from the substrate, which introduces spurious Raman peaks at ~75, 300, 520 cm^{-1}. It can be seen that reducing the layer thickness has no significant

effects on the position of the Raman modes (Figure 5.2b). However, the modes at 266 cm^{-1} (S-P-S stretching mode) and 374 cm^{-1} (P-P stretching mode) reveal a small red shift, which we assign to laser-induced heating. To detect how the temperature of the sample affects the Raman signal, we selected a thin flake and performed Raman measurements before and after heating the flake by laser annealing. The laser annealing causes a small red-shift consistent with a thermal heating effect [16], as shown in Figure 5.2c.
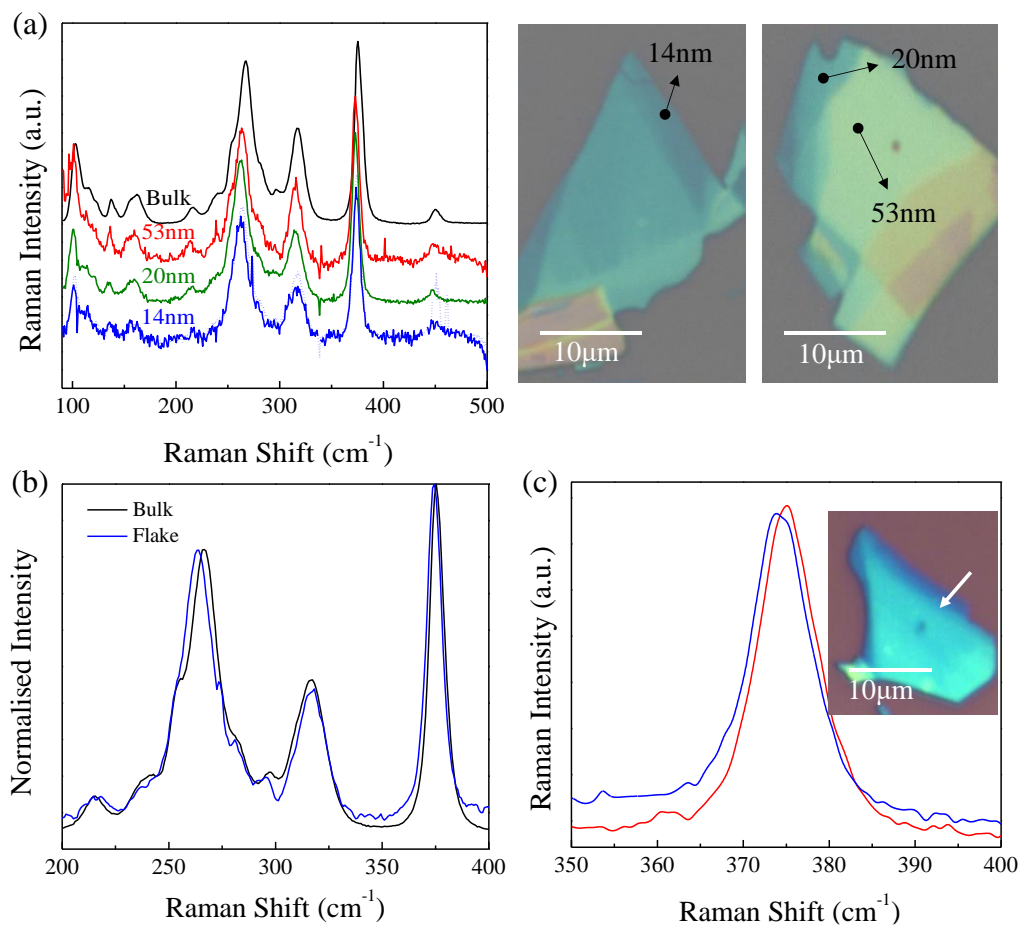
Figure 5.2. (a) Normalized Raman spectra for CIPS flakes at a laser power $P = 200\,\mu W$. ($\lambda = 532$ nm) using a 100x objective ($T = 300$ K). For clarity, the spectra are shifted along the vertical axis. Inset: Optical image of the CIPS flakes with varying thickness. (b) Raman spectra for bulk and 14 nm-thick flakes. The spectra are normalized to the intensity of the 374 cm^{-1} Raman peak (P-P stretching mode). (c) Raman spectrum before (red) and soon after laser annealing (blue) for a CIPS flake at a laser power $P = 200\,\mu W$ ($\lambda = 532$nm) using a 100x objective ($T = 300$ K). The laser annealing is conducted for 120 s at a laser power $P = 20$ mW. Inset: Optical image of the flake with the arrow indicating the location of the laser spot.

5.3   Photoluminescence

We probed the optical properties of bulk crystals and flakes of CIPS by PL over a range of temperatures from $T = 10$ K to 300 K. Figure 5.3a shows the temperature dependent PL emission spectra for bulk CIPS. The spectra show a multi-band emission with the main PL bands centred at around 1.5 eV and 1.9 eV, lower than the band gap energy of CIPS ($E_g = 2.7$ eV at $T = 300$K) [29]. When the temperature increases from $T = 15$ K to $T = 300$ K, the PL emission shifts to lower energy, as shown in the normalised spectra in the inset. This also shows that the PL band at around 1.5 eV becomes stronger than the band at 1.9 eV at low temperatures.
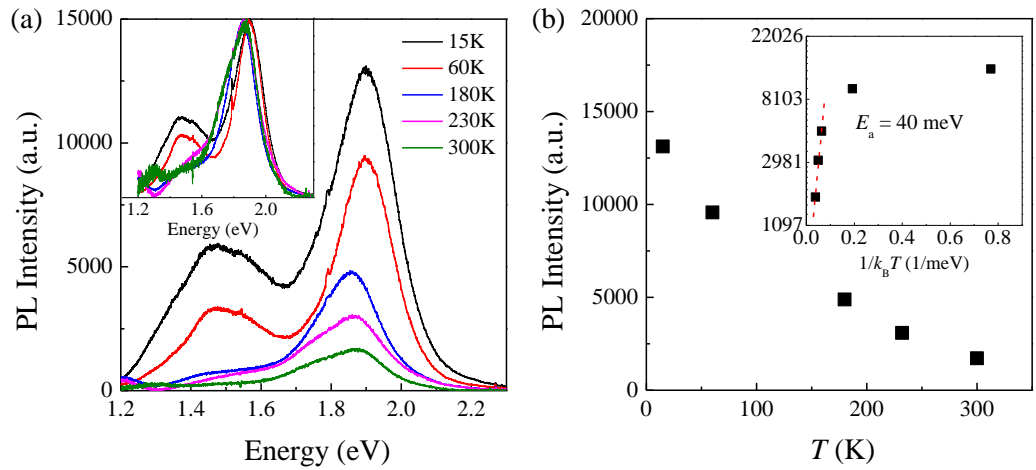
Figure 5.3. (a) Temperature dependent PL spectra for bulk CIPS measured at laser power $P = 2$ mW ($\lambda = 532$ nm) using a 50x objective. Inset: PL spectra normalised to the intensity of the 1.9 eV peak. (b) PL intensity of 1.9 eV peak extracted from (a) plotted against temperature. Inset: Arrhenius plot of the PL intensity versus $1/k_BT$, as extracted from (b).

The intensity of the PL band at 1.9 eV as a function of temperature is shown in Figure 5.3b. The gradual decrease in the PL intensity with increasing temperature can be described by a simple Arrhenius equation, $I \approx \exp(-E_a/k_BT)$, where E_a is the activation energy and k_B is the Boltzman constant. We find that $E_a = 40$ meV from a linear fit of the PL intensity in the region 15 K $< T <$ 180

52

K, as shown in the inset of Figure 5.3b. A similar activation energy was obtained from the study of the PL emission peak at 1.5 eV.

The temperature dependent PL emission spectra of a thin CIPS flake ($t \sim$ 20 nm) is shown in Figure 5.4a. The broad PL emission is centred at around 1.9 eV. As for bulk CIPS, this energy is much smaller than the direct band gap of CIPS. This indicates that the PL emission arises from defect-states within the band gap. The optical image of the flake is shown in the inset with the arrow showing the location of the laser spot. The PL peak intensity decreases exponentially with increasing temperature, as shown in Figure 5.4b. At low temperature ($T < 170$ K), there is a negligible change in the PL intensity. However, at $T > 170$ K, the intensity decreases significantly. By using the Arrhenius equation $I \approx \exp(-E_a/k_B T)$, and a linear fit to the data in the region of 240 K $< T <$ 300 K, we obtain a thermal activation energy $E_a = 55$ meV, as shown in the inset of Figure 5.4b.
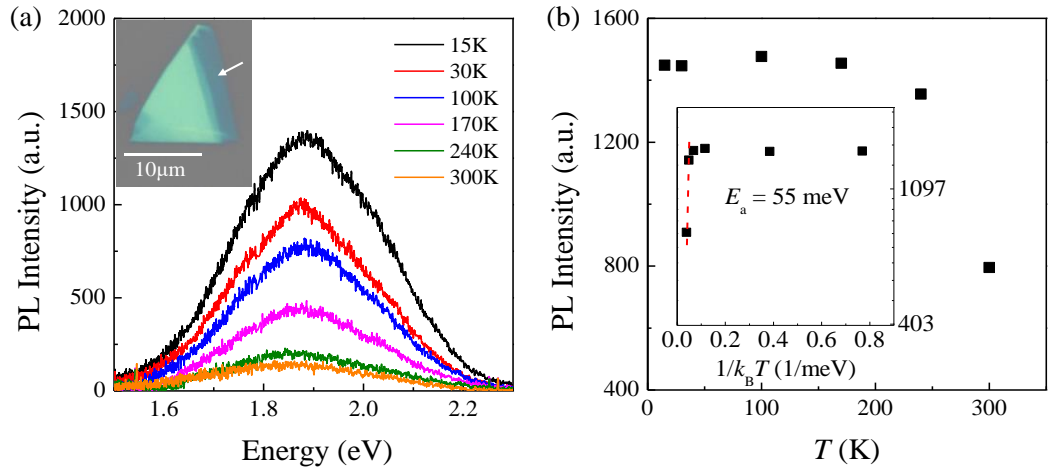
Figure 5.4. (a) Temperature dependent PL spectra for a CIPS flake ($t \sim$ 20 nm) measured at laser power $P = 2$ mW ($\lambda = 532$ nm) using a 50x objective. Inset: Optical image of the flake. (b) PL intensity extracted from (a) versus temperature. Inset: Arrhenius plot of the PL intensity versus $1/k_B T$, as extracted from (a).

Multi-peak fittings using Gaussian functions were applied to the PL spectrum taken at $T = 15$ K (Figure 5.5a). Three main peaks centred at 1.77 eV (full width at half maximum, FWHM of 0.28 eV), 1.87 eV (FWHM of 0.23 eV) and 2.01eV (FWHM of 0.25 eV) were obtained from the PL emission spectrum, indicating the existence of three different defect bands in the CIPS flake. Figure 5.5b shows the results of the Gaussian fits at different temperatures. This analysis reveals a small energy shift for the defect bands to higher energy as the temperature decreases. The broad spectra and weak temperature dependence are typical features of PL emission from deep-level defects [34, 99-101].
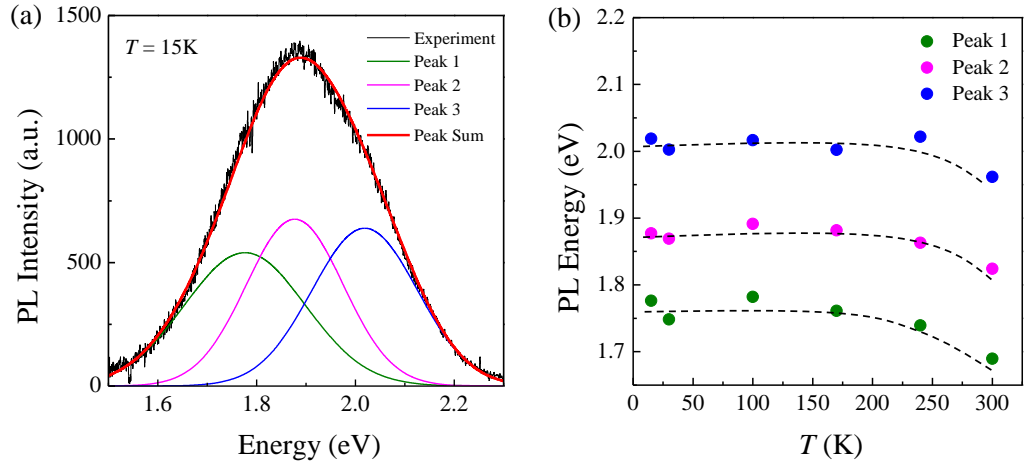
Figure 5.5. (a) Multi-peak fitting of the PL emission spectrum at $T = 15$ K for a CIPS flake. (b) PL energy of the sub-emission PL peaks, as extracted from (a) plotted against temperature. The dashed lines are guides to the eye.

The energy peak position of the PL emission of bulk and thin flakes is weakly affected by temperature, shifting by about 20 meV to high energy with decreasing T from 300 K to 10 K, as shown in Figure 5.6. The thermal shift of the energy peak position is significantly smaller than that measured for the band gap over the same temperature range ($\Delta E_g \sim 100$ meV) [29]. The corresponding PL intensity increases by a factor of ~ 10. Flakes of CIPS show broader emissions and a similar weak T-dependence. The specific form of the PL

spectrum can change from flake to flake, but always reveals broad PL emissions at similar energies.
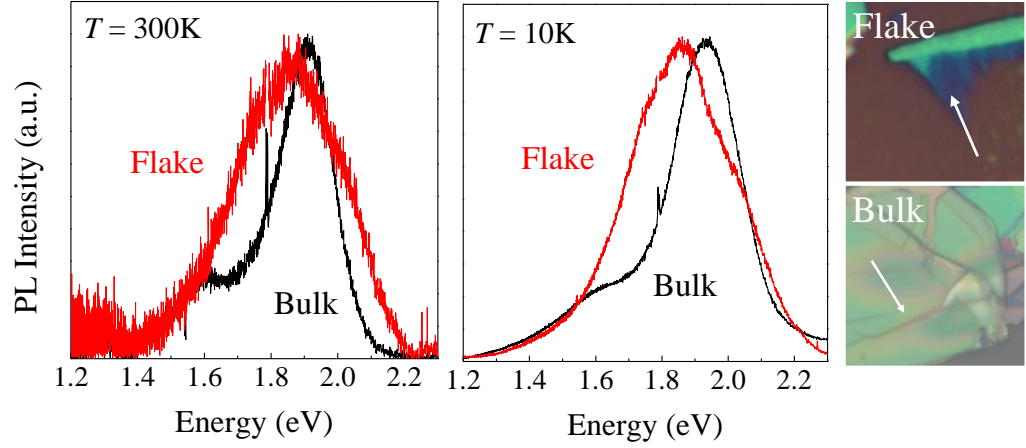
Figure 5.6. Low (10 K) and room (300 K) temperature normalized PL spectra for a bulk crystal and a thin (12 nm) flake of CIPS at a laser power $P = 2$ mW ($\lambda = 532$ nm) using a 50x objective. Inset: Optical images of the bulk and thin ($t \sim$ 12 nm) CIPS flake with arrows indicating the location of the laser spot.

To further explore the PL emission, we have conducted the PL experiments at different excitation powers. Figure 5.7a shows the PL emission of bulk CIPS at different laser excitation powers at $T = 15$ K. It shows a gradual increase in the PL intensity as the laser power increases from $P = 2$ μW to $P = 2$ mW. The position of the PL bands around 1.5 eV and 1.9 eV is unaffected by the change in the excitation power. This is shown in the normalised spectra in the inset of Figure 5.7a. The PL peak intensity at around 1.9 eV tends to saturate at high excitation powers (Figure 5.7b). A similar trend is observed at $T = 300$ K. The peak intensity (I) as a function of the excitation power (P) can be described by $I = P^c$, where c is a constant. We estimate values of $c = 0.71$ and $c = 0.42$ for $T = 15$ K and 300 K, respectively.
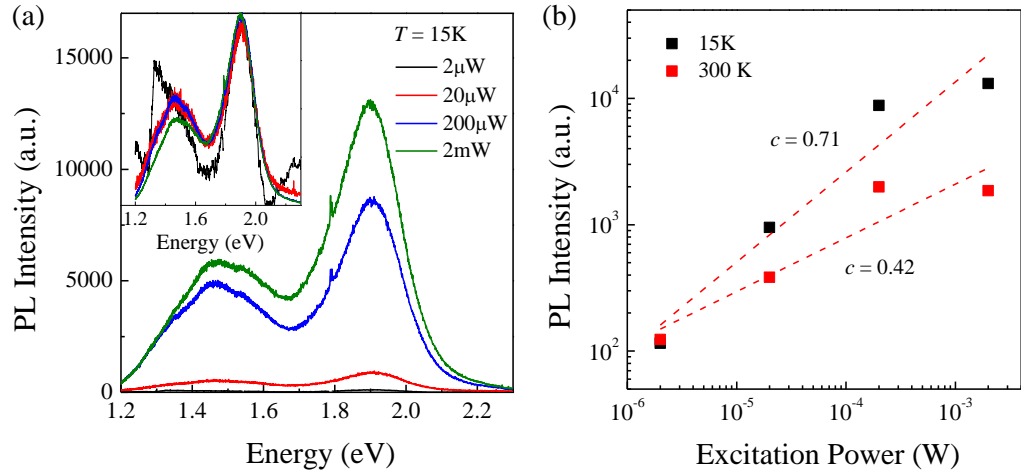
Figure 5.7. (a) Power dependence of the PL emission for bulk CIPS at $T = 15$ K with an excitation wavelength of $\lambda = 532$ nm using a 50x objective. Inset: PL spectra normalised to the intensity of the 1.9 eV peak. (b) The intensity of the PL peak at 1.9 eV versus excitation power at $T = 15$K and $T = 300$K. The dashed lines represent fits to the data by a power law P^c.

For a thin CIPS flake of thickness $t \sim 12$ nm, a similar behaviour was observed at $T = 10$ K (Figure 5.8a). The PL spectra shows a broad emission peak centred at around 1.9 eV. Normalised spectra in the inset show no shift in the PL signal. When the peak intensity at 1.9 eV is plotted against the excitation power, using $I = P^c$, we estimate $c = 0.87$, as shown in Figure 5.8b.
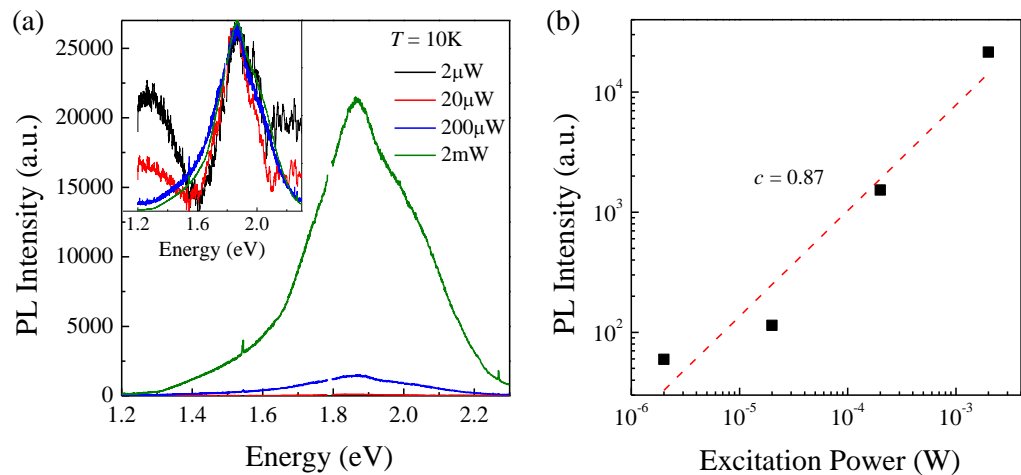
Figure 5.8. (a) Power dependence of the PL intensity for a thin CIPS flake ($t \sim 12$ nm) at $T = 10$ K with an excitation wavelength of $\lambda = 532$ nm using a 50x objective. Inset: Normalised PL spectra. (b) The intensity of the PL peak around 1.9 eV versus excitation powers at $T = 10$ K. The dashed line represents a linear fit to the data.

The saturation of the PL intensity suggests that the recombination process involves a transition from a bound state. As the excitation power increases, the bound states are increasingly occupied, resulting in a saturation of the PL intensity. This also suggests the existence of defects and/or impurities [100, 102] with optical transitions below the absorption edge (2.8 eV) [97]. The excitation of the defects below the gap of CIPS using $\lambda = 532$ nm reveal several defect-related bands. Nonequilibrium charge carriers can undergo relaxation processes within these defect bands before carrier recombination. Heating results in the decrease of the PL emission intensity. This relates to the fact that there is a nonradiative recombination channel *via* carrier-phonon scattering for the relaxation of nonequilibrium carriers, besides the radiative recombination channel. This carrier-phonon scattering increases as temperature increases [103], resulting in the increase in the nonradiative recombination. The weak temperature dependence of the defect band excitation also has been observed by Yan *et al.* in time-correlated single photon counting experiments [97].

Previous studies of the absorption spectrum of CIPS and its temperature dependence have revealed an extended Urbach tail near the absorption edge [29]. This is present in both the paraelectric and ferroelectric phase and becomes more prominent as the temperature increases [29]. In the low photon energy range, the spectral dependence of the absorption coefficient (α) on the photon energy ($h\nu$) is known as the empirical Urbach rule given by $\alpha = \alpha_0 \exp(h\nu/E_U)$, where α_0 is a constant and E_U is the Urbach energy. The optical emission spectrum $PL\ (h\nu)$ for a system of energy levels in thermal equilibrium can be linked to the absorption $\alpha(h\nu)$ according to the simple relation $PL(h\nu) \sim \alpha \exp(-h\nu/k_B T) \sim \alpha_0 \exp(h\nu/E_U) \exp(h\nu/k_B T)$. The value of E_U is related to the width

of the distribution of localized energy states in the forbidden band gap and for CIPS it corresponds to a value of about 50 meV at $T = 300$ K [29]. The Urbach tail is common in materials that have localized states in the forbidden gap due to intrinsic or extrinsic phenomena [104]. For CIPS, the Urbach tail has been assigned to the structural disorder associated with the different positions of the Cu-atoms within the crystal [29]. At low temperature ($T < 243$ K), the Cu-atoms tend to occupy the positions in the crystal that are displaced upwards from the centre of the S_6 octahedron ($Cu1^u$). In this temperature range the absorption edge arises from the direct allowed optical transitions. As the temperature increases, the population of $Cu1^u$ decreases and the downward position ($Cu1^d$) begins to be occupied. This leads to a broadening of the optical absorption edge and thermal expansion of the lattice. At the phase transition temperature, $T_c = 315$ K, the $Cu1^u$ and $Cu1^d$ positions become equivalent and the spontaneous polarisation vanishes. At $T > T_c$, the Cu-atoms not only moves within the vdW layer but also in the interlayer space [29, 75]. Thus, it is possible that the defect related PL bands revealed in our experiments may arise from the structural disorder in the crystal and their energy peak position and intensity can be affected by the thermal motion of the Cu-atoms as T increases.

5.4   Summary

We have obtained the characteristic Raman modes for CIPS, as reported in the literature for bulk CIPS. There is no significant change in the spectra with the thickness of the flakes. However, for thin flakes, we observe a small red shift of specific modes, which we assign to laser induced heating. The PL emission studies have shown the existence of localised states within the forbidden gap of

CIPS. These localised states exist in both bulk and nanometer-thick flakes and show broadband defect-assisted emission when excited with laser light of wavelength $\lambda = 532$ nm below the band gap energy. As the temperature increases, there is a small red shift of the PL emission for both bulk and nanometer-thick flakes. This is also marked by a decreasing PL emission intensity due to enhanced phonon scattering with increasing temperatures. The red shift can also be seen in the individual defect-bands extracted by Gaussian fitting of the PL emission for a thin flake. It is important to note that the shift occurs at $T \sim 250$ K, which correlates to the temperature required for the activation of thermal motion of Cu-ions leading to a progressive increase in disorder and ionic conductivity in CIPS, as reported in the literature [29, 75]. The PL emission spectra also depend on the excitation power. With increasing power, the PL peak intensity saturates, suggesting the existence of defect-induced bound states in the crystal. Thus, the results presented in this chapter provides evidence of structural disorder in the CIPS crystal and helps to understand how the temperature dependent Cu-ion motion can affect its optical properties. These results are also relevant to the studies of the devices based on CIPS-graphene heterostructure as described in the subsequent chapters.

Chapter 6

Memristive effects in graphene induced by CIPS

This chapter reports on hybrid field-effect transistors based on CIPS/graphene heterostructure in which a graphene conducting channel is gated through a CIPS layer. These devices use graphene as a sensitive probe to study the polarisation and charge transfer phenomenon at the CIPS/graphene interface. The transfer characteristics of these FETs reveal hysteretic and memristive effects, which are sensitive to gating, temperature and light illumination. The electrical properties of thin CIPS layers have been studied by considering tunnel junctions (TJs) in which a CIPS layer is embedded between two few layer graphene (FLG) electrodes. The transport characteristics show an interplay between charge transfer and ferroelectric polarisation influenced by temperature. A range of functionalities observed in these types of devices can open up new opportunities for the development of electrically and optically controlled memristive devices.

The hybrid FETs studied in this chapter were fabricated by Dr. Wenjing Yan at the Institute of Semiconductors in Beijing, China. The devices were processed by at the Nanoscale and Microscale Research Centre (nmRC) in University of Nottingham. The TJs were fabricated at the National Graphene Institute, Manchester by Dr. Nilanthy Balakrishnan. The electrical and optical studies were conducted by myself. The work related to this chapter was published in *2D Mater*. **9**, 035003 (2022).

6.1 Field effect transistors (FETs) based on CIPS/graphene heterostructures

6.1.1 Introduction

Within the family of vdW ferroelectrics, CIPS has gained particular attention over the years and has been used in combination with other 2D materials to realise ferroelectric field effect transistors (FeFETs) [10, 16, 31, 105-107], negative capacitance transistors [33, 108], photodetectors [34], memristors [36] and devices for energy applications [37, 38].

Combining graphene with 2D ferroelectrics offers a technique to switch the ferroelectric polarisation by modifying the electrostatic potential at the graphene/ferroelectric interface [21, 35, 109]. Despite this, the mechanisms behind the resistive switching of CIPS-based devices remain poorly understood. Thus, systematic studies of CIPS under different conditions, such as electric field, temperature and light can help to unravel the complex interplay between various hysteretic effects caused by ferroelectric polarisation, ionic conductivity, crystal defects, etc. [110].

Here we study the memristive effects in a multi-terminal FET that comprises of a pristine graphene section and a section with a CIPS flake lying underneath the graphene layer. The CIPS/graphene heterostructure shows significantly different electrical and optical properties compared to those of the pristine graphene.

6.1.2 Room temperature memristive effects in CIPS/graphene FETs

Figure 6.1 shows two sections of the CIPS/graphene FET comprising of pristine graphene (PG) and the CIPS/graphene heterostructure (CG) in a series resistance configuration with the same electrical current, I, flowing through both of them. Thus, by monitoring the voltage drop, V, across different pairs of terminals along the graphene channel, we study simultaneously the conductive properties of PG and CG (Figure 6.1a). The I-V curves of the PG and CG layers are ohmic. The corresponding longitudinal resistance, R, was measured over a range of gate voltages V_G applied between the graphene and the Si-gate electrode (Figure 6.1b).
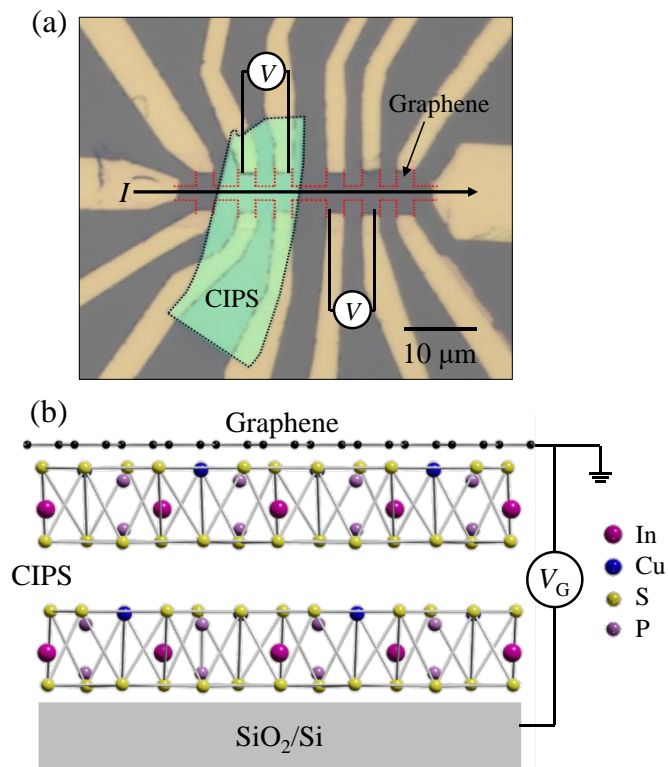
Figure 6.1. (a) Optical image of CIPS/graphene multi-terminal field effect transistor on a SiO_2/n-Si substrate. Red and black dashed lines mark the edges of the graphene and CIPS layers, respectively. The thickness of the CIPS flake is $t = 50$ nm. (b) Schematic showing the CIPS/graphene heterostructure and crystal structure of graphene and CIPS. The gate voltage V_G is applied between the graphene and the Si-gate electrode.

Figure 6.2a shows the $R(V_G)$ curve for different sections of the FET at $T =$ 300 K. Pristine graphene shows a maximum in the longitudinal resistance, R, around gate voltage $V_G = 5$ V corresponding to the charge neutrality point V_{NP} of the graphene Dirac cone (shown as dashed lines in Figure 6.2a). This shows that the pristine graphene layers are p-type doped. We estimate a hole density p $= 3.2 \times 10^{11}$ cm^{-2} at $V_G = 0$ V. The electron and hole mobilities are $\mu = 4.6 \times 10^3$ cm^2/Vs and 4.2×10^3 cm^2/Vs at $T = 300$ K, respectively. The slight asymmetry in electron and hole mobility relates to the attractive versus repulsive scattering of carriers by charged impurities in the substrate and/or on the surface of graphene due to unintentional doping of CVD graphene [111, 112]. For CG, the curve is shifted to lower V_G compared to PG. The shift is accompanied by a shift in the graphene charge neutrality point ($\Delta V_{NP} = 9$ V) for a gate voltage sweep of ΔV_G $= \pm 20$ V. The $R(V_G)$ curve is acquired starting from $V_G = 0$ (mark 1 in Figure 6.2a), continuing with a sweep of V_G to a maximum $V_G = + 20$ V (mark 2), passing through $V_G = 0$ V again along the way down (mark 3) to a minimum V_G $= -20$ V (mark 4).

As shown in Figure 6.2b, the temporal response of the resistance at $V_G = 0$ V is slow (with rise and decay times of $\tau > 100$ s) and different following a sweep down or a sweep up of V_G. Thus, our data indicate that CIPS modulates the carrier density of the graphene layer, inducing an n-type doping at $T = 300$ K. To date, both p-type and n-type doping of graphene and hysteretic behaviours have been reported in different FE/graphene heterostructures [113-119]. Here, we examine the nature of the doping and hysteresis in the CIPS/graphene heterostructure by considering the dependence of the hysteresis on the gate

voltage, the time scale at which this takes place, and its dependence on temperature and light illumination.
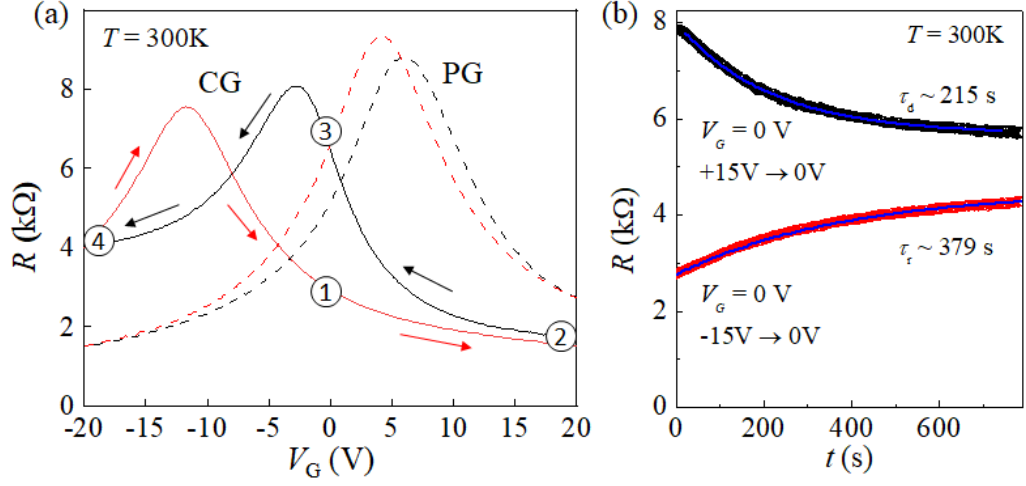
Figure 6.2. (a) Transfer curves $R(V_G)$ of pristine graphene (PG) (dashed line) and CG (solid line) for the sweep up (red) and sweep down (black) branch at $T = 300$ K ($I = 1\mu$A). Four data points (1-2-3-4) are marked sequentially on the $R(V_G)$ curve. (b) Temporal response of R for CG ($T = 300$ K). Blue lines are fits to the data by an exponential curve with decay time τ_d and rise time τ_r. Measurements were conducted at $V_G = 0$ V following a sweep down (black curve) or sweep up (red curve).

Non-volatile resistance switching and memristive effects can arise from ferroelectric polarisation in CIPS. For example, as sketched in Figure 6.3a, a positive gate voltage ($V_G > 0$ V) on the Si-gate electrode can induce a ferroelectric polarisation in the CIPS layer that points upward, thus modulating the carrier density in the graphene layer. An opposite FE polarisation should occur instead for $V_G < 0$ V. The dynamics of reversal of ferroelectric polarisation is much faster than the time scale considered in our study. In general, hysteresis due to a FE polarisation should produce a shift of the Dirac point in the direction of the sweep [120], *i.e.* the neutrality point V_{NP} should shift to higher voltages when V_G is swept from negative to positive values compared to when V_G is swept from positive to negative values. Memristive effects and resistance switching

can also originate from other mechanisms, including electronic and/or ionic conduction in the FE layer. The ionization of dopants and/or a slow motion of ions within CIPS can be triggered by a large applied electric field and/or at high temperatures [28]. These can affect the conductivity of graphene through a charge transfer at the CIPS/graphene interface, as sketched for different V_G in Figure 6.3b.
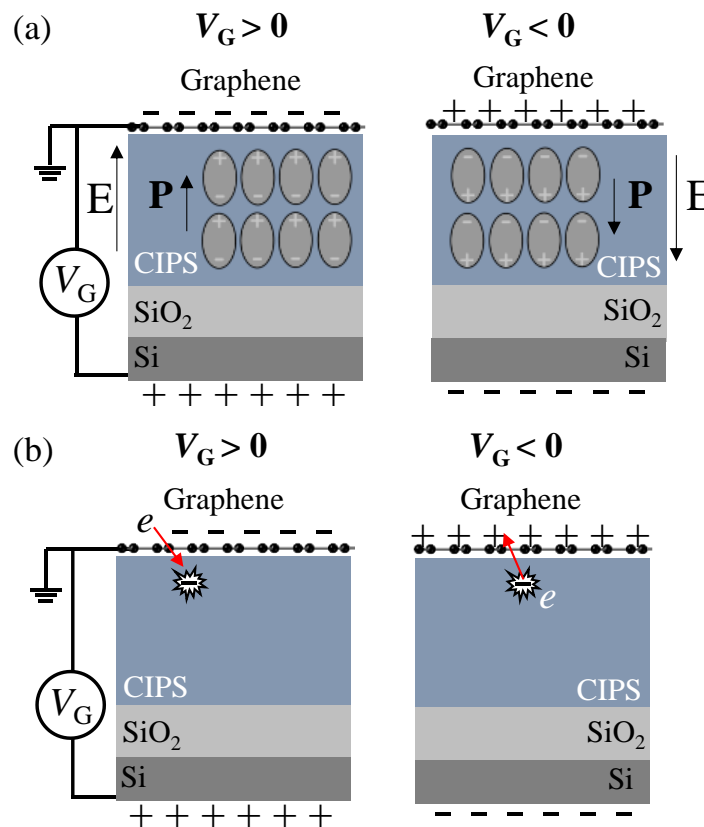
Figure 6.3. (a) Schematic of the ferroelectric polarisation in CIPS induced by a positive (left) or negative (right) V_G applied to the Si-gate electrode. The induced polarisation **P** is parallel to the external electric field **E**. (b) Schematic of the charge transfer mechanism at the CIPS/graphene interface mediated by traps in the CIPS layer under a positive (left) or negative (right) V_G.

6.1.3 Charge transfer at the CIPS/graphene interface

As shown in Figure 6.4a, the amplitude of the hysteresis, as measured by ΔV_{NP}, decreases with decreasing sweep voltage range. This is related to the decrease in charges transferred at the CIPS/graphene interface which leads to a

small hysteresis at low voltages. The $R(V_G)$ curves do not indicate a well-defined switching gate voltage. Also the amplitude of hysteresis decreases as the sweep rate increases (as shown in Figure 6.4b). Such an observation is not consistent with an electric field induced ferroelectric polarisation.
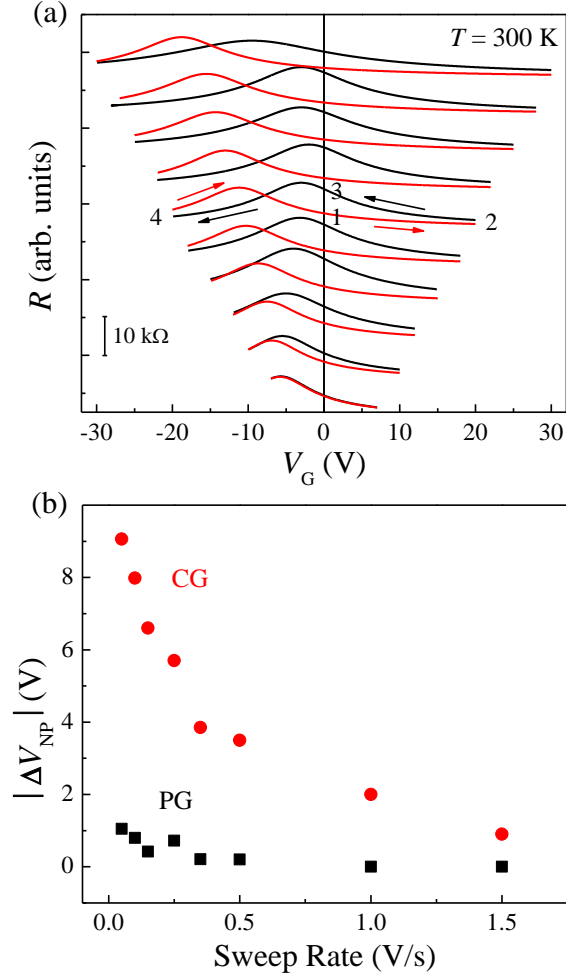
Figure 6.4. (a) Transfer curves $R(V_G)$ for CG at $T = 300$ K ($I = 0.3$ μA). The sweep up/down branches are shown in red and black, respectively. Curves are displaced along the vertical axis for clarity. (b) The dependence of the amplitude of ΔV_{NP} on the sweep rate, with maximum V_G of 15 V.

The direction of hysteresis can be explained using Figure 6.5. In the first part of the sweep of V_G to positive gate voltages ($V_G > 0$ V), negatively charged defects are created in CIPS by capture of electrons from the graphene layer. During the reverse sweep with $V_G < 0$ V, due to the negative gate potential, holes

drift toward the interface and neutralize the defects. Thus, the hysteresis is caused by trapping of charges in the CIPS layer. The gate voltage induces charges in the graphene layer, which then redistribute between graphene and CIPS. This time-dependent slow process causes a hysteresis in the transport characteristics that depends on the sweep rate and the range of the gate voltage.
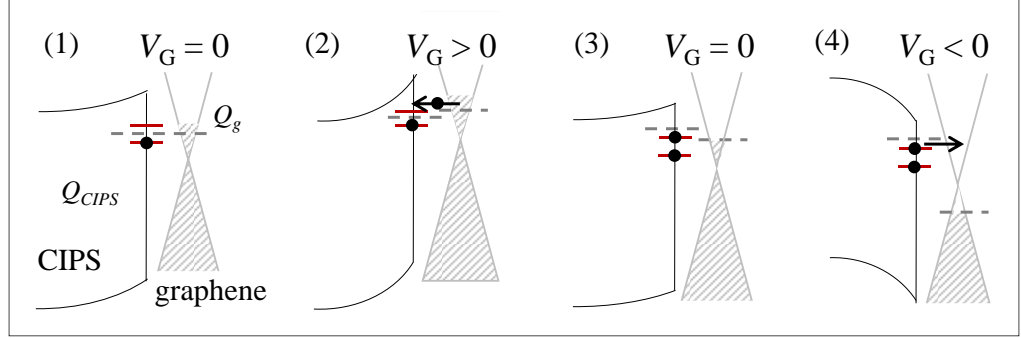
Figure 6.5. Band bending for CG. The electron affinity of graphene and CIPS is $\chi_{Gr} = 4.5$ eV and $\chi_{CIPS} = 3.7$ eV, respectively [35]. At $V_G = 0$ V, equilibrium is achieved by transfer of electrons between CIPS and graphene, inducing a depletion layer and an upward bend of the CIPS conduction band near its interface with graphene. Black dots correspond to trap charges and red lines illustrate the energy level of the traps. Different band alignments and charge transfers correspond to values of V_G marked as 1-2-3-4 in panel Figure 6.4a.

6.1.4 Modelling charge transfer at the CIPS/graphene interface

To account for the hysteresis in $R(V_G)$ due to a charge transfer at the CIPS/graphene interface, we consider a classical capacitance model [121]. A gate voltage increment ΔV_G generates an incremental increase in charge ΔQ in the CIPS/graphene heterostructure, which can be described as $\Delta Q = C\Delta V_G$, where ΔQ is the sum of free charge carriers in the graphene layer (ΔQ_g) and charges bound onto localized states of CIPS (ΔQ_{CIPS}), and C is the capacitance of the SiO$_2$ layer. Here, we assume that the charge ΔQ redistributes between the graphene (Q_g) and the CIPS (Q_{CIPS}) layers with an effective time constant τ, *i.e.*

$$Q_g = \Delta V_G C \exp\left(-\Delta t / \tau\right) \tag{6.1}$$

Thus, the charge stored by CIPS in a time interval Δt can be described by,

$$\Delta Q_{CIPS} = \Delta V_{\mathrm{G}} C \left[1 - \exp\left(-\Delta t / \tau \right) \right] . \qquad (6.2)$$

The charge in CIPS causes a potential difference between the CIPS and the graphene given by

$$\Delta V = \Delta V_{\mathrm{G}} \left[1 - \exp\left(-\Delta t / \tau \right) \right] . \qquad (6.3)$$

The model takes into account the experimental sweep rate $\Delta V_{\mathrm{G}}/\Delta t$, which is calculated by dividing the gate voltage sweep interval ΔV_{G} by the total measurement time interval Δt. Also, the reading and waiting time at each point are taken into account. We use small (10 ms) Δt steps and an experimental sweep rate of 0.1 V/s to model the charge distribution in the graphene layer as a function of time t. The $R(V_{\mathrm{G}})$ curve is calculated as

$$R = 1/Q_{\mathrm{g}}\mu , \qquad (6.4)$$

where μ is the carrier mobility (assumed independent of V_{G}) and Q_{g} is the time-dependent charge. The value of ΔV_{NP} is calculated as a difference between the charge neutrality points of the $R(V_{\mathrm{G}})$ curves for the opposite directions of V_{G}-sweeps and for different sweep intervals. Finally, the dependence of ΔV_{NP} on the range of gate voltage sweep is fitted using τ as the only fitting parameter (as shown in Figure 6.6).

The numerical calculations using the capacitance model reproduce the measured dependence of the amplitude of the hysteresis ΔV_{NP} on the sweep range ΔV_{G} for a value of $\tau = 380$ s, which is the only fitting parameter. This time constant is in line with the characteristic times for switching on/off the resistance in the CG FET.
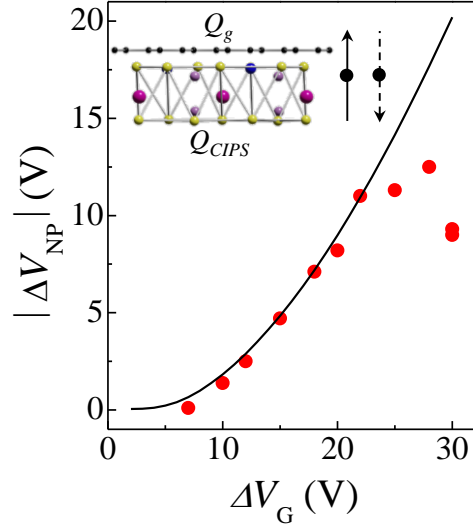
Figure 6.6. Measured (red dots) and calculated (black line) amplitude of the hysteresis (ΔV_{NP}) versus the sweep voltage range ΔV_G. The inset sketch shows the charge transfer at the graphene/CIPS interface.

6.1.5 Temperature dependent memristive effects in CIPS/graphene heterostructure

We examine further this charge transfer by considering the T-dependence of the $R(V_G)$ curves. As shown in Figure 6.7a, at low temperature ($T \leq 200$ K), the hysteresis and memristive effects are very weak. A comparison of the $R(V_G)$ curves for CG and PG at $T < 200$ K reveals that CIPS acts to n-dope the graphene layer. Thus, over this range of temperatures, the charge transfer across the CIPS/graphene interface involves shallow donor-levels in CIPS with a fast temporal trapping/detrapping dynamics. However, as the temperature increases above $T = 200$ K, the hysteresis in CG becomes more pronounced compared to pristine graphene (Figure 6.7a and b) with a thermally activated behaviour described by $|\Delta V_{NP}| \approx \exp(-E_a/\kappa T)$ over the temperature range $T = 200 -$ 320 K, where $E_a = 0.10 \pm 0.01$ eV is the activation energy (Figure 6.7c); a further increase of temperature above $T = 320$ K leads to a significant broadening of the

transfer curves. The increase in the hysteresis with increasing T in CG is accompanied by a corresponding change of the electron density. For the sweep up of V_G, the electron density increases from $n \sim 4 \times 10^{11}$ cm^{-2} to $n \sim 1.3 \times 10^{12}$ cm^{-2} at $V_G = 0$ V (Figure 6.7d).
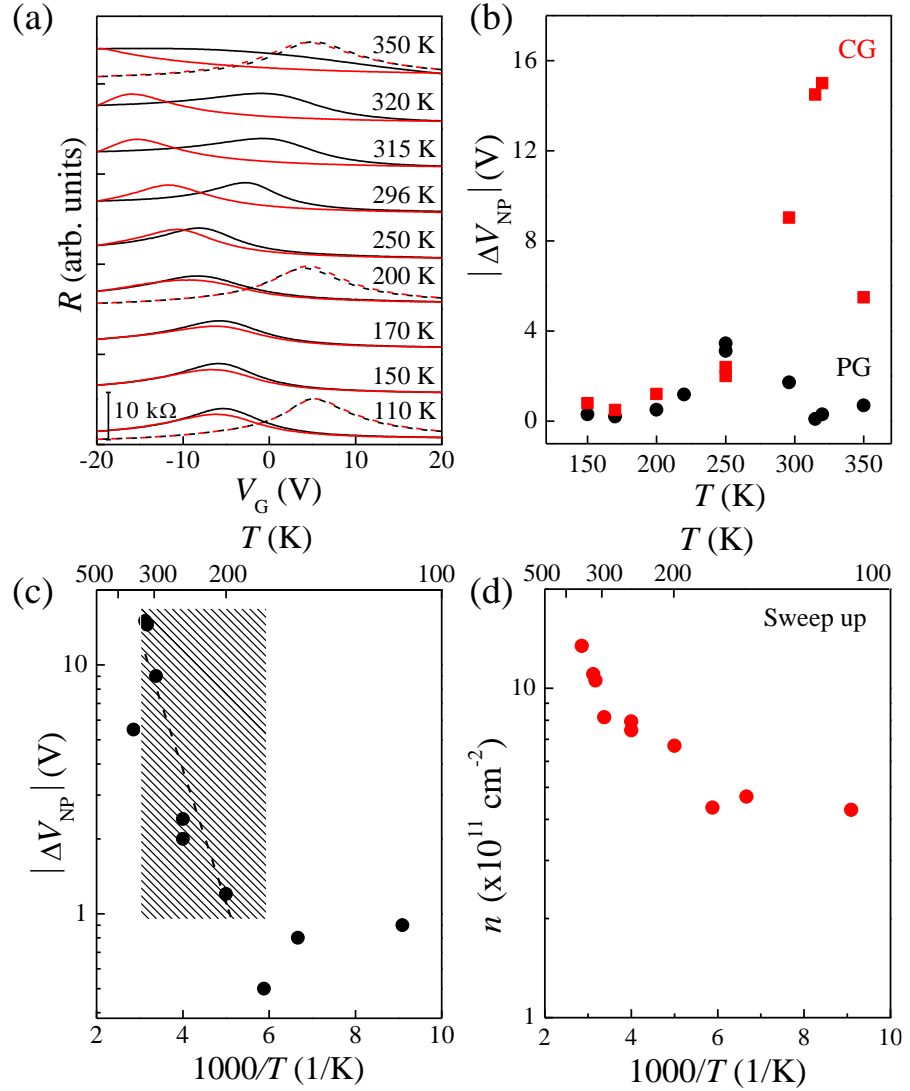
Figure 6.7. (a) Transfer curves $R(V_G)$ for CG at different temperatures T ($I = 1$ μA). The sweep up/down branches are shown in red and black, respectively. For clarity, curves are displaced along the vertical axis. $R(V_G)$ curves for pristine graphene (PG) are shown as dashed lines for $T = 110$ K, 200 K and 350 K. (b) Amplitude of the hysteresis $|\Delta V_{NP}|$ versus T, as derived from the data in part (a) for CG and PG. (c) Amplitude of the hysteresis $|\Delta V_{NP}|$ versus $1/T$, as derived from the data in part (a) for CG. The dashed line is an exponential fit to the data in the temperature range $T = 200$-320 K. (d) Carrier density, n, versus $1/T$ at $V_G = 0$, as derived from the data in part (a) for CG.

The range of high temperatures ($T > 200$ K) in our experiments coincides with that required for the activation of the thermal motion of the Cu-ions, which leads to a progressive increase of disorder and ionic conductivity in CIPS for $T > 250$ K [75] and a paraelectric-ferroelectric transition at $T \sim 315$ K [25, 26]. The temporal dynamics of the resistance and hysteresis at large V_G and $T > 200$K suggest a slow charge transfer at the CIPS/graphene interface mediated by defects with deep localized states in the band gap of CIPS. Although model calculations predict an intrinsic, stable out-of-plane ferroelectricity in CIPS, charge transfer from/to defects across the CIPS/graphene interface can play a dominant role at $T > 200$ K. Since the range of temperatures at which the hysteresis occurs corresponds to the temperatures at which the Cu-ions are displaced from their lattice sites, we propose that the defects responsible for the hysteresis may form as a result of the thermally activated migration of the Cu-ions. Thus, the two phenomena, the thermal motion of the Cu-ions, which leads to a progressive increase of disorder, and the trap states due to the crystal disorder, could be linked.

6.1.6 Photodoping effects in CIPS/graphene heterostructure

We exploit the semiconducting properties of CIPS and use light to probe further the charge transfer and hysteresis effects in the FETs. Figures 6.8a and b show the $R(V_G)$ curves of CG at $T = 100$ K and 300 K under light illumination with laser light of wavelength $\lambda = 405$ nm and incident power P_i over a wide range from $P_i = 0$ (dark) to $P_i \sim 2 \times 10^{-8}$ W. At $T = 100$ K (Figure 6.8a) and low laser powers ($P_i < P_1 = 2 \times 10^{-13}$ W), the $R(V_G)$ curves are not changed by light. In contrast, for $P_i > P_1$, the $R(V_G)$ curves shift to negative gate voltages and the

hysteresis becomes more pronounced. A distinct phenomenology is observed instead at room temperature. As shown in Figure 6.8b, at $T = 300$ K, increasing P_i above $P_2 = 1 \times 10^{-10}$ W leads to an upward shift of the $R(V_G)$ curves, rather than the downward shift seen at $T = 100$ K. Thus, the photodoping effect in graphene changes from n-type (Figure 6.8a) to p-type (Figure 6.8b) with increasing temperature. At all temperatures, light enhances the hysteresis in $R(V_G)$: The P_i-dependence of $|\Delta V_{NP}|$ at different T is illustrated in Figure 6.8c.
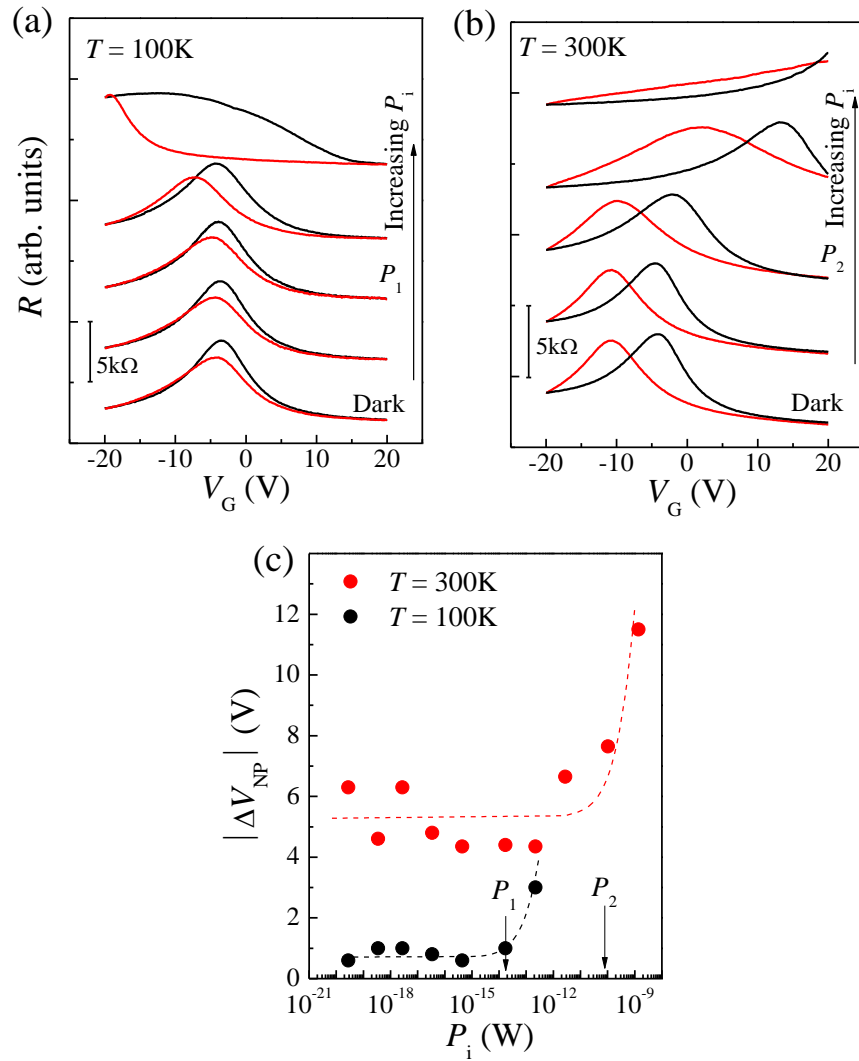
Figure 6.8. Transfer curves $R(V_G)$ for CG for different laser powers P_i ($\lambda = 405$ nm) at (a) $T = 100$ K and (b) 300 K ($I = 1$ µA). Changes in $R(V_G)$ are observed for $P_i > P_1 \sim 2 \times 10^{-13}$ W ($T = 100$ K) and $P_i > P_2 \sim 1 \times 10^{-10}$ W ($T = 300$ K). The sweep up/down branches are shown in red and black, respectively. For clarity, curves are displaced along the vertical axis. (c) Amplitude of the hysteresis $|\Delta V_{NP}|$ extracted from the transfer curves versus P_i from parts (a-b).

The light-induced hysteresis and photodoping of graphene are activated above a critical laser power that depends on temperature. We propose that at low temperatures, donor-like states in CIPS and/or at the CIPS/graphene interface are ionized by light, acting effectively as a local positive gate for the graphene channel. The photo-ionization of defects increases the electron density in the graphene layer and reduce the carrier mobility due to enhanced carrier scattering by ionized impurities (Figure 6.9). In contrast, at room temperature, photo-created holes are accelerated towards graphene by the electrostatic potential of the CIPS/graphene interface. This potential arises from the ionization of defects in CIPS leading to an increasing charge transfer at the CIPS/graphene as the temperature increases. We note that the light-induced effects tend to be weaker at gate voltages far from the neutrality point of graphene as the change in carrier density due to the gate becomes stronger than the light-induced change. The hysteresis and slow dynamics of the resistance change under light illumination (Figure 6.10) are indicative of a light-activated slow redistribution of charges. This is a reversible process, suggesting a dynamical disorder tuneable by light.
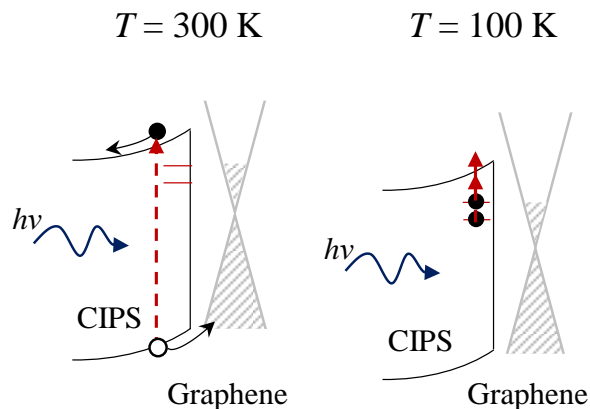
Figure 6.9. Schematic of the separation of photocreated carriers by the electric field in CG (left) and the ionization of traps by light (right).

The time-dependence of R was measured under light ($\lambda = 405$ nm, $P \sim$ 1.0×10^{-10} W, $T = 300$ K) at different gate voltages V_G. The resistance was measured by monitoring the voltage drop at a constant current, $I = 1$ μA, in a time interval following the turn off ($t = 0$ s) or turn on ($t = 0$ s) of the light (Figure 6.10). As shown in Figure 6.10a, for $V_G = 0$ V, when light is turned on at $t = 0$ s, the resistance initially decrease before increasing and reaching a steady state that changes slowly with time. If light is turned off instead, the resistance initially increases before decreasing and reaching a steady state. A similar dynamics was observed at $V_G = + 20$ V (Figure 6.10b) and $V_G = - 20$ V (Figure 6.10c). In all cases, the temporal response is slow (> 10 s) with distinct dynamics in the initial (~ 10 s) and follow up ($> 10^2$ s) time intervals. These effects are reversible if the device is rested in the dark for a sufficiently long time (~ 1 day).
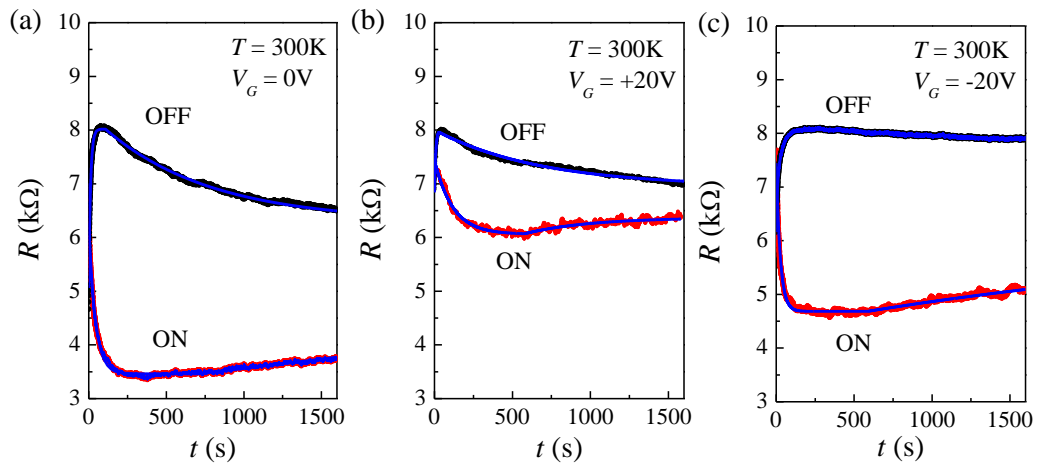
Figure 6.10. Time-dependence of the resistance R at different gate voltages: (a) $V_G = 0$ V, (b) $V_G = + 20$ V, and (c) $V_G = - 20$ V. The resistance was measured by monitoring the voltage drop at a constant current, $I = 1$ μA, in a time interval following the turn off or turn on of the light. These experiments were conducted with laser power $P = 1.0×10^{-10}$ W ($\lambda = 405$ nm, $T = 300$ K). Blue lines are fit to the data by exponential curves from which we derive the rise and decay times of the resistance. In general, the dynamics following the switch off/on of the light is significantly faster (~ 10 s) than that at long times.

6.2 Ferroelectric tunnel junctions (FTJs) based on CIPS/graphene heterostructures

A ferroelectric tunnel junction (FTJ) is a two terminal vertical heterostructure with metal electrodes separated by a thin layer of a ferroelectric material. The transport properties of such devices change dramatically when the film thickness approaches the nanometer scale, causing direct tunneling to be the dominant mechanism [122]. Thin layers of CIPS has been incorporated into FTJs to study tunneling electroresistance by switching the ferroelectric polarisation [21, 35]. These devices have demonstrated large modulation of tunnel barrier height of about ~1 eV in the junction induced by the polarisation field in the adjacent CIPS [35]. This part of the chapter reports on a tunnel junction based on CIPS where a CIPS flake of thickness $t = 34$ nm is embedded between two electrodes made of few layer graphene (FLG).

Figure 6.11 shows the optical image and schematics of the tunnel junction whose *I-V* characteristics was acquired over a range of *V* and *T*. By analysing the direction of the hysteresis loop in the *I-V* characteristics, we study the mechanism of charge transfer across the FLG/CIPS/FLG interface.
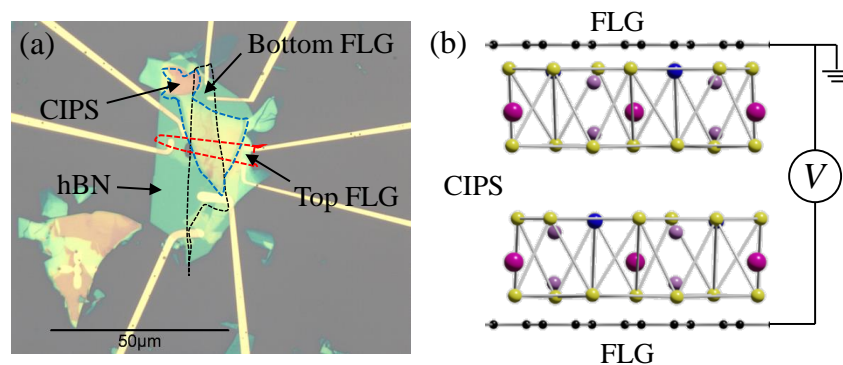
Figure 6.11. (a) Optical image of the device with the boundary of each flake traced by dashed lines. (b) Schematic of the FLG/CIPS/FLG junction. The bottom and top FLG comprise 7 and 3 graphene layers, respectively. The CIPS layer has thickness $t = 34$ nm. A voltage *V* is applied between the two FLG electrodes, generating a current *I*.

Figure 6.12a-d shows the *I-V* characteristics at different temperatures. The current at each temperature was recorded by sweeping *V* in consecutive trips from 0 V to +*V*, sweeping back to –*V*, and returning to 0 V. The applied voltage and temperature are critical to the hysteretic behaviour in the *I-V*. As *T* increases above *T* = 250 K, we observe a larger *I* and a counter-clockwise hysteresis loop in *I-V*. The amplitude of the current is larger when sweeping the voltage from high to low positive *V* (or from more negative to less negative *V*).
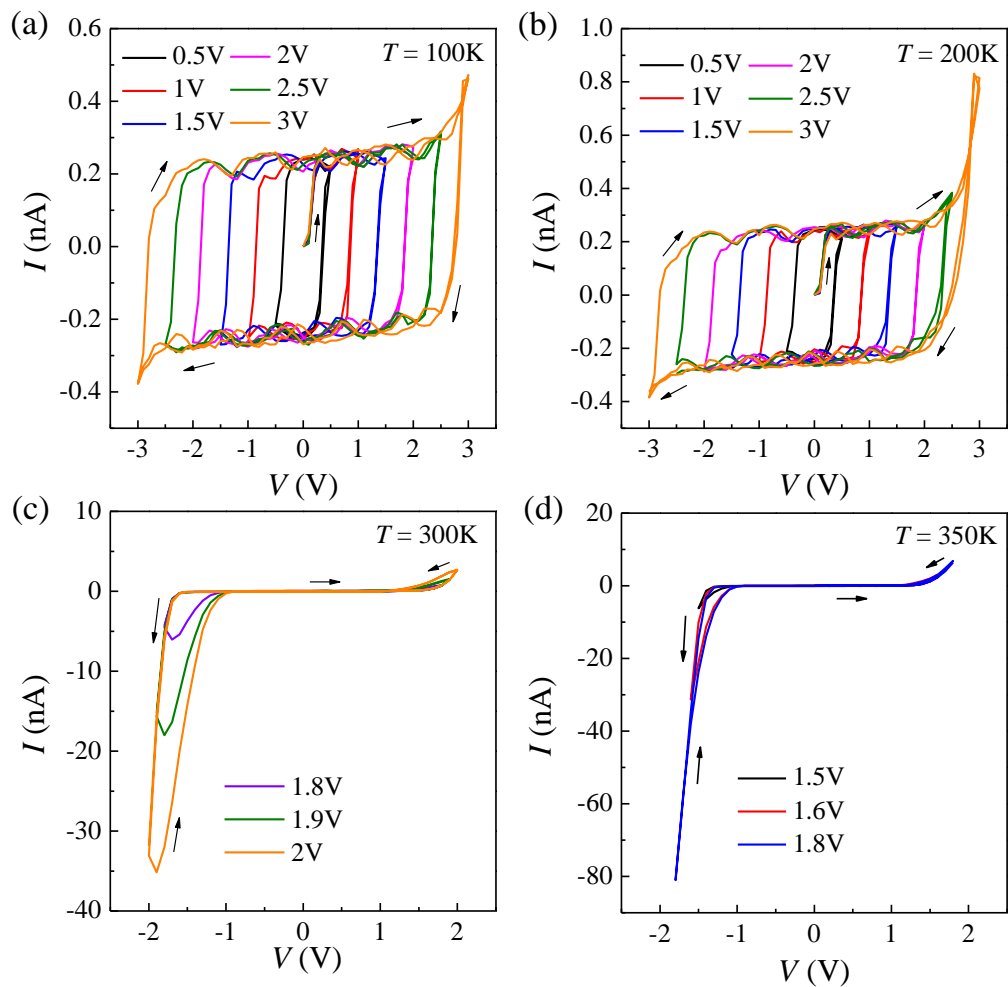
Figure 6.12. *I-V*s measured at (a) *T* = 100 K, (b) *T* = 200 K, (c) *T* = 300 K and (d) *T* = 350 K. The top FLG is grounded and a positive/negative voltage is applied to the bottom FLG electrode. The arrows indicate the direction of the hysteresis loop in each plot.

From the Arrhenius plot of the amplitude of the current versus $1/T$ at $V =$ 2V, we extract an activation energy $E_a = 0.3$-0.5 eV for $T > 200$ K (Figure 6.13a). We estimate a break down electric field of $E_B = V/t = 52$ MV/m at $T = 300$ K and $V = 1.8$ V for $t = 34$ nm thick CIPS layer. This shows that CIPS has smaller break down field than that of other commonly used dielectrics, such as nanometer-thick SiO_2 ($\sim 10^9$ V/m) and hBN ($\sim 10^9$ V/m) [123, 124]. The applied electric fields in this study (up to about 5×10^7 V/m) are higher or comparable to the reported coercive field of $\sim 5\times10^6$ V/m (in bulk materials, [76]), $\sim 14\times10^7$ V/m (in devices, [35]), and 1×10^7 V/m to 13×10^7 V/m (in PFM, [7]). Figure 6.13b shows that as the temperature increases, the breakdown field decreases.
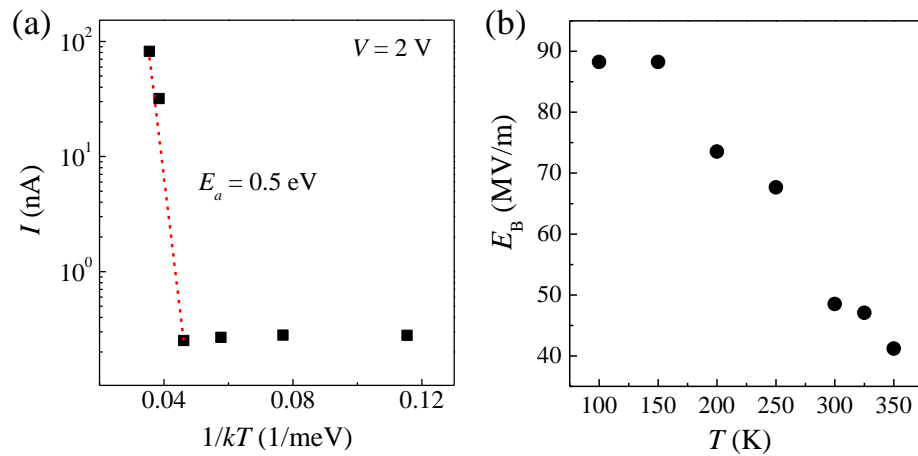
Figure 6.13. (a) Arrhenius plot of I versus $1/k_BT$ at $V = 2$ V, as derived from the *I-V*s at different temperatures. (b) Plot showing the breakdown field (E_B) of CIPS extracted from the *I-V*s as a function of temperature.

The *I-V*s are asymmetric with respect to the polarity of V, suggesting two nonequivalent interfaces. The increasing hysteresis with increasing the sweep range of V suggest that polarized charges at the CIPS/FLG interface can effectively lower or increase the potential barrier seen by electrons (Figure 6.14) [21], causing a change of the electron transmission through the junction and resistance switching.
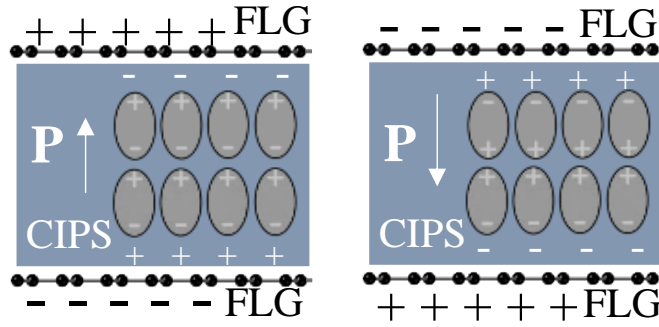
Figure 6.14. Schematic of surface polar charges and FE polarisation in FLG/CIPS/FLG.

In general, we cannot exclude a contribution of charge transfer in the TJ. The overall shape of the transport characteristics and hysteresis is influenced by both charge transfer and ferroelectric polarisation effects. These two phenomena induce a different hysteresis, *i.e.* clockwise or counter-clockwise hysteresis, respectively. The hysteresis behaviour tends to weaken with increasing T from 300 K to 350 K, suggesting that the ferroelectric switching is weakened by a thermally activated charge transfer from the defects and/or ionic conductivity in CIPS.

6.3   Summary

In conclusion, we have shown that bringing CIPS into contact with a graphene layer triggers a range of complex phenomena. We have reported a large hysteresis effect in field effect transistors where the graphene layer acts as a channel and CIPS behaves as a charge trapping layer. The underlying mechanisms of conduction were examined over a range of temperatures and under light illumination to account for different resistive switching mechanisms. The measured effects indicate a slow (>100 s) charge transfer between CIPS and graphene at temperatures $T > 200$ K. Charge transfer can occur in darkness and

under light illumination. In particular, light induces a temperature dependent photodoping effect in graphene that varies from *n*- to *p*-type with increasing temperature. The measured electrically and optically controlled memristive effects in these devices highlight the complexity of the graphene/CIPS heterostructure. Charge transfer mediated by defects in CIPS can influence the tunneling resistance of FTJs and the operation of other ferroelectric devices, such as FeFETs. The addition of an hBN barrier layer could prevent the charge transfer at the CIPS/graphene layer, facilitating the observation of the ferroelectric switching, as done in recent work with other 2D ferroelectrics [109]. Thus, engineering the interface of graphene with ferroelectrics should consider the contribution of both charge transfer and polarisation effects for device optimization and a rich variety of new applications.

Chapter 7

Room temperature quantum Hall effect in gated CIPS-graphene heterostructure

This chapter reports on hybrid field-effect transistors based on CIPS/graphene interface in which a single layer of graphene is capped with a CIPS layer. Electrostatic gating of the graphene channel enables the Fermi energy to be tuned so that electrons in the localized states of the insulator are in equilibrium with the current-carrying, delocalized states of graphene. Due to the presence of strongly bound states in this hybrid system, a quantum Hall plateau state can be achieved at room temperature in relatively modest magnetic fields. This phenomenon offers the prospect for the controlled manipulation of the quantum Hall effect at room temperature.

The ten-terminal pristine graphene Hall bar devices studied in this chapter were produced by Dr. Camilla Coletti's group at the Institute Italiano di Tecnologia, Italy. The fabrication of CIPS/graphene heterostructures and the electrical measurements were conducted by myself at the University of Nottingham. The surface studies and analysis related to AFM, PFM and KPFM were conducted by Dr. James Kerfoot at Park Systems in Nottingham. Hall measurements at high magnetic fields ($B > 16$ T) were performed by Dr. Nathan Cottam at the HFML-EMFL facility in Nijmegen, Netherlands, assisted by Dr. Steffen Wiedmann's group.

The results presented in this chapter have been accepted in *Communications Physics*.

7.1 Introduction

The electronic properties of graphene are very sensitive to applied magnetic fields ($\mathbf{B}$) and are ideally suited for the investigation of the quantum Hall effect (QHE). This is exemplified by plateaus in the Hall resistance due to the quantization of the two-dimensional electron motion into Landau levels (LL) [43, 125-132]. The QHE, first discovered in Si metal–oxide–semiconductor field-effect transistors [133], exhibits important differences in graphene due to the electron–hole degeneracy near the charge neutrality point, which leads to a distinctive half-integer QHE and a non-zero Berry's phase of the electron wavefunction [127, 128, 130-132].

Of particular significance for the QHE in graphene is the effect of dopant impurities near its surface. Screening effects in graphene [134, 135] tend to be weakened by a magnetic field and can facilitate the localisation of charge carriers in the disordered potential of the graphene layer [136, 137]. For example, for epitaxial graphene on a Si-terminated SiC substrate [138-141], donors reside in the SiC layer just below the graphene layer. These dopants act as a reservoir of electrons for graphene, keeping the Hall voltage on the $v = 2$ QH plateau over a wide range of magnetic fields [142]. An extended quantum Hall plateau was also observed in graphene-based field effect transistors (FETs) in which graphene is capped by a thin layer of the van der Waals crystal InSe [143, 144]. These examples of "giant" QH plateaux in graphene have been reported at low temperatures ($T < 200$ K) and have been assigned to the magnetic field and electric field induced transfer of charge carriers between the degenerate Landau levels of graphene and the localized states in its proximity. A full microscopic model for the QHE in these hybrid systems does not yet exist. However, recent

work has modelled the interaction between localized charges near the surface of graphene [145], showing that when the chemical potential is in the gap between Landau levels, charges can form stable bound states over a distance of the order of the magnetic length $l_B = \sqrt{\hbar/(eB)}$ and binding energy $E_B = (\hbar v_F/l_B)$, where $v_F \approx 10^6$ m/s is the Fermi velocity and e is the elementary charge. This phenomenon can persist well beyond cryogenic temperatures, opening possibilities for the controlled manipulation of the QHE at room temperature. To date, a room temperature resistance quantum has been reported only in high mobility graphene at large magnetic fields that are only available in a few high field magnet laboratories [128, 146].

Here, we report on the QHE in field effect transistors based on a single layer graphene capped with the ferroelectric van der Waals crystal CuInP$_2$S$_6$ (CIPS). The CIPS layer is used as a source of localized charge carriers in proximity to graphene. We report a hysteretic behaviour in the longitudinal and transverse magnetoresistance of graphene over a wide range of applied magnetic fields and temperatures. Similar hysteretic phenomena in graphene have been reported previously in zero magnetic field and assigned to charge trapping [119, 120, 147-150] and/or ferroelectric polarisation [13, 117, 151-153]. In this work, we report on the dynamic exchange of charge carriers at the CIPS/graphene interface and its influence on the QHE and its hysteretic behaviour. The QHE is found to be weakly dependent on temperature and is observed at room temperature over a range of widely accessible applied magnetic fields.

7.2 Transport characteristics in zero magnetic field

The CIPS/graphene heterostructure was prepared by exfoliation and visco-elastic stamping of a CIPS flake on a graphene Hall bar based on high-quality graphene grown by CVD (chemical vapour deposition). Figure 7.1a shows the optical image of a ten-terminal Hall bar based on graphene (G) and CIPS/graphene (CG) on a 285 nm-thick SiO_2/n-Si substrate. The morphology of the layers was probed by atomic force microscopy (AFM) and single pass amplitude-modulated Kelvin probe force microscopy (AM-KPFM) [95]. The CIPS layer has a non-uniform layer thickness ranging from 20 nm to 50 nm and a uniform work function potential at the graphene/CIPS interface (Figure 7.1b). Details of the fabrication and the characterisation of the CIPS flakes by AFM and piezoresponse force microscopy have been mentioned in the Chapter 3 and Chapter 4 (section 4.2.1 and 4.2.2), respectively.
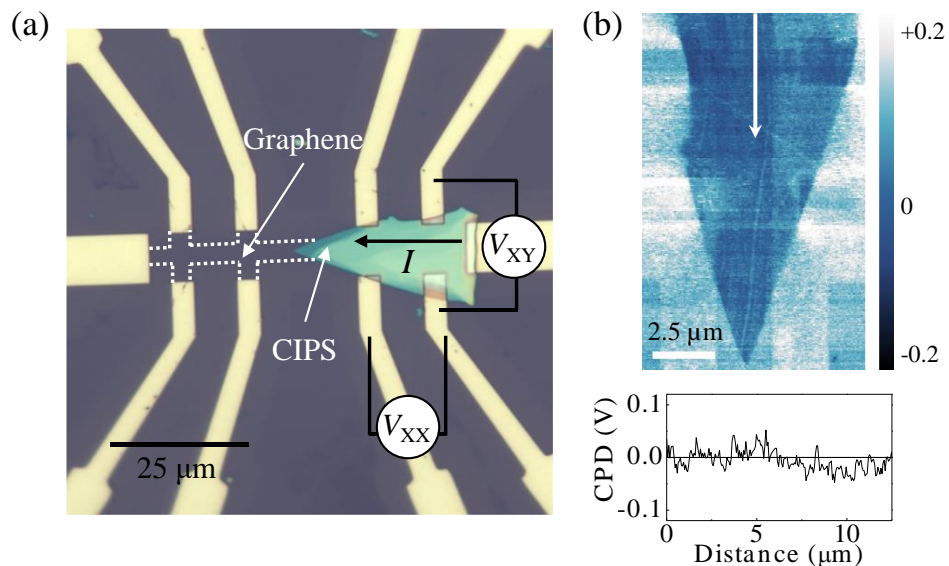
Figure 7.1. (a) Optical image of a Hall bar based on CIPS/graphene (CG) on a SiO_2/n-Si substrate and Ni-Au contacts. One section of the graphene layer is covered by a CIPS layer. The white dotted lines mark the edges of pristine graphene. (b) AM-KPFM contact potential difference (CPD) map (top) and CPD profile (bottom) of CG measured with a Multi75E cantilever at a voltage amplitude of $V_{AC} = 4$ V and frequency $f_{AC} = 17$ kHz. The CPD-profile is obtained along the length of the CIPS-flake, as indicated by the white arrow in the map.

The longitudinal resistance R_{XX} was measured at a constant current ($I =$ 1 μA). The voltage drop V_{XX} across different pairs of terminals along the graphene channel was measured over a range of gate voltages V_G applied between the graphene and Si-gate electrodes. As can be seen in the inset of Figure 7.2, for pristine graphene the $R_{XX}(V_G)$ curve at $T = 300$ K is peaked at the neutrality point $V_{NP} = + 10$ V. Using a capacitance model of the graphene FET, we estimate a hole density $p = 7\times10^{11}$ cm^{-2} at $V_G = 0$ and a hole (electron) mobility $\mu = 9\times10^3$ cm^2/Vs (10^4 cm^2/Vs) for carrier concentrations in the range 10^{11}-10^{12} cm^{-2} at $T = 300$ K. In contrast to pristine graphene, for CG the transfer characteristics show a pronounced hysteresis and are asymmetric (Figure 7.2): The amplitude of the hysteresis increases with increasing the sweep range of V_G from $\Delta V_G = \pm 10$ V to ± 50 V. For $\Delta V_G = \pm 10$ V, the $R_{XX}(V_G)$ curves are shifted to lower values of V_G compared to pristine graphene; also, the field effect and Hall mobility for holes (electrons) is reduced to $\mu \sim 10^4$ cm^2/Vs to $\mu \sim 2\times10^3$ cm^2/Vs.
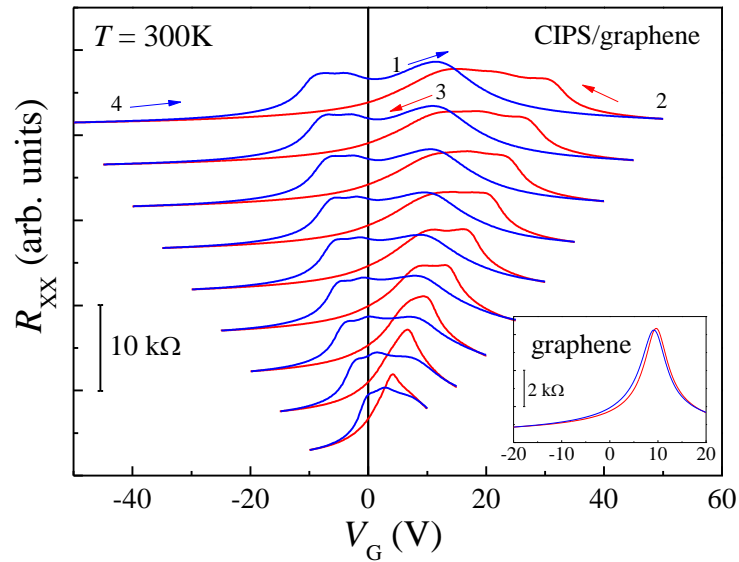
Figure 7.2. $R_{XX}(V_G)$ curves for CG at $T = 300$ K ($I = 1$ μA, $B = 0$ T). The sweep up/down branches are shown in blue and red, respectively. Curves are displaced along the vertical axis for clarity. Inset: $R_{XX}(V_G)$ curve for a reference sample based on pristine graphene (G) at $T = 300$ K ($I = 1$ μA, $B = 0$ T).

In general, the $R_{XX}(V_G)$ curve consists of multiple peaks, suggestive of a channel with a non-uniform distribution of dopants; also, the temporal response of R_{XX} is slow (with rise and decay times $\tau > 100$ s). Thus, the $R_{XX}(V_G)$ curve depends on the sweep range of V_G and sweep rate $\Delta V_G/\Delta t$. A value of $\Delta V_G/\Delta t =$ 0.3V/s was used for the data presented in the remaining part of this work.

Hysteresis in the transport characteristics of graphene can arise from a gate-induced polarisation at the interface of graphene with a ferroelectric layer [152]. For our CG, the hysteresis is not dominated by this phenomenon as a gate-induced ferroelectricity would produce a shift of the neutrality point V_{NP} in the direction of the gate sweep, *i.e.* V_{NP} would shift to higher voltages when V_G is swept from negative to positive values compared to when V_G is swept from positive to negative values. On the other hand, a hysteresis can also originate from a slow charge transfer at the CIPS/graphene interface, as reported earlier in a similar device structure [147]. The gate voltage induces charges in the graphene layer, which then redistribute between the graphene and CIPS layers. In the first part of the sweep of V_G to positive gate voltages ($V_G > 0$ V), electrons are transferred from graphene onto CIPS; during reverse sweep with $V_G < 0$ V, the CIPS layer discharges its electrons onto graphene. A non-uniform distribution of localized states in CIPS can create areas of graphene with different carrier densities, thus causing the multiple peaks in $R_{XX}(V_G)$ shown in Figure 7.2.

We model the hysteresis in $R_{XX}(V_G)$ by using a classical capacitance model for the FET, considering a charge transfer at the CIPS/graphene interface as described previously in Chapter 6 (section 6.1.4). Figure 7.3a shows the different

charge neutrality points for sweep up and down branches, as estimated from the multiple peaks occurring in the $R_{XX}(V_G)$ for a V_G sweep range of ± 50 V.
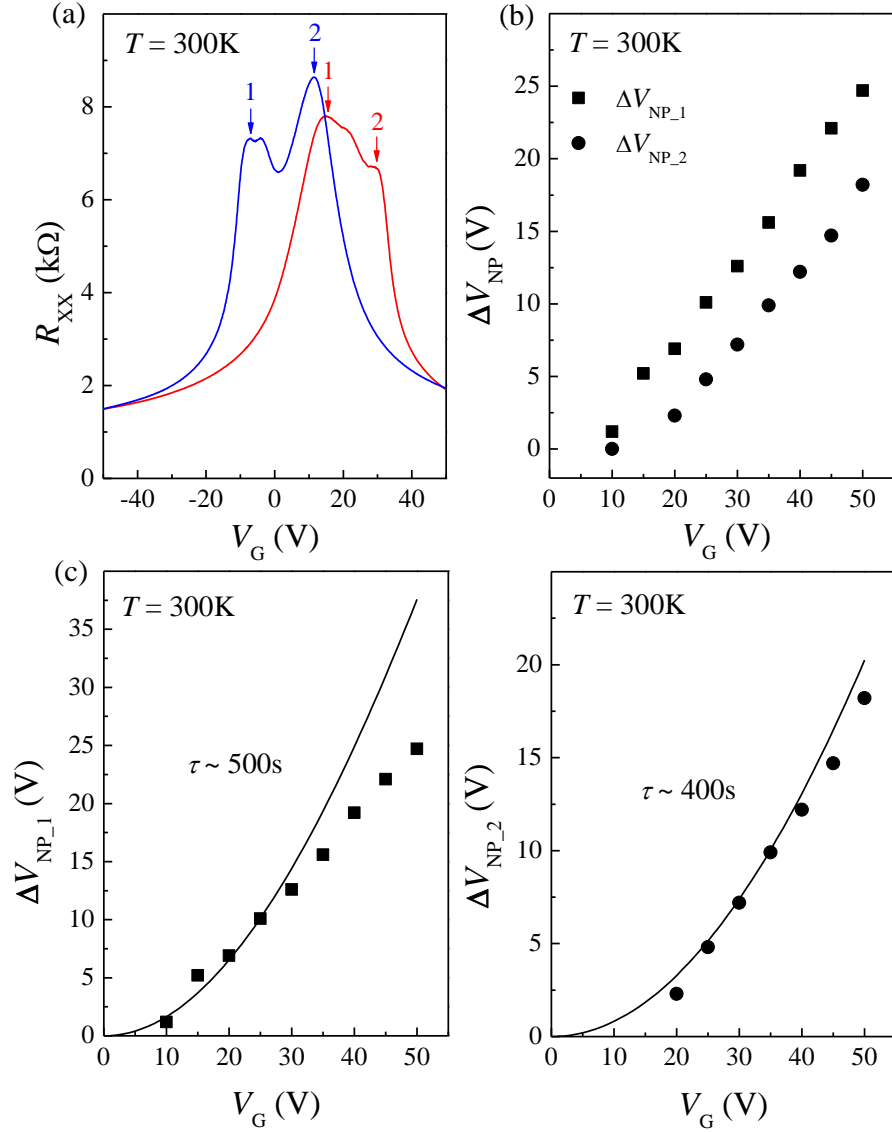
Figure 7.3. (a) $R_{XX}(V_G)$ dependence for CG under gate voltage sweeps of ΔV_G = ± 50 V at $T = 300$ K, showing multiple charge neutrality points (indicated by 1 and 2). The sweep up/down branches are shown in blue and red, respectively. (b) Amplitude of hysteresis (ΔV_{NP}) versus sweep voltage range of ΔV_G for charge neutrality points 1 (black squares) and 2 (black dots) extracted from Figure 7.2. (c) Calculated (black line) amplitude of hysteresis (ΔV_{NP}) versus sweep voltage range of ΔV_G for different charge neutrality points shown in part (b) using the capacitance model. The sweep rate is 0.3V/s.

The amplitude of hysteresis (ΔV_{NP}) is measured as the difference between the charge neutrality points for opposite direction of V_G-sweeps and for different gate voltages ranges (Figure 7.3b). We use an experimental sweep rate of 0.3 V/s to model the charge distribution using τ as the only fitting parameter. We estimate that a charge ΔQ redistributes slowly between the graphene (Q_g) and CIPS (Q_{CIPS}) layers with a characteristic time constant $\tau > 100$ s at room temperature (Figure 7.3c). The regions of CG tend to charge/discharge with similar slow temporal dynamics; also, the value of $\Delta Q/e = n_Q$ is dependent on V_G and reaches values of up to $n_Q \sim 10^{12}$ cm^{-2} at large V_G ($V_G = + 50$ V).

The hysteresis in $R_{XX}(V_G)$ is also affected by light illumination as shown in Figure 7.4. Figure 7.4a compares the transfer characteristics of CG in darkness and when the sample is excited with an unfocussed laser beam of photon energy larger ($hv = 3.06$ eV) and smaller ($hv = 1.96$ eV) than band gap of CIPS ($E_g = 2.7$ eV at $T = 300$ K). It is found that for $hv = 1.96$ eV ($\lambda = 632.8$ nm), the hysteresis in $R_{XX}(V_G)$ is the same as observed in the dark. In contrast, a photon energy of $hv = 3.06$ eV ($\lambda = 405$ nm) leads to a reduced hysteresis and a shift of the $R_{XX}(V_G)$ curve to larger positive V_G. In particular, for an increasing optical power P and $hv = 3.06$ eV, the shift of the $R_{XX}(V_G)$ curve increases, the hysteresis tends to weaken and the $R_{XX}(V_G)$ curve evolves from a multi-peaked curve into a single peak (Figure 7.4b). This indicates an effective photo-induced p-type doping of graphene. Also, the photo generated carriers in the CIPS layer tend to screen the disordered potential created by localized charges, thus weakening the hysteretic behaviour and restoring the transfer characteristics of graphene.
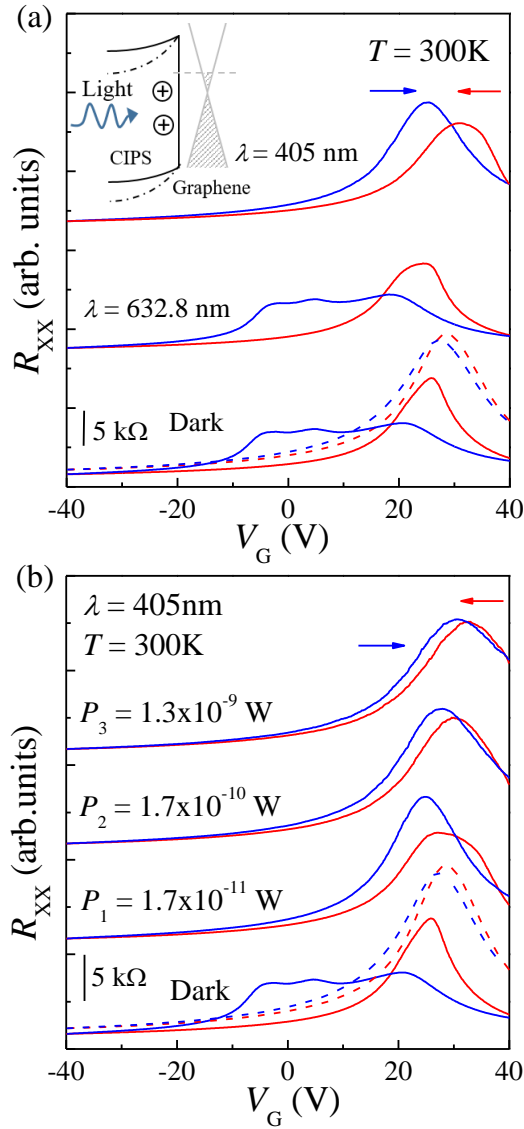
Figure 7.4. (a) $R_{XX}(V_G)$ curves for CG (solid lines) for different laser excitation wavelengths, $\lambda = 632.8$ nm ($h\nu = 1.96$ eV) and $\lambda = 405$ nm ($h\nu = 3.06$ eV) at $T = 300$ K ($I = 1$ µA, $P = 1.7310^{-11}$ W). Inset: Schematics of the screening of the built-in electric field at the CIPS/graphene interface by carriers photocreated in CIPS. (b) $R_{XX}(V_G)$ curves for CG (solid lines) for different laser powers $P_1 = 1.7 \times 10^{-11}$ W, $P_2 = 1.7 \times 10^{-10}$ W and $P_3 = 1.3 \times 10^{-9}$ W ($\lambda = 405$nm). In both panels, $R_{XX}(V_G)$ curves for graphene under dark conditions are shown as dashed lines. The sweep up/down branches are shown in blue and red, respectively. For clarity, curves are displaced along the vertical axis.

In summary, the transport characteristics of graphene are very sensitive to charges trapped in the CIPS layer. This effect is observed in all our CG devices and is used to probe the effect of localized charges on the QHE at different temperatures, magnetic fields and gate voltages.

7.3   Magneto-transport and quantum Hall effect

Figure 7.5a and 7.5b show the temperature dependence of the $R_{XX}(V_G)$ curves for CG at $B = 0$ T and 16 T, respectively. At low temperatures ($T \leq 200$ K), the hysteresis in $R_{XX}(V_G)$ is weak, as also observed in pristine graphene. However, it becomes pronounced for $T > 200$ K. In particular, in magnetic field ($B = 16$ T in Figure 7.5b), the $R_{XX}(V_G)$ curves exhibit pronounced maxima and minima.
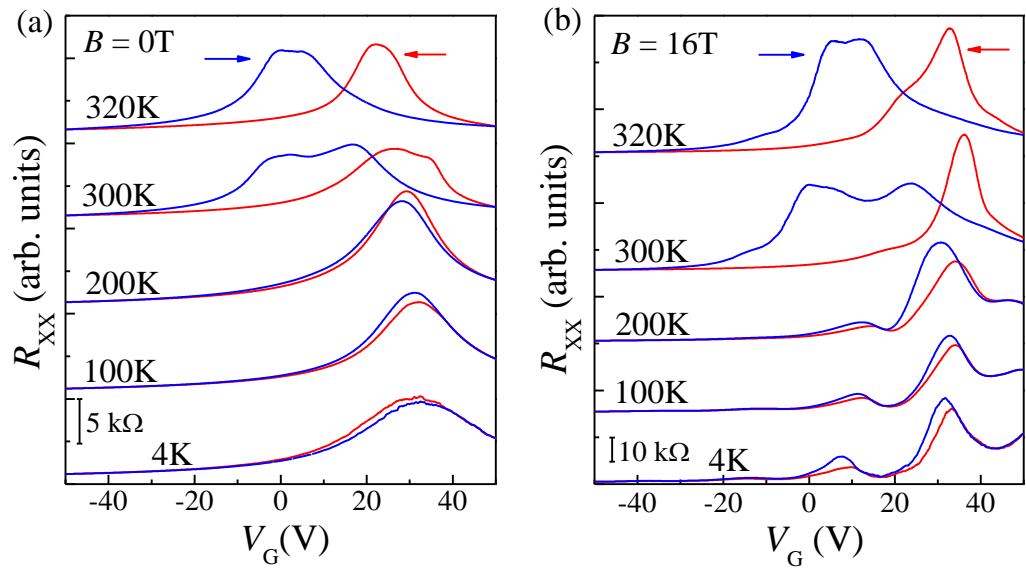
Figure 7.5. (a-b) $R_{XX}(V_G)$ curves for CIPS/graphene at different temperatures T ($I = 1$ μA) and (a) $B = 0$ T and (b) $B = 16$ T. The sweep up/down branches are shown in blue and red, respectively. For clarity, curves are displaced along the vertical axis

To illustrate this behaviour more clearly, we plot in Figure 7.6a-b-c the colour plots of R_{XX} versus V_G and B at different T and for different (up/down) sweeps of V_G. For T up to 200 K (Figure 7.6a-b), the bright red region in $R_{XX}(B, V_G)$ centred at $V_{NP} \sim +30$ V corresponds to the neutrality point of graphene represented by the zeroth Landau level, LL ($n = 0$). For both sweep up/down branches, secondary peaks in $R_{XX}(B, V_G)$ emerge for $B > 5$ T at around $V_G = 20$

V and 40 V. As V_G increases from negative to positive values, first holes ($V_G < V_{NP}$) and then electrons ($V_G > V_{NP}$) fill successive LLs.
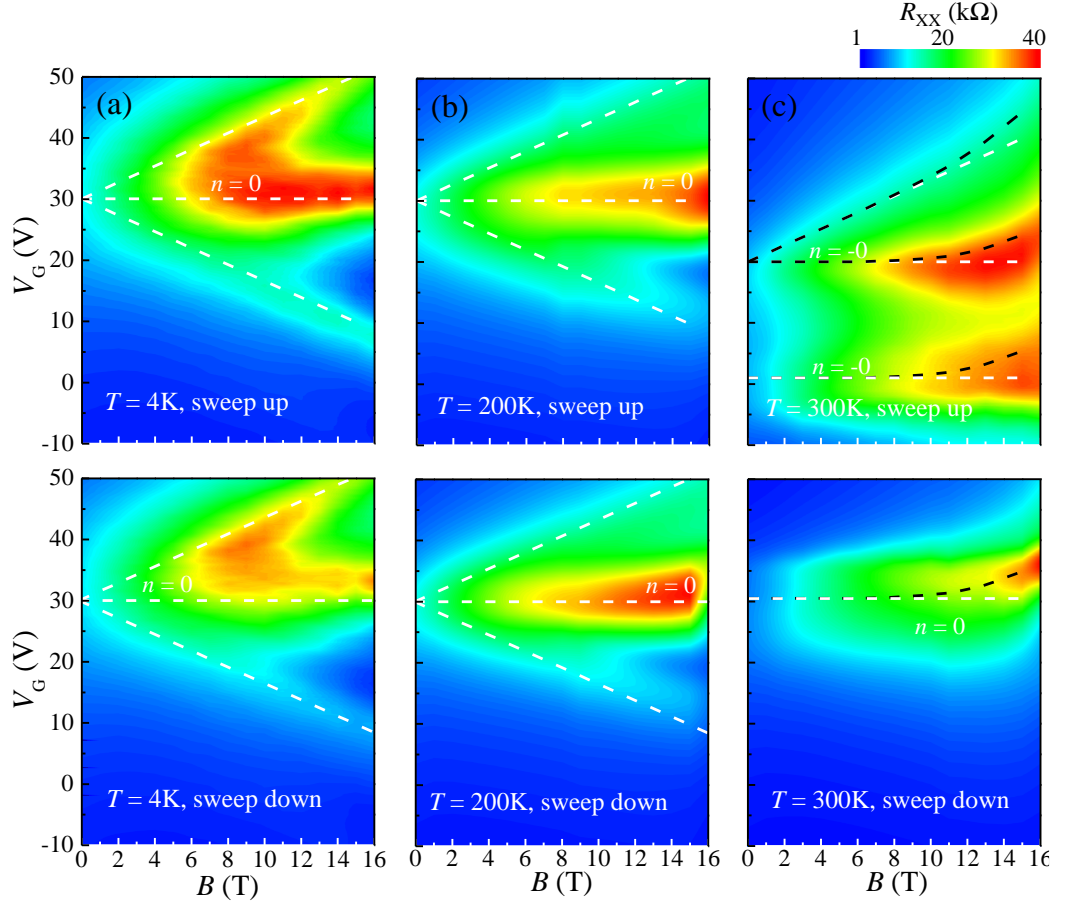
Figure 7.6. Colour plots of R_{XX} versus B and V_G at (c) $T = 4$ K, (d) $T = 200$ K and (e) $T = 300$ K and different sweeps (top: sweep up; bottom: sweep down; $I = 1$ μA). Dashed white lines represent the calculated Landau level (LL) charts using a conventional model, as described in the text. Dashed black lines in part (e) show the calculated LL charts assuming a B-induced charge transfer.

The energy-level spectrum of Dirac fermions in a magnetic field is described by the relation $E_n = sgn(i)\sqrt{ehv_F^2 B|n|/\pi}$, where $n = 0, \pm1$… The spectrum comprises electron ($n \geq 1$) and hole ($n \leq -1$) LLs, as well as a LL ($n = 0$) at the neutrality point. We use the capacitance equation $C = e[dn_g/dV_G]$ to calculate the voltage separation ΔV_G of the maxima in the $R_{XX}(V_G)$ curve at different B. Here $C = \varepsilon\varepsilon_0/t$ is the "classical" capacitance per unit area of the

graphene/SiO$_2$/Si heterostructure, $t = 285$ nm is the SiO$_2$ layer thickness, $\varepsilon = 3.9$ is the relative dielectric constant of SiO$_2$, ε_0 is the permittivity of free space, and n_g is the carrier density in the graphene layer. We express the separation between the maxima in $R_{XX}(V_G)$ corresponding to the alignment of the Fermi level with the $n = 0$ and $n = \pm 1$ LLs as $\Delta V_G = eg/C$, where $g = 4eB/h$ is the LL degeneracy. This model reproduces accurately the data at low T for both sweep up and down of V_G ($T = 4$ K and 200 K in Figure 7.6a-b, white dashed lines), but fails to describe the data at high T ($T = 300$ K in Figure 7.6c, white dashed lines). At $T = 300$ K, the LL quantization is obscured by a large hysteresis; in particular, the neutrality points V_{NP} tend to shift to larger positive V_G with increasing B. The black lines in Figure 7.6c describe the deviation of the LL features in $R_{XX}(B, V_G)$ from a conventional LL chart model. The measured deviation is reproduced by considering a B-dependent charge transfer and the capacitance equation $C = e[dn_g/dV_G]$. We find that the magnetic field tends to reduce the density of electrons transferred from CIPS to graphene from $\Delta n_g = 4 \times 10^{10}$ cm^{-2} at $B = 10$ T to $\Delta n_g = 4 \times 10^{11}$ cm^{-2} at $B = 16$ T. We explore further this phenomenum by examining the dependence of the Hall resistance (R_{XY}) on B, V_G and T.

Figure 7.7 and 7.8 shows the V_G-dependence of R_{XY} over a range of temperatures ($T = 4$ - 320 K) and magnetic fields from $B = 0$ T to 16 T. At $T = 4$ K (Figure 7.7a inset), the $R_{XY}(V_G)$ curve shows quantum Hall plateaus centred at $V_G \sim + 20$ V and $V_G \sim + 40$ V, corresponding to the LL filling factor $v = 2$ for holes and electrons, respectively. The LL filling factor v is derived from the relation $v = \pm 4(|n|+1/2)$, where n is the LL index [139]. Plateaus corresponding to lower value of R_{XY} can also be seen at $V_G \sim$ - 2 V ($v = 6$) and $V_G \sim$ - 25 V ($v =$

10). As the temperature increases to $T = 100$ K (Figure 7.7b) and 200 K (Figure 7.7c), the quantum Hall plateaus tend to narrow.
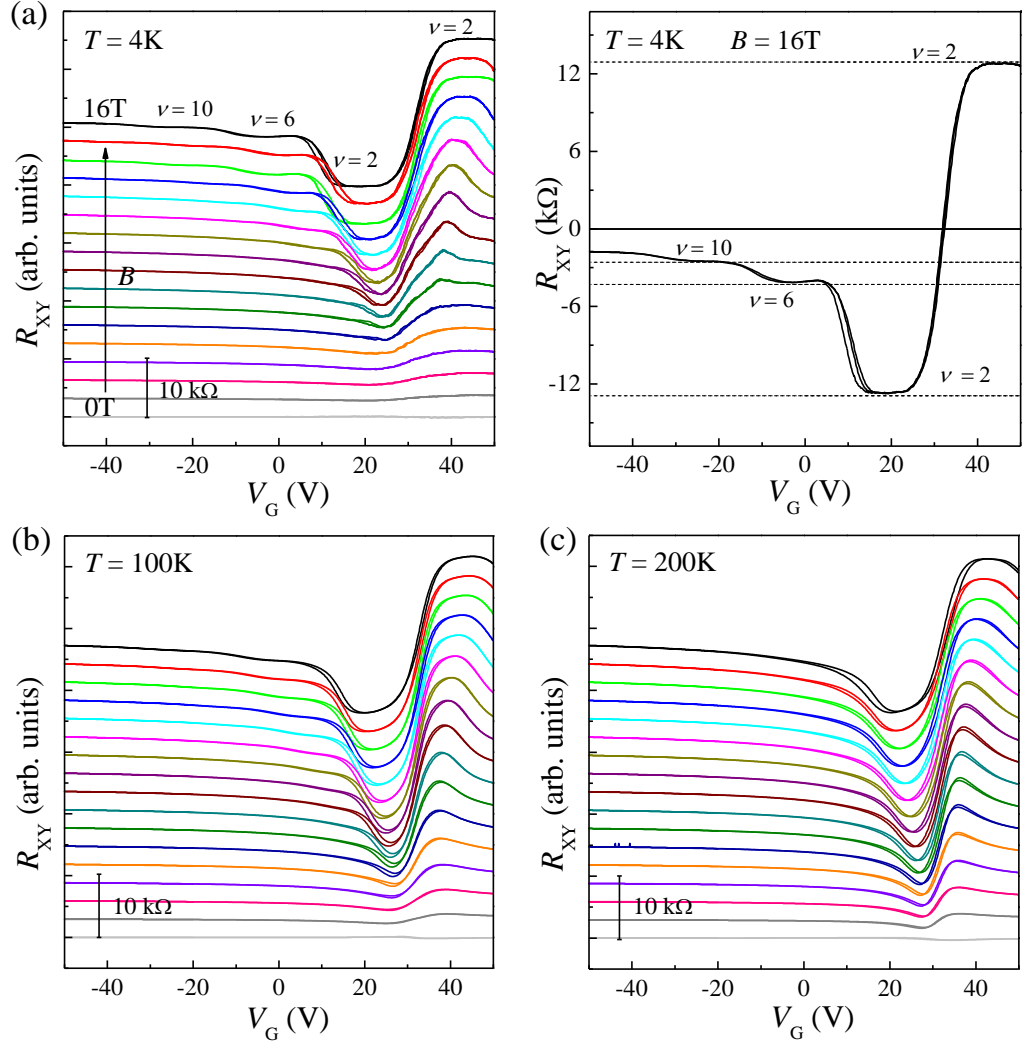
Figure 7.7. $R_{XY}(V_G)$ curves for CG at different temperatures: (a) $T = 4$ K, (b) $T = 100$ K and (c) $T = 200$ K, and magnetic field ranging from $B = 0$ T to 16 T in 1 T steps ($I = 1$ μA). The right panel in part (a) shows the $R_{XY}(V_G)$ curve at $B = 16$ T and $T = 4$ K. Dashed lines correspond to the quantized values of R_{XY}.

A further increase of temperature to $T \geq 300$ K (Figure 7.8a and 7.8b) induces a prononuced hysteresis in the $R_{XY}(V_G)$ curves as the magnetic field, B is increases from 0 T to 16 T.
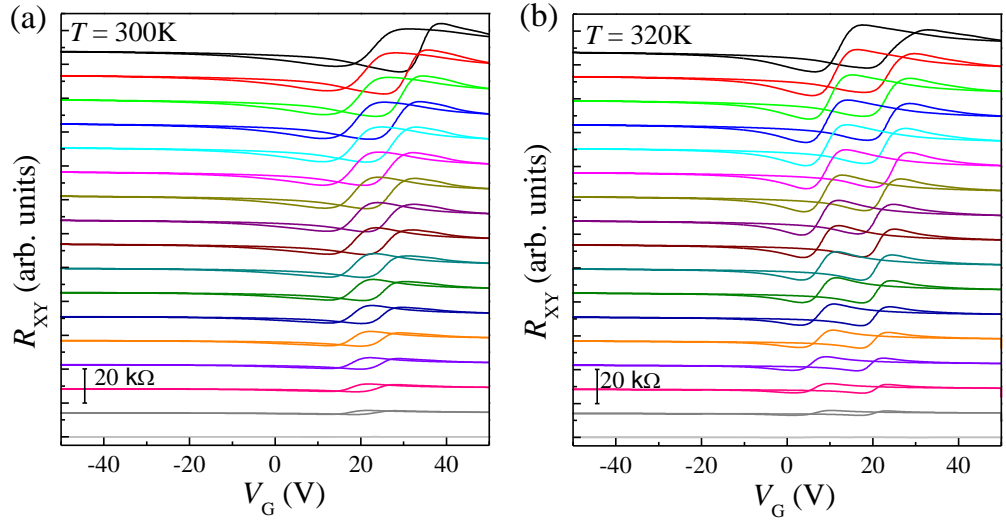
Figure 7.8. $R_{XY}(V_G)$ curves for CG at (a) $T = 300$ K and (b) $T = 320$ K. The magnetic field ranges from $B = 0$ T to 16 T in 1 T steps ($I = 1$ μA).

Figure 7.9 shows the colour contour plots of R_{XY} versus V_G and B at $T = 300$ K for different (up/down) sweeps of V_G. These data illustrate the sign of the $v = 2$ QH plateau and its evolution with increasing values of B and V_G. In particular, it can be seen that the neutrality point V_{NP} shifts to larger positive V_G with increasing B.
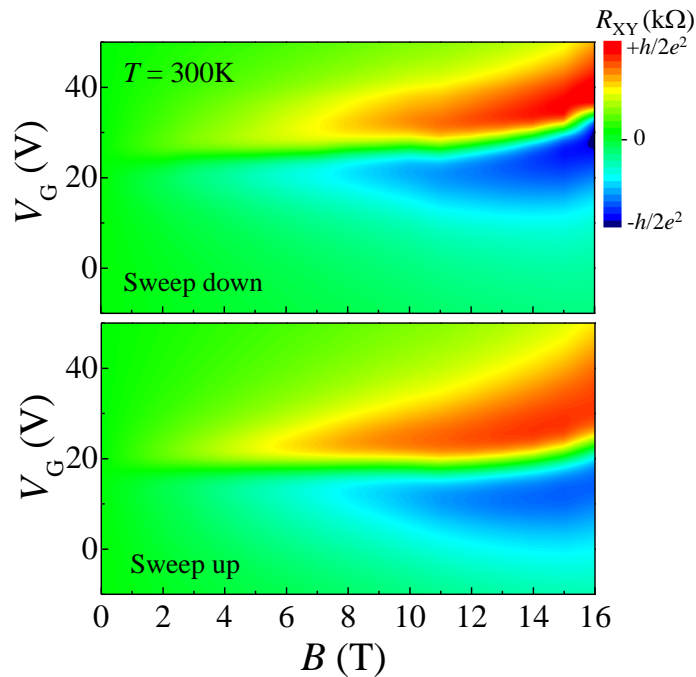
Figure 7.9. Colour plots of R_{XY} versus B and V_G at $T = 300$ K for different sweeps (top: sweep down; bottom: sweep up).

From Figure 7.7 and 7.8 it can be seen that the $v = 2$ QH plateau is accompanied by a hysteresis that depends on T and B. This behaviour is shown in more detail in Figure 7.10a where the $R_{XY}(V_G)$ curves are plotted for $B = 16$ T at different T. To quantify the hysteresis, we consider the gate voltage at which $R_{XY}(V_G)$ goes to zero (*i.e.* the charge neutrality point) on the sweep up (V_{Gu}) and sweep down (V_{Gd}) branches of the $R_{XY}(V_G)$ curves. The difference between the two values, $|\Delta V_G| = |V_{Gu} - V_{Gd}|$, is shown in Figure 7.10b for different T and B.
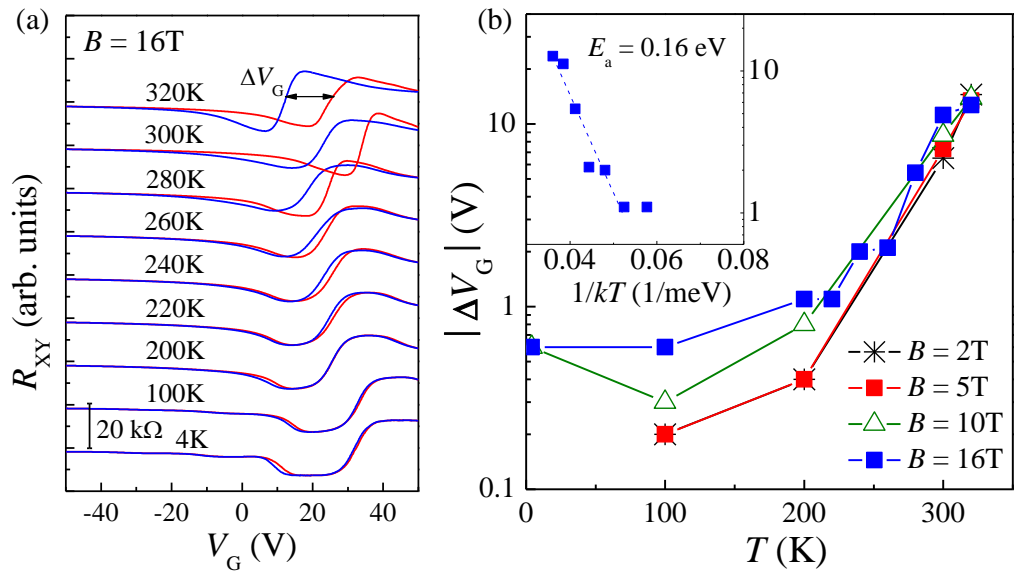
Figure 7.10. (a) $R_{XY}(V_G)$ curves for $B = 16$ T and different temperatures T for CG. The sweep up/down branches are shown in blue and red, respectively. For clarity, curves are displaced along the vertical axis. ΔV_G is the amplitude of the hysteresis in $R_{XY}(V_G)$, as estimated from the voltage at which $R_{XY}(V_G) = 0$. (b) Amplitude of the hysteresis $|\Delta V_G|$ versus T at different B. For $T = 4.2$ K and $B \leq$ 5 T, the value of $|\Delta V_G|$ is zero. Inset: Arrhenius plot of $|\Delta V_G|$ versus $1/T$ at $B =$ 16 T. The dashed line is an exponential fit to the data.

For $T < 200$ K, the value of $|\Delta V_G|$ is weakly dependent on T and tends to increase with B. For $T > 200$ K, the hysteresis becomes more pronounced and can be described by the relation $|\Delta V_G| \approx \exp(-E_a/kT)$, where E_a is an activation energy given by $E_a \approx 0.16$ eV for $B = 16$ T (Arrhenius plot in the inset

of Figure 7.10b). From Figure 7.10a, it can also be seen that increasing T above $T = 100$ K leads to a shift of the neutrality point to lower values of V_G, corresponding to an increasing density of electrons in graphene. This behaviour is not observed in pristine graphene and is assigned to the thermal excitation of electrons from CIPS onto graphene. For lower T ($T = 4.2$ and 100 K), the shift of the neutrality point is towards higher values of V_G with increasing T, indicative of a thermal excitation of carriers near the Dirac point.

Due to the hysteresis and slow charge transfer in CG, the measurement of R_{XX} and R_{XY} versus magnetic field at a given V_G require special consideration. For each measurement of the $R_{XY}(B)$ and $R_{XX}(B)$ curves at a given V_G, the gate voltage was increased by small increments ($\Delta V_G/\Delta t = 0.1$ V/s) starting from $V_G = 0$ V until reaching the required value of V_G. The temporal dependence of R_{XY} and R_{XX} at $B = 0$ T was then followed over intervals of several minutes, as required for R_{XY} and R_{XX} to reach stable values. The magnetic field was then swept from $B = 0$ T to 16 T (sweep rate of 5 mT/s) at a given V_G. The values of V_G were selected according to the $R_{XY}(V_G)$ curves in Figure 7.7, 7.8 and 7.9, showing plateaus on each side of the neutrality point (between the $n = 0$ and $n = \pm 1$ LLs) due to holes ($V_G \sim + 20$ V) or electrons ($V_G \sim + 40$ V).

Figure 7.11a shows the $R_{XY}(B)$ curves of CG for $V_G = + 20$ V at $T = 4$ K and 300 K. It can be seen that the $R_{XY}(B)$ curves exhibit a weak T-dependence; in particular, the approach to the $v = 2$ QH plateau tends to shift to lower B-fields at $T = 300$ K. The value of R_{XY} at the plateau and its stability over time depend on the gate voltage (as shown in Figure 7.13a and A4).
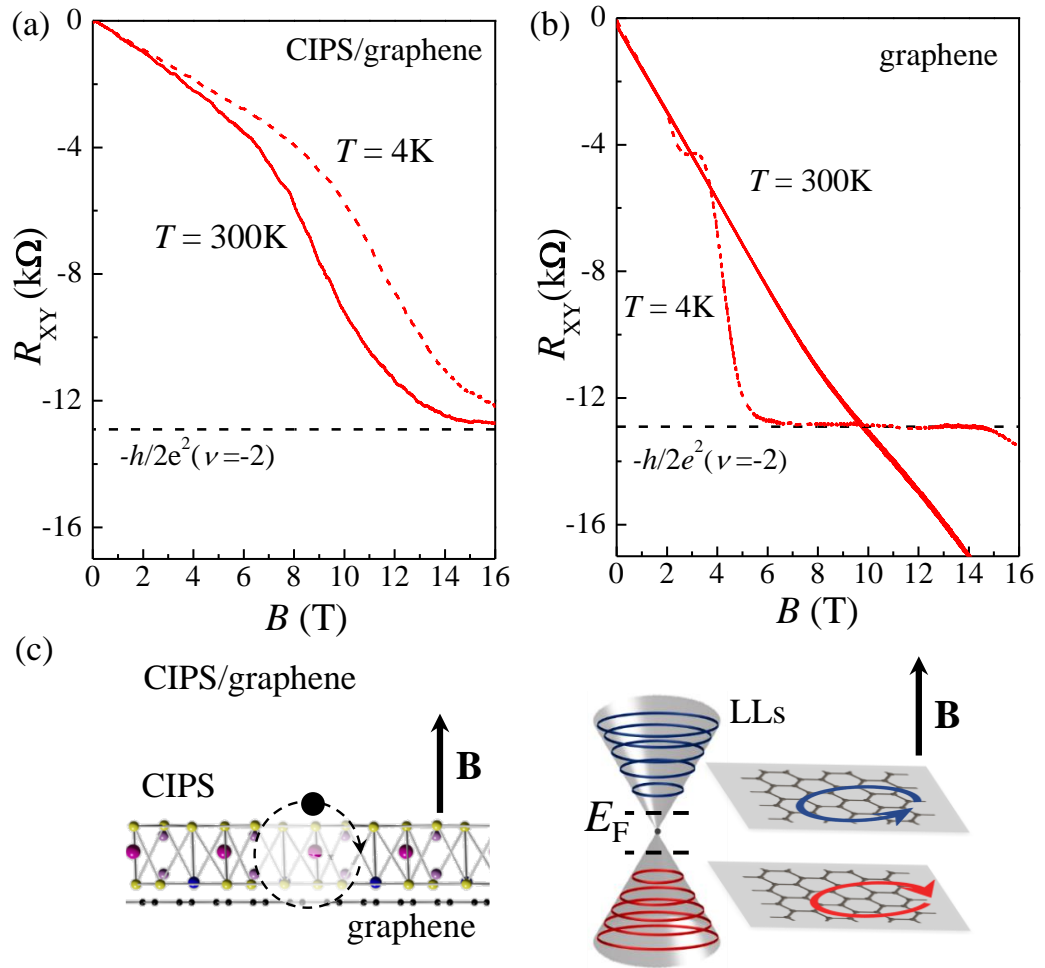
Figure 7.11. (a-b) Hall resistance R_{XY} versus magnetic field B at $T = 4$ K and $T = 300$ K in (a) CG ($V_G = + 20$ V, $I = 1$ μA) and (b) pristine graphene ($V_G = + 3$ V, $I = 1$ μA). (c) Left: Bound states in CIPS/graphene. Right: Landau levels (LLs) in graphene with Fermi level aligned between the $n = 0$ and $n = \pm1$ LLs corresponding to the $v = 2$ QH plateau.

We have observed similar behaviours in other devices (Figure 7.12), although the threshold in B for the $v = 2$ QH plateau may differ depending on the quality of the graphene layer. The graphene layer can contain imperfections and impurities that are introduced during the growth and/or during the transfer of graphene from the Cu to the SiO_2/Si substrate. This source of disorder can play a critical role on the $v = 2$ QH plateau. This is shown in Figure 7.12b where the $v = - 2$ QH plateau is approached at higher B than in the other devices due to low

quality of the graphene layer. The behaviour of CIPS/graphene contrasts with the strong temperature dependence of the $v = 2$ QH plateau in pristine graphene (Figure 7.11b and Figure A5). Although the analysis of the QH plateau in proximity of the charge neutrality point V_{NP} is complicated by the contribution of both electrons and holes to the conductivity, we can select gate voltages at which a QH plateau is observed for both holes and electrons (Figure 7.9, 7.12 and 7.13a).
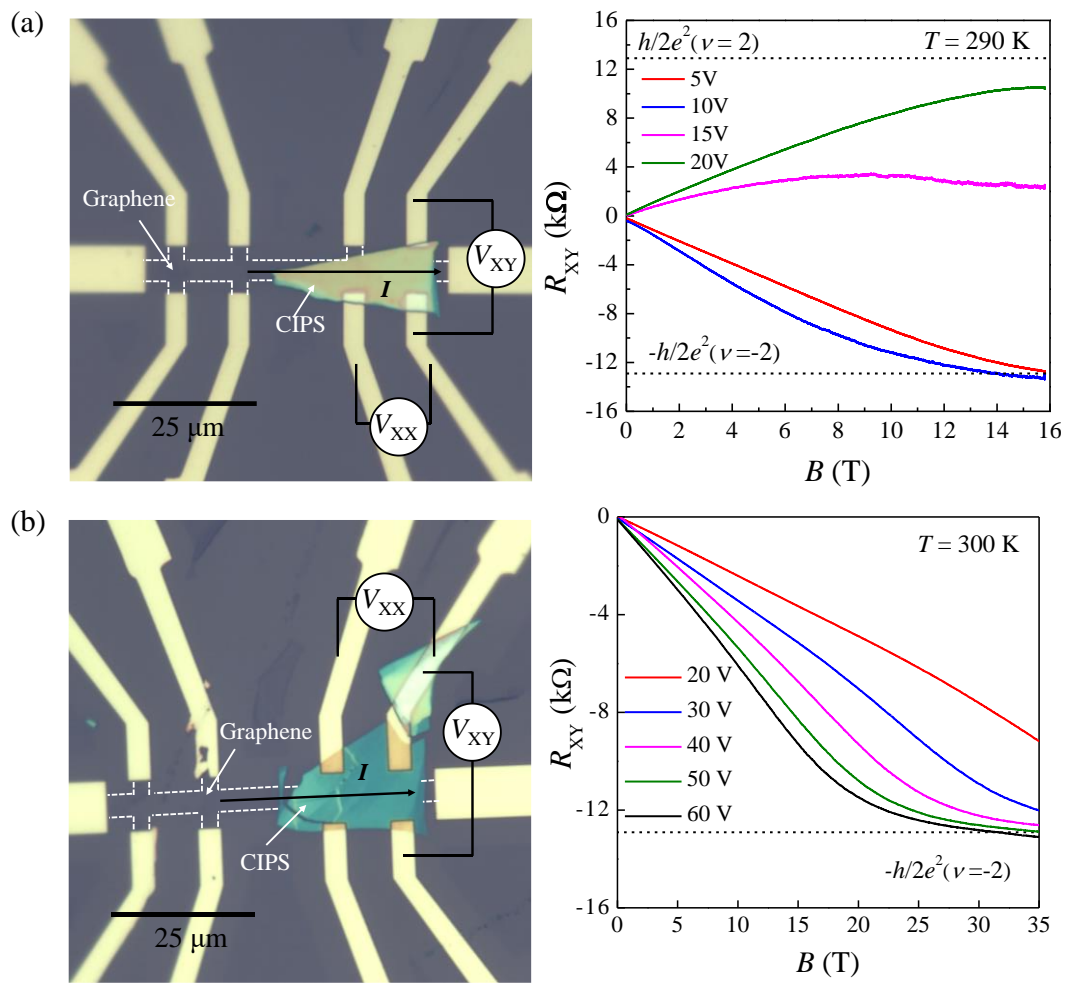
Figure 7.12. (a-b) Additional graphene Hall bar devices with one section encapsulated with a CIPS layer. Inset: Corresponding $R_{XY}(B)$ curves measured at different V_G.

The plateau in $R_{XY}(B)$ is paralled by a corresponding decrease in $R_{XX}(B)$ (Figure 7.13b and Figures A4 at low temperatures). However, we note that R_{XX}

does not go to zero at values of B corresponding to the $v = 2$ QH plateau; also, we observe a small deviation of R_{XY} from its nominal quantized value ($h/2e^2$). This can also be seen in pristine graphene at low temperatures (Figure A5). As shown in Figure 7.13c, this deviation (ΔR_{XY}) depends on R_{XX} and tends to zero for decreasing R_{XX}. Here, different values of R_{XX} and R_{XY} were obtained from measurements of the same CG device at different T, B and/or V_G after the onset of the $v = 2$ QH plateau in $R_{XY}(B)$.
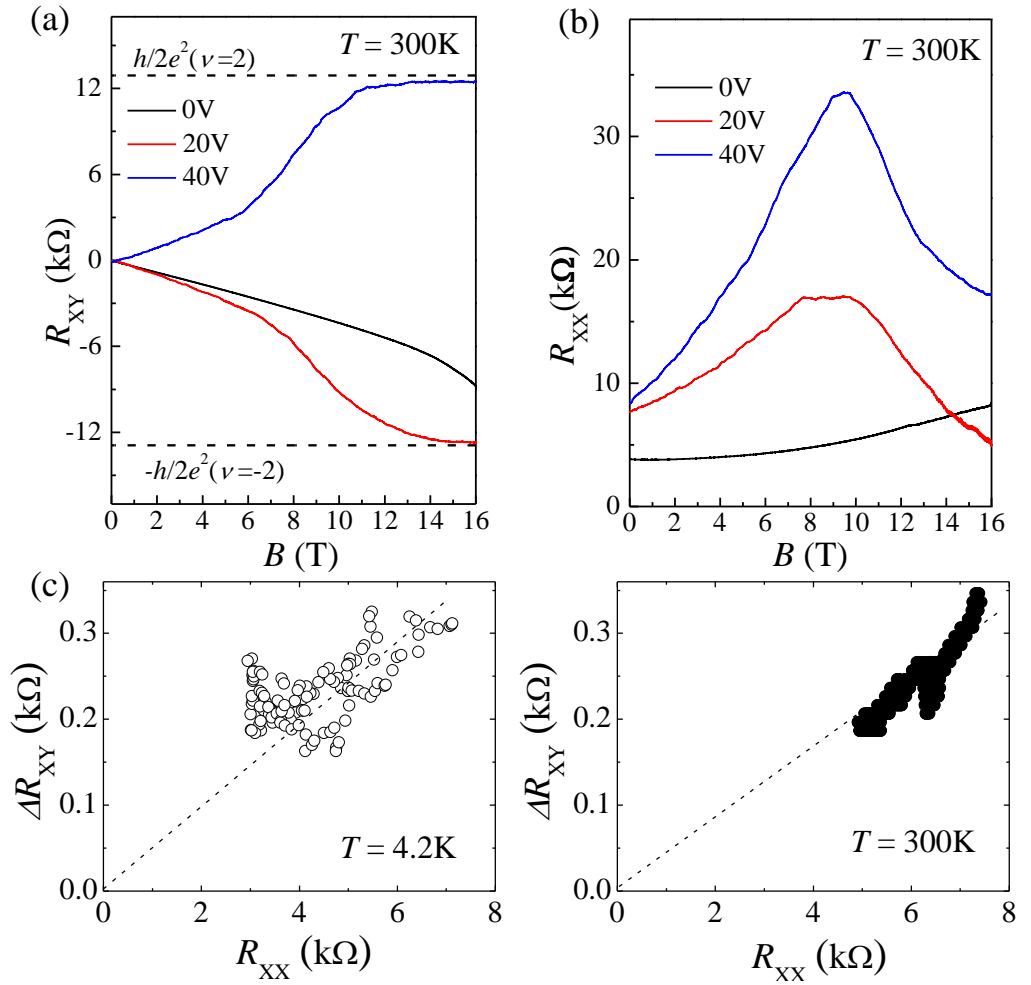
Figure 7.13. (a) R_{XY} versus B for CG at different V_G and $T = 300$ K ($I = 1$ μA). (b) R_{XX} versus B for CG at different V_G and $T = 300$ K ($I = 1$ μA). (c) Deviation of R_{XY} from quantized value at the $v = 2$ QH plateau ($h/2e^2$) versus R_{XX}, as derived from measurements at different T, B and V_G (Left: $T = 4.2$ K, $B = 16$ T, $V_G = 42$-28 V and 16-22 V; Right: $T = 300$ K, $B = 14$-16 T, $V_G = 20$ V). Dashed lines are guides to the eye.

Our data indicate a coupling between R_{XX} and R_{XY} that could be accounted for by geometrical effects and/or disorder. A non-uniform channel can exhibit regions that do not have minimal resistance at the same magnetic field. This results in an effective misalignment of the Hall probes so that the measured Hall resistance R_{XY} is influenced by the longitudinal resistance R_{XX} [154]. Also, disorder can play an important role on the $v = 2$ QH plateau due to the coexistence and contribution to the transport of both electrons and holes [155]. Using the data in Figure 7.13c, we estimate the coupling parameter $s = \Delta R_{XY}/R_{XX}$. A linear fitting of ΔR_{XY} versus R_{XX} indicates $s = 0.04$ (0.05) at $T = 300$ K ($T = 4.2$ K). Our values are similar to the value ($s = 0.038$) for high-quality graphene/SiC devices reported in the recent literature [156].

7.4 Room temperature quantum Hall effect

The room temperature QHE has been reported previously in pristine graphene and explained in terms of the unique magnetic field quantization of Dirac fermions in graphene [128]. The LL quantization energy of fermions in magnetic field is $E_n = v_F \sqrt{2e\hbar B \mid n \mid}$. For $n = \pm 1$ and $B = 45$ T, $E_n \sim 250$ meV, which greatly exceeds the thermal energy (~ 26 meV) of charge carriers at room temperature. However, the physics behind the room-temperature QHE in graphene is generally more complex and requires an understanding of the anomalous nature of the $n = 0$ LL [157]. The thermal activation energy for the quenching of the $v = 2$ QH plateau in graphene approaches the theoretical cyclotron energy gap only at high magnetic fields ($B \sim 30$ T). At high B, the number of states with zero energy ($n = 0$ LL) is only determined by the total magnetic flux and does not depend on disorder. Thus, the $n = 0$ LL is well

separated from its neighbouring ($n = \pm 1$) LLs and the activation energy corresponds approximatively to $E_1 = v_F \sqrt{2e\hbar B}$; however, for lower B, LL mixing due to disorder acts to broaden the LLs by means of inter-LL scattering, leading to an activation energy smaller than E_1. Thus, the observation of the $v = 2$ QH plateau at room temperature in graphene requires large B (> 20 T) that are accessible only in a few high B facilities. In our CIPS/graphene sample the $v = 2$ QH plateau is observed at relatively small B at $T = 300$ K, yet it is not seen in pristine graphene in the same range of B, our results merit further consideration.

First, we note that the CIPS layer can act as a remote source of carriers for graphene. Our measurements demonstrate that the charge transfer at the CIPS/graphene interface is tuneable by gating and is temperature dependent. Regions of CIPS with different densities of localized states tend to charge and discharge with a similar slow (~ 100 s) time constant at room temperature, thus accounting for the gate-induced hysteresis in the transport characteristics (Figure 7.2). The hysteresis in the transfer characteristics of CG becomes significant only at $T > 200$ K (Figure 7.5 and 7.6), symptomatic of a thermal activation and slow transfer of charges from/to the CIPS layer onto graphene.

For sufficiently high temperatures ($T > 200$ K), electrons (and holes) in the localized states of CIPS are in equilibrium with the current-carrying, delocalized states of graphene. Under these conditions, stable bound states are formed in CIPS/graphene. In contrast, at low T such equilibrium cannot be established and the hysteretic behaviour is not observed. Also, a comparison of the transfer characteristics and their hysteresis for CG at $B = 0$ and 16 T indicates that the charge transfer is influenced by a large quantizing magnetic field. The magnetic field acts to enhance the hysteretic behaviour and distorts the V_G-dependence of

R_{XX} around the charge neutrality point. As shown in Figure 7.6c and 7.9, for B ≥ 10 T the bright colour regions in R_{XX} and R_{XY} corresponding to the zeroth LL tend to shift to larger V_G with increasing B, consistent with a reduced transfer of electrons from the CIPS layer onto graphene due to an increased localization of charges in the quantizing magnetic field. This can also be seen in Figure 7.10b, where the hysteresis (as measured by $|\Delta V_G|$) increases with B.

Reference [145] offers an insight into the role of localized charges near the surface of graphene: For a range of chemical potentials inside the gap between the zeroth and first LLs, charged impurities at a distance of the magnetic length from the graphene layer can form stable molecules bound by free carriers of opposite sign in graphene [145]. The optimal distance between charges in the bound state is of the order of the magnetic length $l_B = \sqrt{\hbar/(eB)}$ and their binding energy scales as $E_B = (\hbar v_F/l_B)$. For B = 16 T, this gives $l_B = 6.4$ nm and $E_B = 0.10$ eV. This binding energy is comparable to our estimate (0.16 eV) derived from the T-dependent hysteresis in R_{XY} (Figure 7.10b). Thus, for sufficiently high temperatures, electrons (and holes) in the localized states have a binding energy that exceeds the cyclotron energy gap.

We note that a strongly disordered system cannot show the QHE because no LL quantization can occur. However, it is well established that the standard picture of QHE requires the existence of localized states due to disorder to enable the Fermi level to be pinned between the extended states of adjacent LLs. The disorder is a key feature of the QH effect and its thermal stability. Localized states due to disorder can act to pin the Fermi level between LLs in graphene, maintaining the Hall voltage on the $v = 2$ QH plateau. The charge transfer

between CIPS and graphene is reversible, leading to a $v = 2$ QH plateau for both electrons and holes (Figure 7.9, 7.11 and 7.13).

We now consider our findings in the context of ongoing research on other hybrid systems based on graphene. For example, the use of a conducting layer, such as the small band gap (~ 1.3 eV at $T = 300$ K) semiconductor InSe to form an InSe/graphene FET, facilitates the observation of a giant QH plateau, but its observation at room temperature is prevented by parallel conduction in the InSe layer [143, 144]. The use of a high-resistance dielectric poses instead other opportunities and challenges. A giant QH plateau has been reported in graphene grown epitaxially by the thermal annealing of a SiC dielectric substrate. In this case, the charge transfer at the SiC/graphene interface involves defects in SiC with a high densities of states (10^{14} cm^{-2} eV^{-1}) in close proximity to graphene [138-142]. These states arise from atomic defects within the first few SiC layers and are created during the formation of the graphene layer by Si-sublimation. For graphene on SiC, the giant QH effect was reported at temperatures of up to $T \sim 100$-200 K, suggesting that the bound states in SiC/graphene have a relatively small binding energy even at high magnetic fields ($B > 20$ T). Alternatively, hexagonal boron nitride (hBN) represents an ideal dielectric for graphene-based FETs [55]. Charge and surface fluctuations in hBN tend to be weaker than in other substrates, such as SiO$_2$. Thus, graphene on hBN has a high-mobility and is well suited for observations of integer and fractional quantum Hall effects [158, 159]. In particular, the formation of moiré superlattices in rotationally misaligned graphene/hBN layers can promote interfacial charge transfer and new quantum transport regimes [160-163]. More recently, a hybrid system based on CrOCl-graphene also revealed an exotic QH effect phase due

to the formation of a long-wavelength charge order [164]. In all these different hybrid systems, the band structure of graphene is modulated around the Dirac cone as a result of an interfacial charge transfer involving a semiconductor or an insulator. However, for all these systems the observation of quantum effects at high temperatures has proven to be challenging. Our choice of CIPS provides an effective layer for charge transfer as CIPS is a dielectric and its defect states are not only sufficiently dense ($\sim 10^{12} \, \text{cm}^{-2} \, \text{eV}^{-1}$), but also they form bound states with graphene that are sufficiently deep to be resilient to ionization at room temperature. The range of high temperatures ($T > 200$ K) for charge transfer and hysteresis in the transport curves corresponds to that required for activating the thermal motion of the Cu-ions [28, 165] out of the CIPS layer planes. This can lead to localized ionic charges whose slow motion could be responsible for the slow dynamics of charge transfer at the graphene/CIPS interface, leading to the hysteretic transport observed in this system. Since CIPS is a dielectric layer and electrons remain bound onto its localized states, the QH voltage in graphene is not short-circuited by a significant parallel conduction in the CIPS layer.

7.5   Summary

In conclusion, the controlled transfer of charges between graphene and localized states in its proximity provide a route for the observation of quantum effects at room temperature and in relatively small applied magnetic fields. We have shown that the electric field-induced transfer of charge between the localized states in the CIPS and graphene layers acts to increase or decrease the carrier density in graphene, causing a change in its resistance that is gate-tuneable at high temperatures ($T > 200$ K). The charge transfer causes hysteretic

behaviours in the electrical characteristics due a slow dynamic exchange of electrons between graphene and localized states in its proximity. Prospects for further research include a more accurate resistance quantization, which requires progress in both material growth and fabrication processes. It requires high-mobility homogenous graphene, an homogenous charge transfer at the graphene/CIPS interface, and the fabrication of low-resistance contacts. A more uniform CIPS/graphene heterostructure could be achieved by the development of scalable growth techniques (for example using epitaxial graphene grown with intrinsic structural alignment on SiC) together with the fabrication of high-quality electrical contacts, such as electrodes with the edge-contact geometry [166]. Thus, there are prospects for further studies and engineering interfacial charge transfer in hybrid systems based on graphene for the observation of quantum effects over a wide parameter space beyond the current state-of-the-art for a wide range of applications, such as graphene-based resistance standards for the new International System of Units [167].

Chapter 8

Conclusions and Outlook

The primary objective of this PhD project was to investigate the functionalisation of graphene by CIPS, a 2D ferroelectric material. The scope of the project has widened and adapted considerably as new phenomena were observed, such as a room temperature quantum Hall effect in CIPS/graphene heterostructures. Some of the keys findings and prospects for further studies are discussed below.

CIPS has a disordered crystal structure as evident from the photoluminescence (PL) spectra of bulk and thin layers. Although the Raman spectra show no significant changes in the position of the vibrational modes for bulk and thin CIPS layers, the PL spectra reveals a multi-band emission below the band gap energy ($E_g = 2.7$ eV at $T = 300$K) due to the presence of localised defect states within the band gap. The PL energy peak position is weakly affected by temperature for both bulk and thin layers. The temperature dependent PL spectra for thin layers show a significant decrease in PL intensity for $T > 200$ K, which coincides with the temperature required for thermal activation of Cu ions, leading to progressive disorder in the crystal structure of CIPS.

Unlike many 2D ferroelectrics, CIPS is well suited for use as a gate in field-effect transistors (FETs). Using a hybrid FET with a graphene channel gated through a CIPS layer, we investigated charge transfer phenomena at the CIPS/graphene interface. The hysteresis in the transfer characteristics can originate not only from a gate-induced ferroelectric polarisation but also from other mechanisms, such as charge trapping in the CIPS layer. The gate voltage

induces charges in the graphene layer, which then redistribute between graphene and CIPS. This time-dependent charge transfer process is slow ($\tau > 100$ s) and causes hysteresis in the transport characteristics that depends on the sweep rate and range of the applied gate voltage V_G. The temperature of the sample also plays a crucial role in this charge transfer process. The pronounced hysteresis and the temporal dynamics of the resistance at large V_G and temperature $T > 200$ K suggest a slow charge transfer at the interface mediated by defects with deep localised states in the band gap of CIPS. We believe that the defects responsible for the hysteresis may result from the migration of Cu ions. The charge transfer across the CIPS/graphene interface is also affected by light. Light illumination results in photo-ionisation of defects in CIPS leading to an increased charge transfer at the interface. The hysteresis and slow dynamics of the resistance change under light illumination are indicative of light-activated slow redistribution of charges leading to a dynamical disorder effect tunable by light.

We also examined the electrical properties of thin CIPS layers by considering a tunnel junction comprising of a thin CIPS tunnel barrier sandwiched between two electrodes based on a few layer graphene. The shape of the hysteresis in the transport characteristics is influenced by both ferroelectric polarisation and charge transfer at the interface. The hysteretic behaviour tends to weaken with temperature $T > 300$ K, suggesting that the ferroelectric switching is weakened by a thermally activated charge transfer.

Finally, we studied graphene Hall bars where one section of the graphene channel is capped by CIPS. In these devices CIPS provide an effective layer for charge transfer at the CIPS/graphene interface due to a high density of defect states. These defect states act as trap of carriers and are sufficiently deep to be

106

ionised only at $T > 200$K. Electrostatic gating of the graphene enables the Fermi energy to be tuned so that electrons in the localized states of CIPS are in equilibrium with the current-carrying, delocalized states of graphene. This leads to strongly bound states in this hybrid system, which at room temperature can pin the graphene Fermi level maintaining the Hall voltage on the $v = 2$ plateau. The quantum Hall effect is found to be weakly dependent on temperature and is observed at room temperature over a range of widely accessible applied magnetic fields. This is interesting since to date a room temperature resistance quantum has been reported only in high mobility graphene at large magnetic fields available only in few high magnetic field laboratories.

Overall, the studies presented in this thesis have helped to deepen our understanding of a new class of hybrid heterostructures based on 2D ferroelectrics. These devices display complex charge transfer dynamics and we have attempted to unravel and model their behaviour using electrical gating, magnetic field and light excitation. This offers great potential in developing ferroelectric field effect transistors (FeFETs) for non-volatile memory applications since conventional ferroelectrics have limited memory retention and endurance. The understanding of the interfacial charge transfer mechanism in these hybrid devices can also help to realise graphene based resistance standards that can be used at high temperatures and at lower magnetic fields unlike conventional graphene or GaAs based standards. Prospects for further research include investigations over a wide range of applied magnetic fields and the development of heterostructures that incorporate an intermediate tunnel barrier, such as a tunnel barrier between CIPS and graphene to tune the rate of charge

transfer and its thermal activation. Heterostructures with high-mobility carriers could also enable the optimization of the QH plateau.

Appendix

A1.   Surface microscopy studies

The thickness of the CIPS layer in the device is in the range of $t = 20$ nm to 50 nm, as measured by AFM (Figure A1a). The root mean square (RMS) roughness on CIPS is ~ 260 pm. The piezoresponse force microscopy (PFM) image reveals a higher contrast for CIPS over graphene (Figure A1b).

(a) Topography   (b) PFM Amplitude
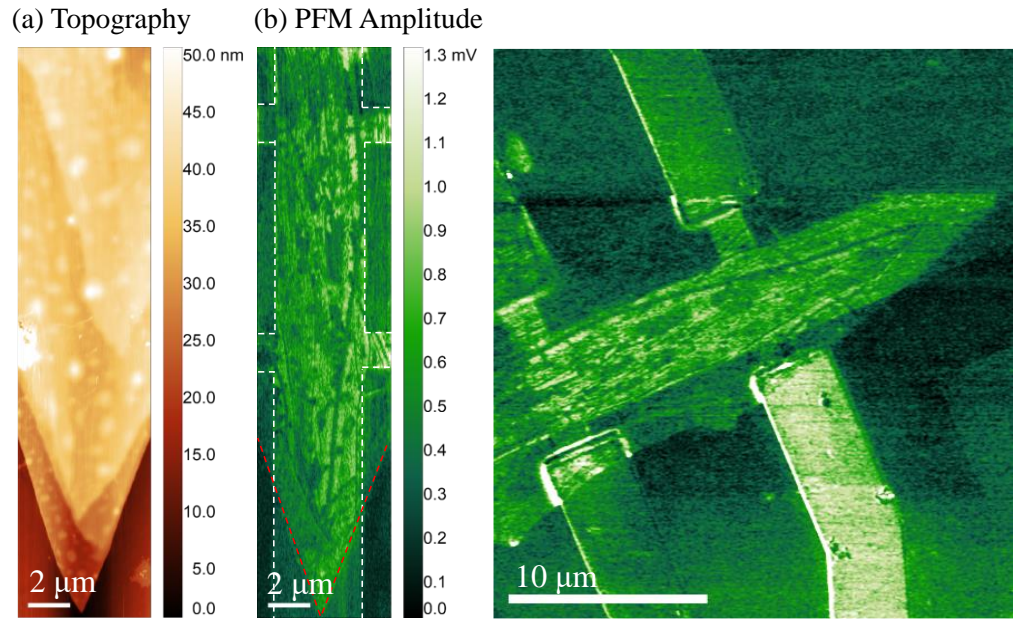
Figure A1. (a) AFM topography of CIPS/graphene showing a non-uniform CIPS layer. (b) PFM amplitude for CIPS/graphene measured using a NuNano Spark 350 cantilever with frequency $f_{AC} = 17$ kHz.

A2.   Hall carrier density in CIPS/graphene

The gate voltage dependent carrier density of CG was derived from the Hall resistance $R_{XY}(V_G)$ curves at $T = 4$ K and 300 K using the relation $R_{XY} = \frac{B}{n \times e}$, where B is the applied magnetic field and e is the electron charge. Figure A3a shows no hysteresis in the carrier density plots at $T = 4$ K. The step-like features appear as the magnetic field is increased to $B = 16$ T due to the quantum

Hall effect. When the temperature is increased to $T = 300$ K, hysteresis effects dominate the carrier density plots (Figure A2b).
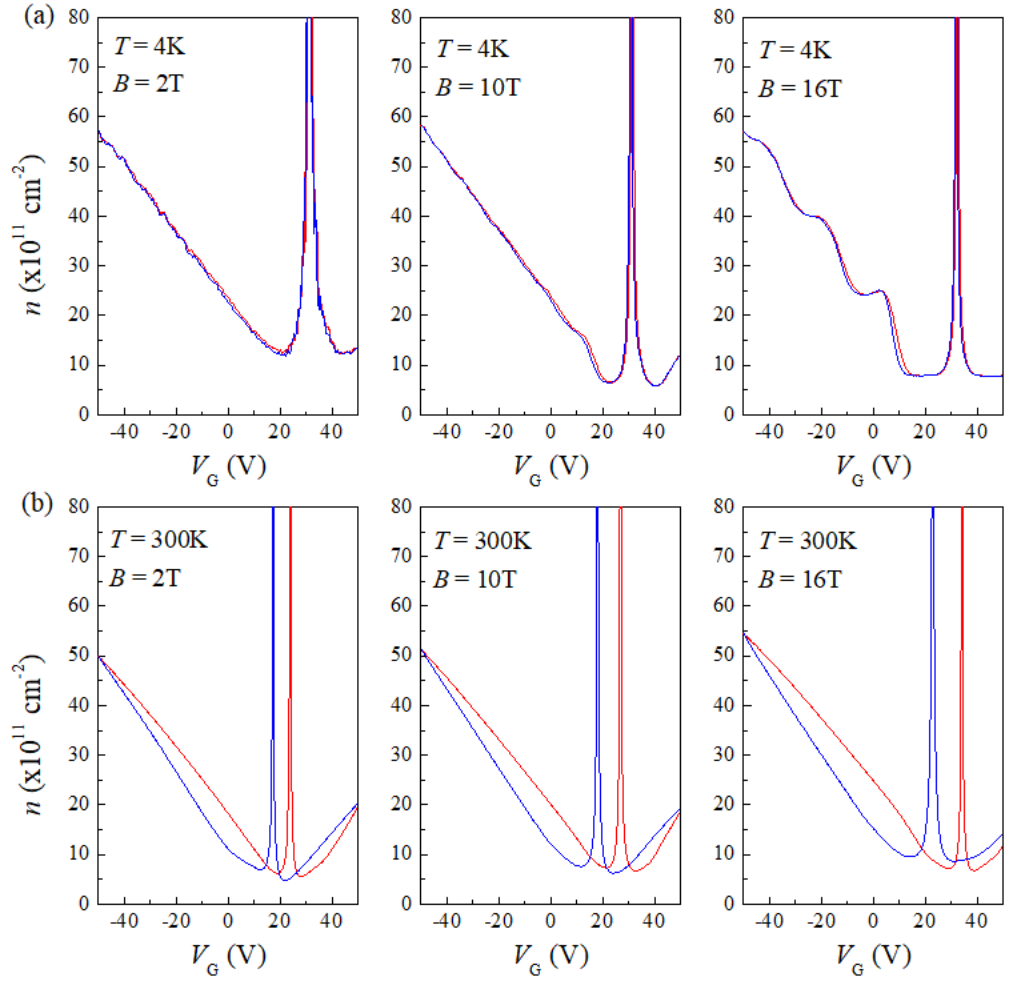
Figure A2. $n(V_G)$ plots as extracted from the $R_{XY}(V_G)$ curves at (a) $T = 4$ K and (b) $T = 300$ K for different magnetic fields. The sweep up/down branches are shown in blue and red, respectively.

A3. Hall mobility in CIPS/graphene

The gate voltage dependent Hall mobility of CG as extracted from $R_{XX}(V_G)$ and $R_{XY}(V_G)$ curves at $T = 4$ K and 300 K is shown in Figure A3.

The Hall mobility, μ_H is calculated using the following relations,

$$\sigma_{XX} = \frac{1}{\rho_{XX}} = \frac{1}{\left(R_{XX} \times \frac{w}{l}\right)} \tag{A3.1}$$

$$R_H = \frac{R_{XY}}{B} \tag{A3.2}$$

$$\mu_{\mathrm{H}} = R_{\mathrm{H}} \times \sigma_{\mathrm{XX}} = \frac{R_{\mathrm{XY}}}{B} \times \frac{1}{\left(R_{\mathrm{XX}} \times \frac{w}{l}\right)} \quad . \tag{A3.3}$$

Here, $\frac{w}{l}$ is the width to length ratio of the CG channel, R_{H} is the Hall

coefficient, B is the magnetic field and μ_H is the Hall mobility. Figure A4a shows

negligible hysteresis in the Hall mobility plots at low temperature ($T = 4$ K). The

maxima and minima features in the $\mu_{\mathrm{H}}(V_{\mathrm{G}})$ plot at $B = 16$ T arise from the LL

quantisation. In contrast, at $T = 300$ K (Figure A3b), the $\mu_{\mathrm{H}}(V_{\mathrm{G}})$ plots are

dominated by hysteresis irrespective of the applied magnetic field. We have used

data at low B (negligible quantization) to estimate the transport parameters of

our samples.
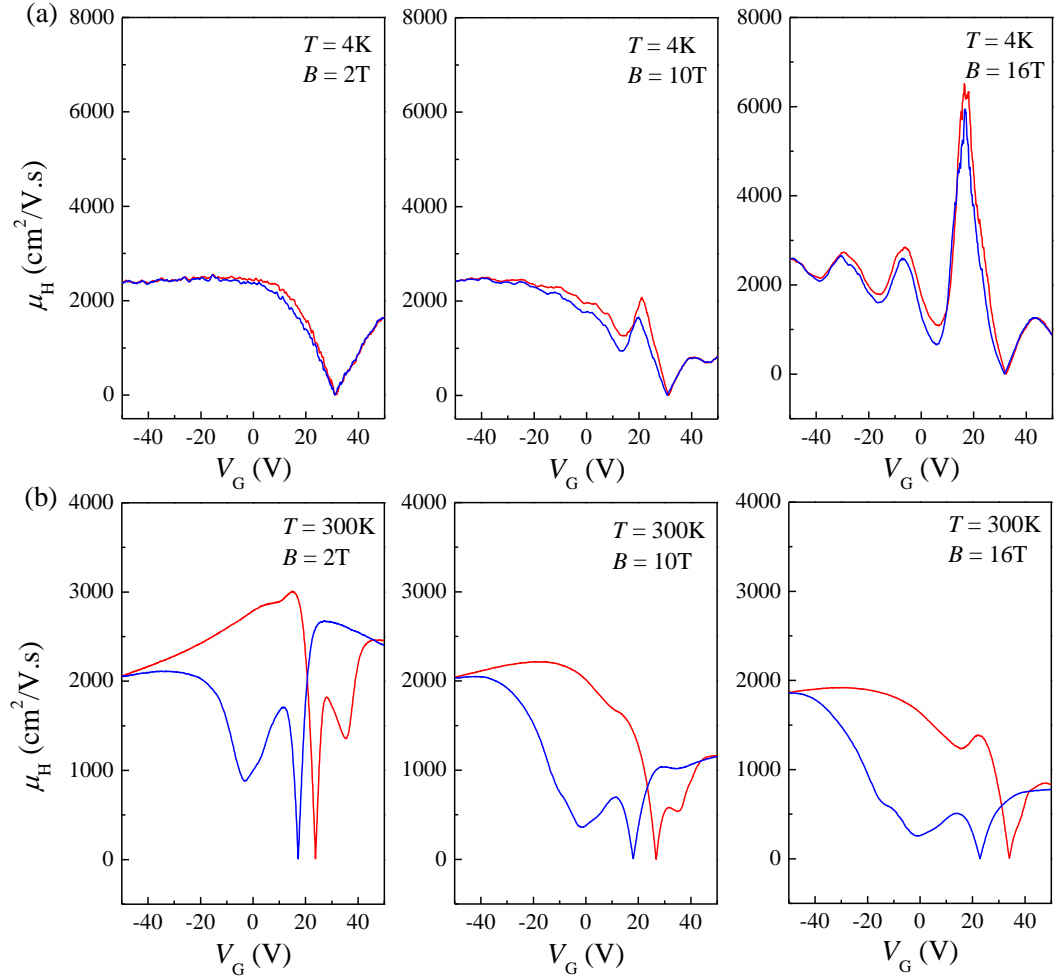
Figure A3. $\mu_{\mathrm{H}}(V_{\mathrm{G}})$ plots as extracted from $R_{\mathrm{XX}}(V_{\mathrm{G}})$ and $R_{\mathrm{XY}}(V_{\mathrm{G}})$ curves at (a) $T = 4$ K and (b) $T = 300$ K for different magnetic fields. The sweep up/down branches are shown in blue and red, respectively.

A4. Low temperature Hall measurements in CIPS/Graphene

Figure A4 shows the $R_{XY}(B)$ and $R_{XX}(B)$ measured simultaneously by sweeping the magnetic field from $B = 0$ T to $B = 16$ T for different gate voltages $V_G = 0$ V, $+ 20$ V and $+ 40$ V.
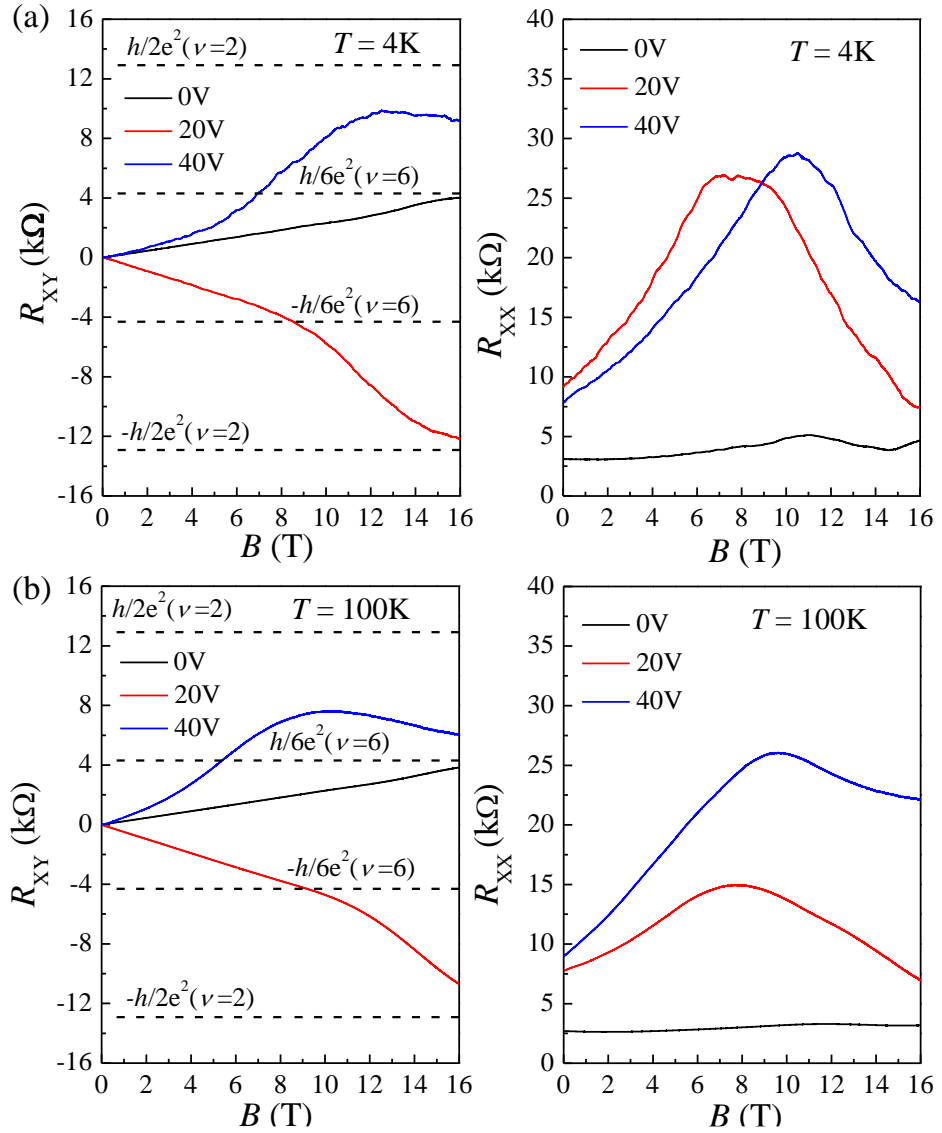
Figure A4. $R_{XY}(B)$ and $R_{XX}(B)$ curves for CG measured at different gate voltages for (a) $T = 4$ K and (b) $T = 100$ K.

We note that the presence of electron–hole puddles in disordered systems can affect the observation of the QH plateau. In particular, in the vicinity of the charge neutrality point, the Hall resistance displays no more well-defined

quantized plateaus due to the simultaneous contribution of electrons and holes to the conductivity.

A5. Magneto-transport in pristine graphene

Figure A5 shows the magnetic field dependent resistance of pristine graphene measured at $V_G = 3$ V and sweeping the magnetic field from $B = 0$ T to 16 T at different temperatures.
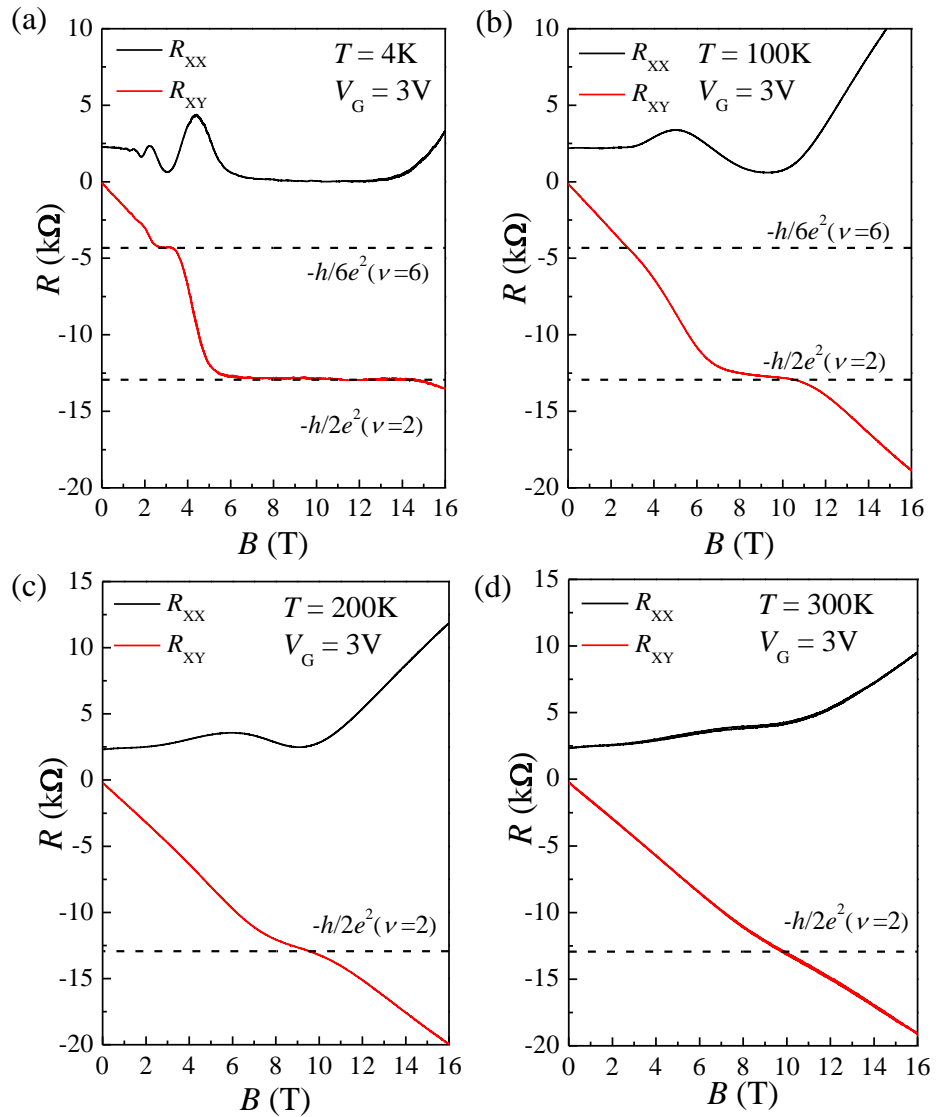
Figure A5. Resistance versus magnetic field curves for pristine graphene measured at a gate voltage $V_G = 3$ V ($I = 1$ µA) and temperatures: (a) $T = 4$ K, (b) $T = 100$ K, (c) $T = 200$ K and (d) $T = 300$ K. The black and red curves correspond to the longitudinal and Hall resistances, respectively. The dotted lines show the position of the $v = 2$ and $v = 6$ QH plateaus in R_{XY}.

The gate voltage was chosen in the vicinity of the neutrality point $V_{NP} = + 10$ V (Figure 7.2 inset). The gate voltage was increased from $V_G = 0$ V to $V_G = 3$ V by increments of 0.1 V and then the magnetic field was swept from $B = 0$ T to $B = 16$ T.

References

1.   Novoselov, K.S., et al., *Electric field effect in atomically thin carbon films.* Science, 2004. **306**(5696): p. 666-669.

2.   Novoselov, K.S., et al., *A roadmap for graphene.* Nature, 2012. **490**(7419): p. 192-200.

3.   Fiori, G., et al., *Electronics based on two-dimensional materials.* Nature Nanotechnology, 2014. **9**(10): p. 768-779.

4.   Chang, L.W., et al., *Size effects on thin film ferroelectrics: Experiments on isolated single crystal sheets.* Applied Physics Letters, 2008. **93**(13).

5.   Chang, L.W., et al., *Settling the "Dead Layer" Debate in Nanoscale Capacitors.* Advanced Materials, 2009. **21**(48): p. 4911-+.

6.   Sinnamon, L.J., et al., *Exploring grain size as a cause for "dead-layer" effects in thin film capacitors.* Applied Physics Letters, 2002. **81**(4): p. 703-705.

7.   Liu, F.C., et al., *Room-temperature ferroelectricity in CuInP2S6 ultrathin flakes.* Nature Communications, 2016. **7**: p. 6.

8.   Zhou, Y., et al., *Out-of-Plane Piezoelectricity and Ferroelectricity in Layered alpha-In2Se3 Nanoflakes.* Nano Letters, 2017. **17**(9): p. 5508-5513.

9.   Cui, C.J., et al., *Intercorrelated In-Plane and Out-of-Plane Ferroelectricity in Ultrathin Two-Dimensional Layered Semiconductor In2Se3.* Nano Letters, 2018. **18**(2): p. 1253-1258.

10.   Fei, Z.Y., et al., *Ferroelectric switching of a two-dimensional metal.* Nature, 2018. **560**(7718): p. 336-+.

11. Chang, K., et al., *Discovery of robust in-plane ferroelectricity in atomic-thick SnTe.* Science, 2016. **353**(6296): p. 274-278.

12. Yuan, S.G., et al., *Room-temperature ferroelectricity in MoTe2 down to the atomic monolayer limit.* Nature Communications, 2019. **10**.

13. Wan, S.Y., et al., *Nonvolatile Ferroelectric Memory Effect in Ultrathin -In2Se3.* Advanced Functional Materials, 2019. **29**(20).

14. Singh, P., et al., *Two-Dimensional CIPS-InSe van der Waal Heterostructure Ferroelectric Field Effect Transistor for Nonvolatile Memory Applications.* Acs Nano, 2022. **16**(4): p. 5418-5426.

15. Cho, Y., et al., *Nanowatt use 8 V switching nonvolatile memory transistors with 2D MoTe2 channel and ferroelectric P(VDF-TrFE).* Nano Energy, 2021. **81**.

16. Si, M.W., et al., *Ferroelectric Field-Effect Transistors Based on MoS2 and CuInP2S6 Two-Dimensional van der Waals Heterostructure.* Acs Nano, 2018. **12**(7): p. 6700-6705.

17. Si, M.W., et al., *A ferroelectric semiconductor field-effect transistor.* Nature Electronics, 2019. **2**(12): p. 580-586.

18. Jiang, X.X., et al., *Ferroelectric Field-Effect Transistors Based on WSe2/CuInP2S6 Heterostructures for Memory Applications.* Acs Applied Electronic Materials, 2021. **3**(11): p. 4711-4717.

19. Xie, S.H., et al., *Ferroelectric semiconductor junctions based on graphene/In2Se3/graphene van der Waals heterostructures.* 2d Materials, 2021. **8**(4).

20. Tang, W.H., et al., *A van der Waals Ferroelectric Tunnel Junction for Ultrahigh-Temperature Operation Memory.* Small Methods, 2022. **6**(4).

21.   Zhao, M., et al., *An ultrathin two-dimensional vertical ferroelectric tunneling junction based on CuInP(2)S(6)monolayer.* Nanoscale, 2020. **12**(23): p. 12522-12530.

22.   Wan, S.Y., et al., *Room-temperature ferroelectricity and a switchable diode effect in two-dimensional alpha-In2Se3 thin layers.* Nanoscale, 2018. **10**(31): p. 14885-14892.

23.   Belianinov, A., et al., *CuInP2S6 Room Temperature Layered Ferroelectric.* Nano Letters, 2015. **15**(6): p. 3808-3814.

24.   Maisonneuve, V., et al., *Room-Temperature Crystal-Structure of the Layered Phase Cu(I)in(Iii)P2s6.* Journal of Alloys and Compounds, 1995. **218**(2): p. 157-164.

25.   Simon, A., et al., *PARAELECTRIC FERROELECTRIC TRANSITION IN THE LAMELLAR THIOPHOSPHATE CUINP2S6.* Chemistry of Materials, 1994. **6**(9): p. 1575-1580.

26.   Vysochanskii, Y.M., et al., *Raman spectroscopy study of the ferrielectric-paraelectric transition in layered CuInP2S6.* Physical Review B, 1998. **58**(14): p. 9119-9124.

27.   Maisonneuve, V., et al., *Ionic conductivity in ferroic CuInP2S6 and CuCrP2S6.* Ferroelectrics, 1997. **196**(1-4): p. 577-580.

28.   Balke, N., et al., *Locally Controlled Cu-Ion Transport in Layered Ferroelectric CuInP2S6.* Acs Applied Materials & Interfaces, 2018. **10**(32): p. 27188-27194.

29.   Studenyak, I.P., et al., *Disordering effect on optical absorption processes in CuInP2S6 layered ferrielectrics.* Physica Status Solidi B-Basic Research, 2003. **236**(3): p. 678-686.

30. Wang, X.W., et al., *Van der Waals engineering of ferroelectric heterostructures for long-retention memory.* Nature Communications, 2021. **12**(1).

31. Zhao, Z.J., et al., *Strong Temperature Effect on the Ferroelectric Properties of CuInP2S6 and Its Heterostructures.* Acs Applied Materials & Interfaces, 2020. **12**(46): p. 51820-51826.

32. Wang, X.W., et al., *Van der Waals negative capacitance transistors.* Nature Communications, 2019. **10**.

33. Neumayer, S.M., et al., *The Concept of Negative Capacitance in Ionically Conductive Van der Waals Ferroelectrics.* Advanced Energy Materials, 2020. **10**(39): p. 7.

34. Ma, R.R., et al., *High-speed ultraviolet photodetectors based on 2D layered CuInP2S6 nanoflakes.* Applied Physics Letters, 2020. **117**(13): p. 6.

35. Wu, J.B., et al., *High tunnelling electroresistance in a ferroelectric van der Waals heterojunction via giant barrier height modulation.* Nature Electronics, 2020. **3**(8): p. 466-472.

36. Li, B.C., et al., *An Electronic Synapse Based on 2D Ferroelectric CuInP2S6.* Advanced Electronic Materials, 2020. **6**(12): p. 7.

37. Si, M.W., et al., *Room-Temperature Electrocaloric Effect in Layered Ferroelectric CuInP2S6 for Solid-State Refrigeration.* Acs Nano, 2019. **13**(8): p. 8760-8765.

38. Niu, L., et al., *Controlled synthesis and room-temperature pyroelectricity of CuInP2S6 ultrathin flakes.* Nano Energy, 2019. **58**: p. 596-603.

39. Novoselov, K.S., et al., *2D materials and van der Waals heterostructures.* Science, 2016. **353**(6298).

40. Wu, S.D., L.W. Cheng, and Q. Wang, *Excitonic effects and related properties in semiconductor nanostructures: roles of size and dimensionality.* Materials Research Express, 2017. **4**(8).

41. Novoselov, K.S., et al., *Electric field effect in atomically thin carbon films.* Science, 2004. **306**(5696): p. 666-9.

42. Ponor. *Graphene - sigma and pi bonds*. 2020; Available from: https://commons.wikimedia.org/w/index.php?curid=92461297.

43. Castro Neto, A.H., et al., *The electronic properties of graphene.* Reviews of Modern Physics, 2009. **81**(1): p. 109-162.

44. Geim, A.K. and K.S. Novoselov, *The rise of graphene.* Nature Materials, 2007. **6**(3): p. 183-191.

45. Zhu, Y.W., et al., *Graphene and Graphene Oxide: Synthesis, Properties, and Applications.* Advanced Materials, 2010. **22**(35): p. 3906-3924.

46. Chen, J.H., et al., *Intrinsic and extrinsic performance limits of graphene devices on SiO2.* Nature Nanotechnology, 2008. **3**(4): p. 206-209.

47. Morozov, S.V., et al., *Giant intrinsic carrier mobilities in graphene and its bilayer.* Physical Review Letters, 2008. **100**(1).

48. Yazdi, G.R., et al., *Growth of large area monolayer graphene on 3C-SiC and a comparison with other SiC polytypes.* Carbon, 2013. **57**: p. 477-484.

49. Pallecchi, E., et al., *High Electron Mobility in Epitaxial Graphene on 4H-SiC(0001) via post-growth annealing under hydrogen.* Scientific Reports, 2014. **4**.

50. Song, H.S., et al., *Origin of the relatively low transport mobility of graphene grown through chemical vapor deposition.* Scientific Reports, 2012. **2**.

51. Li, X.S., et al., *Graphene Films with Large Domain Size by a Two-Step Chemical Vapor Deposition Process.* Nano Letters, 2010. **10**(11): p. 4328-4334.

52. Albar, J.D., et al., *An atomic carbon source for high temperature molecular beam epitaxy of graphene.* Scientific Reports, 2017. **7**.

53. Li, Z.L., et al., *Mechanisms of Liquid-Phase Exfoliation for the Production of Graphene.* Acs Nano, 2020. **14**(9): p. 10976-10985.

54. Zhang, K.L., et al., *Two dimensional hexagonal boron nitride (2D-hBN): synthesis, properties and applications.* Journal of Materials Chemistry C, 2017. **5**(46): p. 11992-12022.

55. Dean, C.R., et al., *Boron nitride substrates for high-quality graphene electronics.* Nature Nanotechnology, 2010. **5**(10): p. 722-726.

56. Bandurin, D.A., et al., *High electron mobility, quantum Hall effect and anomalous optical response in atomically thin InSe.* Nature Nanotechnology, 2017. **12**(3): p. 223-+.

57. Lee, G.H., et al., *Highly Stable, Dual-Gated MoS2 Transistors Encapsulated by Hexagonal Boron Nitride with Gate-Controllable Contact, Resistance, and Threshold Voltage.* Acs Nano, 2015. **9**(7): p. 7019-7026.

58. Tang, B., et al., *UV-SWIR broad range photodetectors made from few-layer alpha-In2Se3 nanosheets.* Nanoscale, 2019. **11**(27): p. 12817-12828.

59. Paszkowicz, W., et al., *Lattice parameters and anisotropic thermal expansion of hexagonal boron nitride in the 10-297.5 K temperature range.* Applied Physics a-Materials Science & Processing, 2002. **75**(3): p. 431-435.

60. Elias, C., et al., *Direct band-gap crossover in epitaxial monolayer boron nitride.* Nature Communications, 2019. **10**.

61. Watanabe, K., T. Taniguchi, and H. Kanda, *Direct-bandgap properties and evidence for ultraviolet lasing of hexagonal boron nitride single crystal.* Nature Materials, 2004. **3**(6): p. 404-409.

62. Schuster, R., et al., *Direct observation of the lowest indirect exciton state in the bulk of hexagonal boron nitride.* Physical Review B, 2018. **97**(4).

63. Kittel, C., *Introduction to solid state physics.* 1956: John Wiley and Sons.

64. Valasek, J., *Piezo-electric and allied phenomena in Rochelle salt.* Physical Review, 1921. **17**(4): p. 475-481.

65. Stengel, M. and N.A. Spaldin, *Origin of the dielectric dead layer in nanoscale capacitors.* Nature, 2006. **443**(7112): p. 679-682.

66. Stengel, M., D. Vanderbilt, and N.A. Spaldin, *Enhancement of ferroelectricity at metal-oxide interfaces.* Nature Materials, 2009. **8**(5): p. 392-397.

67. Liu, M.H., et al., *2D ferroelectric devices: working principles and research progress.* Physical Chemistry Chemical Physics, 2021. **23**(38): p. 21376-21384.

68. Park, C.B., et al., *Observation of Spin-Induced Ferroelectricity in a Layered van der Waals Antiferromagnet CuCrP2S6.* Advanced Electronic Materials, 2022. **8**(6).

69. Barraza-Lopez, S., et al., *Colloquium: Physical properties of group-IV monochalcogenide monolayers.* Reviews of Modern Physics, 2021. **93**(1).

70. Varotto, S., et al., *Room-temperature ferroelectric switching of spin-to-charge conversion in germanium telluride.* Nature Electronics, 2021. **4**(10): p. 740-747.

71. Ding, W.J., et al., *Prediction of intrinsic two-dimensional ferroelectrics in In2Se3 and other III2-VI3 van der Waals materials.* Nature Communications, 2017. **8**.

72. Yang, Q., M.H. Wu, and J. Li, *Origin of Two-Dimensional Vertical Ferroelectricity in WTe2 Bilayer and Multilayer.* Journal of Physical Chemistry Letters, 2018. **9**(24): p. 7160-7164.

73. Wang, C.S., et al., *Towards two-dimensional van der Waals ferroelectrics.* Nature Materials, 2023.

74. Liu, F.C., et al., *Room-temperature ferroelectricity in CuInP2S6 ultrathin flakes.* Nature Communications, 2016. **7**.

75. Maisonneuve, V., et al., *Ferrielectric ordering in lamellar CuInP2S6.* Physical Review B, 1997. **56**(17): p. 10860-10868.

76. Zhou, S., et al., *Anomalous polarization switching and permanent retention in a ferroelectric ionic conductor.* Materials Horizons, 2020. **7**(1): p. 263-274.

77. You, L., et al., *Origin of giant negative piezoelectricity in a layered van der Waals ferroelectric.* Science Advances, 2019. **5**(4).

78.   Bercha, D.M., et al., *Vibronic interaction in crystals with the Jahn-Teller centers in the elementary energy bands concept.* Condensed Matter Physics, 2015. **18**(3).

79.   Babuka, T., et al., *Layered ferrielectric crystals CuInP2S(Se)(6): a study from the first principles.* Phase Transitions, 2019. **92**(5): p. 440-450.

80.   Vanlanduyt, J., G. Vantendeloo, and S. Amelinckx, *Phase-Transitions in In2se3 as Studied by Electron-Microscopy and Electron-Diffraction.* Physica Status Solidi a-Applied Research, 1975. **30**(1): p. 299-314.

81.   Zhang, D.W., et al., *Ferroelectric order in van der Waals layered materials.* Nature Reviews Materials, 2022.

82.   Quereda, J., et al., *Strong Quantum Confinement Effect in the Optical Properties of Ultrathin alpha-In2Se3.* Advanced Optical Materials, 2016. **4**(12): p. 1939-1943.

83.   Li, W., et al., *Large disparity between optical and fundamental band gaps in layered In2Se3.* Physical Review B, 2018. **98**(16).

84.   Xue, F., et al., *Gate-Tunable and Multidirection-Switchable Memristive Phenomena in a Van Der Waals Ferroelectric.* Advanced Materials, 2019. **31**(29).

85.   Liu, Z., et al., *In-plane ferroelectric tunnel junctions based on 2D α-In2Se3/semiconductor heterostructures.* npj Computational Materials, 2023. **9**(1): p. 6.

86.   Castellanos-Gomez, A., et al., *Deterministic transfer of two-dimensional materials by all-dry viscoelastic stamping.* 2d Materials, 2014. **1**(1).

87.   Meitl, M.A., et al., *Transfer printing by kinetic control of adhesion to an elastomeric stamp.* Nature Materials, 2006. **5**(1): p. 33-38.

88.   Bie, Y.Q., et al., *Site-Specific Transfer-Printing of Individual Graphene Microscale Patterns to Arbitrary Surfaces.* Advanced Materials, 2011. **23**(34): p. 3938-+.

89.   Bogardus, E.H. and H.B. Bebb, *Bound-Exciton Free-Exciton Band-Acceptor Donor-Acceptor and Auger Recombination in Gaas.* Physical Review, 1968. **176**(3): p. 993-&.

90.   Patane, A. and N. Balkan, *Semiconductor Research: Experimental Techniques.* Springer Series in Materials Science. 2012: Springer.

91.   Jorio, A.S., R.;Dresselhaus, G.;Dresselhaus, M., *Raman Spectroscopy in Graphene Related Systems.* 2011: John Wiley & Sons.

92.   Huang, M.Y., et al., *Probing Strain-Induced Electronic Structure Change in Graphene by Raman Spectroscopy.* Nano Letters, 2010. **10**(10): p. 4074-4079.

93.   Binnig, G., C.F. Quate, and C. Gerber, *Atomic Force Microscope.* Physical Review Letters, 1986. **56**(9): p. 930-933.

94.   Gruverman, A., O. Auciello, and H. Tokumoto, *Scanning force microscopy for the study of domain structure in ferroelectric thin films.* Journal of Vacuum Science & Technology B, 1996. **14**(2): p. 602-605.

95.   Nonnenmacher, M., M.P. Oboyle, and H.K. Wickramasinghe, *Kelvin Probe Force Microscopy.* Applied Physics Letters, 1991. **58**(25): p. 2921-2923.

96.   Ma, Q.J., et al., *Tunable Optical Properties of 2D Materials and Their Applications.* Advanced Optical Materials, 2021. **9**(2).

97.   Yan, X.Q., et al., *Temperature-tunable optical properties and carrier relaxation of CuInP2S6 crystals under ferroelectric-paraelectric phase transition.* Journal of Materials Chemistry C, 2022. **10**(2): p. 696-706.

98.   Rao, R., et al., *Ferrielectric-paraelectric phase transitions in layered CuInP2S6 and CuInP2S6- In4/3P2S6 heterostructures: A Raman spectroscopy and x-ray diffraction study.* Physical Review Materials, 2022. **6**(4).

99.   Liu, Z., et al., *Temperature-dependent photoluminescence and lasing properties of CsPbBr3 nanowires.* Applied Physics Letters, 2019. **114**(10).

100.   Trapalis, A., et al., *Temperature dependence of the band gap of zinc nitride observed in photoluminescence measurements.* Applied Physics Letters, 2017. **111**(12).

101.   Zhang, T.J. and J. Wang, *Defect-Enhanced Exciton-Exciton Annihilation in Monolayer Transition Metal Dichalcogenides at High Exciton Densities.* Acs Photonics, 2021. **8**(9): p. 2770-2780.

102.   Gu, P.F., et al., *Photoluminescent Quantum Interference in a van der Waals Magnet Preserved by Symmetry Breaking.* Acs Nano, 2020. **14**(1): p. 1003-1010.

103.   Yuan, L., et al., *Twist-angle-dependent interlayer exciton diffusion in WS2-WSe2 heterobilayers.* Nature Materials, 2020. **19**(6): p. 617-+.

104.   Urbach, F., *The Long-Wavelength Edge of Photographic Sensitivity and of the Electronic Absorption of Solids.* Physical Review, 1953. **92**(5): p. 1324-1324.

105. Huang, W.H., et al., *Gate-Coupling-Enabled Robust Hysteresis for Nonvolatile Memory and Programmable Rectifier in Van der Waals Ferroelectric Heterojunctions.* Advanced Materials, 2020. **32**(14): p. 9.

106. Wang, F., et al., *Subthermionic field-effect transistors with sub-5 nm gate lengths based on van der Waals ferroelectric heterostructures.* Science Bulletin, 2020. **65**(17): p. 1444-1450.

107. Wang, X.W., et al., *Van der Waals engineering of ferroelectric heterostructures for long-retention memory.* Nature Communications, 2021. **12**(1): p. 8.

108. Wang, X.W., et al., *Van der Waals negative capacitance transistors.* Nature Communications, 2019. **10**: p. 8.

109. Wang, X.R., et al., *Interfacial ferroelectricity in rhombohedral-stacked bilayer transition metal dichalcogenides.* Nature Nanotechnology, 2022. **17**(4): p. 367-+.

110. Zhou, S., et al., *Van der Waals layered ferroelectric CuInP2S6: Physical properties and device applications.* Frontiers of Physics, 2021. **16**(1).

111. Chen, J.H., et al., *Charged-impurity scattering in graphene.* Nature Physics, 2008. **4**(5): p. 377-381.

112. Novikov, D.S., *Elastic scattering theory and transport in graphene.* Physical Review B, 2007. **76**(24): p. 245435.

113. Baeumer, C., et al., *Tunable Carrier Type and Density in Graphene/PbZr0.2Ti0.8O3 Hybrid Structures through Ferroelectric Switching.* Nano Letters, 2013. **13**(4): p. 1693-1698.

114. Jie, W., et al., *Ferroelectric Polarization Effects on the Transport Properties of Graphene/PMN-PT Field Effect Transistors.* The Journal of Physical Chemistry C, 2013. **117**(26): p. 13747-13752.

115. Lee, S. and Y. Lee, *Graphene/lead-zirconate-titanate ferroelectric memory devices with tenacious retention characteristics.* Carbon, 2018. **126**: p. 176-182.

116. Lipatov, A., et al., *Polarization-Dependent Electronic Transport in Graphene/Pb(Zr,Ti)O3 Ferroelectric Field-Effect Transistors.* Advanced Electronic Materials, 2017. **3**(7): p. 1700020.

117. Rajapitamahuni, A., et al., *Examining Graphene Field Effect Sensors for Ferroelectric Thin Film Studies.* Nano Letters, 2013. **13**(9): p. 4374-4379.

118. Yue, H., et al., *Graphene probe to explore the surface polarization in SrTiO3 without damage.* Applied Physics Letters, 2021. **119**(7).

119. Yusuf, M.H., et al., *Extrinsic and Intrinsic Charge Trapping at the Graphene/Ferroelectric Interface.* Nano Letters, 2014. **14**(9): p. 5437-5444.

120. Wang, H.M., et al., *Hysteresis of Electronic Transport in Graphene Transistors.* Acs Nano, 2010. **4**(12): p. 7221-7228.

121. Cottam, N.D., et al., *Defect-Assisted High Photoconductive UV–Visible Gain in Perovskite-Decorated Graphene Transistors.* ACS Applied Electronic Materials, 2020. **2**(1): p. 147-154.

122. Tsymbal, E.Y. and H. Kohlstedt, *Applied physics - Tunneling across a ferroelectric.* Science, 2006. **313**(5784): p. 181-183.

123. Sire, C., et al., *Statistics of electrical breakdown field in HfO2 and SiO2 films from millimeter to nanometer length scales.* Applied Physics Letters, 2007. **91**(24).

124. Hattori, Y., et al., *Layer-by-Layer Dielectric Breakdown of Hexagonal Boron Nitride.* Acs Nano, 2015. **9**(1): p. 916-921.

125. Goerbig, M.O., *Electronic properties of graphene in a strong magnetic field.* Reviews of Modern Physics, 2011. **83**(4): p. 1193-1243.

126. Slizovskiy, S. and J.J. Betouras, *Nonlinear magnetization of graphene.* Physical Review B, 2012. **86**(12).

127. Zhang, Y.B., et al., *Experimental observation of the quantum Hall effect and Berry's phase in graphene.* Nature, 2005. **438**(7065): p. 201-204.

128. Novoselov, K.S., et al., *Room-Temperature Quantum Hall Effect in Graphene.* Science, 2007. **315**(5817): p. 1379-1379.

129. Kane, C.L. and E.J. Mele, *Quantum spin Hall effect in graphene.* Physical Review Letters, 2005. **95**(22).

130. Gusynin, V.P. and S.G. Sharapov, *Unconventional integer quantum Hall effect in graphene.* Physical Review Letters, 2005. **95**(14).

131. Guinea, F., M.I. Katsnelson, and A.K. Geim, *Energy gaps and a zero-field quantum Hall effect in graphene by strain engineering.* Nature Physics, 2010. **6**(1): p. 30-33.

132. Novoselov, K.S., et al., *Unconventional quantum Hall effect and Berry's phase of 2 pi in bilayer graphene.* Nature Physics, 2006. **2**(3): p. 177-180.

133. Vonklitzing, K., G. Dorda, and M. Pepper, *New Method for High-Accuracy Determination of the Fine-Structure Constant Based on*

Quantized Hall Resistance. Physical Review Letters, 1980. **45**(6): p. 494-497.

134. Fogler, M.M., D.S. Novikov, and B.I. Shklovskii, *Screening of a hypercritical charge in graphene.* Physical Review B, 2007. **76**(23).

135. Terekhov, I.S., et al., *Screening of Coulomb impurities in graphene.* Physical Review Letters, 2008. **100**(7).

136. Luican-Mayer, A., et al., *Screening Charged Impurities and Lifting the Orbital Degeneracy in Graphene by Populating Landau Levels.* Physical Review Letters, 2014. **112**(3).

137. Pyatkovskiy, P.K. and V.P. Gusynin, *Dynamical polarization of graphene in a magnetic field.* Physical Review B, 2011. **83**(7).

138. Alexander-Webber, J.A., et al., *Phase Space for the Breakdown of the Quantum Hall Effect in Epitaxial Graphene.* Physical Review Letters, 2013. **111**(9).

139. Janssen, T.J.B.M., et al., *Anomalously strong pinning of the filling factor nu=2 in epitaxial graphene.* Physical Review B, 2011. **83**(23).

140. Kopylov, S., et al., *Charge transfer between epitaxial graphene and silicon carbide.* Applied Physics Letters, 2010. **97**(11).

141. Tzalenchuk, A., et al., *Towards a quantum resistance standard based on epitaxial graphene.* Nature Nanotechnology, 2010. **5**(3): p. 186-189.

142. Alexander-Webber, J.A., et al., *Giant quantum Hall plateaus generated by charge transfer in epitaxial graphene.* Scientific Reports, 2016. **6**.

143. Kudrynskyi, Z.R., et al., *Giant Quantum Hall Plateau in Graphene Coupled to an InSe van der Waals Crystal.* Physical Review Letters, 2017. **119**(15).

144. Bhuiyan, M.A., et al., *Photoquantum Hall Effect and Light-Induced Charge Transfer at the Interface of Graphene/InSe Heterostructures.* Advanced Functional Materials, 2019. **29**(3): p. 1805491.

145. Slizovskiy, S., *Bound states of charges on top of graphene in a magnetic field.* Physical Review B, 2015. **92**(19).

146. Vaquero, D., et al., *Phonon-mediated room-temperature quantum Hall transport in graphene.* Nature Communications, 2023. **14**(1): p. 318.

147. Dey, A., et al., *Memristive effects due to charge transfer in graphene gated through ferroelectric CuInP2S6.* 2d Materials, 2022. **9**(3).

148. Kalon, G., et al., *The role of charge traps in inducing hysteresis: Capacitance-voltage measurements on top gated bilayer graphene.* Applied Physics Letters, 2011. **99**(8).

149. Liao, Z.M., et al., *Hysteresis reversion in graphene field-effect transistors.* Journal of Chemical Physics, 2010. **133**(4).

150. Choi, M.S., et al., *Controlled charge trapping by molybdenum disulphide and graphene in ultrathin heterostructured memory devices.* Nature Communications, 2013. **4**.

151. Hwang, H.J., et al., *Direct Measurement of Transient Charging and Dipole Alignment Speed in Ferroelectric Hf0.5Zr0.5O2 Gate Dielectric Using Graphene FETs.* Advanced Electronic Materials, 2021. **7**(5).

152. Zheng, Y., et al., *Graphene Field-Effect Transistors with Ferroelectric Gating.* Physical Review Letters, 2010. **105**(16).

153. Lipatov, A., et al., *Polarization-Dependent Electronic Transport in Graphene/Pb(Zr,Ti)O-3 Ferroelectric Field-Effect Transistors.* Advanced Electronic Materials, 2017. **3**(7).

154. Hartland, A., *The Quantum Hall-Effect and Resistance Standards.* Metrologia, 1992. **29**(2): p. 175-190.

155. Poumirol, J.M., et al., *Impact of disorder on the v=2 quantum Hall plateau in graphene.* Physical Review B, 2010. **82**(12).

156. Chae, D.H., et al., *Investigation of the stability of graphene devices for quantum resistance metrology at direct and alternating current.* Measurement Science and Technology, 2022. **33**(6).

157. Giesbers, A.J.M., et al., *Quantum-hall activation gaps in graphene.* Physical Review Letters, 2007. **99**(20).

158. Yang, W., et al., *Epitaxial growth of single-domain graphene on hexagonal boron nitride.* Nature Materials, 2013. **12**(9): p. 792-797.

159. Ponomarenko, L.A., et al., *Cloning of Dirac fermions in graphene superlattices.* Nature, 2013. **497**(7451): p. 594-597.

160. Woods, C.R., et al., *Commensurate-incommensurate transition in graphene on hexagonal boron nitride.* Nature Physics, 2014. **10**(6): p. 451-456.

161. Finney, N.R., et al., *Tunable crystal symmetry in graphene-boron nitride heterostructures with coexisting moire superlattices.* Nature Nanotechnology, 2019. **14**(11): p. 1029-+.

162. Hunt, B., et al., *Massive Dirac Fermions and Hofstadter Butterfly in a van der Waals Heterostructure.* Science, 2013. **340**(6139): p. 1427-1430.

163. Yankowitz, M., et al., *Emergence of superlattice Dirac points in graphene on hexagonal boron nitride.* Nature Physics, 2012. **8**(5): p. 382-386.

164. Wang, Y., et al., *Quantum Hall phase in graphene engineered by interfacial charge coupling.* Nature Nanotechnology, 2022.

165. Neumayer, S.M., et al., *Ionic Control over Ferroelectricity in 2D Layered van der Waals Capacitors.* Acs Applied Materials & Interfaces, 2022. **14**(2): p. 3018-3026.

166. Wang, L., et al., *One-Dimensional Electrical Contact to a Two-Dimensional Material.* Science, 2013. **342**(6158): p. 614-617.

167. He, H., et al., *Accurate graphene quantum Hall arrays for the new International System of Units.* Nature Communications, 2022. **13**(1): p. 6933.